ECAP-2022-002

Setup characterisation measurements for grating-based X-ray phase-contrast imaging

Master's Thesis in Physics

Presented by:

Constantin Rauch

April 2022

Erlangen Centre for Astroparticle Physics

Friedrich-Alexander-Universität Erlangen-Nürnberg

Supervisor: Prof. Dr. Stefan Funk

Contents

1. Introduction

In high energy density (HED) experiments, matter under extreme conditions is studied to gain new insights in the fields of confined fusion, material science and laboratory astrophysics ([Ant+17], [Col+98] and [Ben+96]). One way of creating the extreme conditions required for HED experiments is focussing a high-powered laser onto a target. The Petawatt High-Energy Laser for Heavy Ion EXperiments (PHELIX) at the GSI Helmholtzzentrum für Schwerionenforschung in Darmstadt is such a high-power laser. It reaches laser intensities of up to $2 \cdot 10^{21}\,\mathrm{W/cm^2}$ and pumps up to 200 J into the target with each shot on timescales shorter than 20 ps [Göt22].

The PHELIX laser can simultaneously create two laser pulses with about 30 J pulse energy, allowing for the imaging of HED processes. The first laser pulse launches the HED process, for example a plasma shockwave. The second laser pulse is focussed on a micrometer thin tungsten wire, destroying it completely and creating an ultra-short X-ray flash [Aks19]. These X-rays propagate through the plasma shock created by the first pulse and interact with it. Measuring only the absorption image of X-rays in the target typically yields low contrasts, due to low density gradients. Measuring the phase shift imprinted by the shockwave on the phase front of the X-rays promises better contrast [Bar+19]. Additionally, the phase shift is linearly related to the electron density, making it a convenient measure for quantitative studies of the shockwave [Bar+19].

One way of measuring this phase shift is grating-based X-ray phase-contrast imaging, which requires an interferometer consisting of at least two gratings in addition to the X-ray detector. High-quality gratings and a well suited detector are crucial for the quality of the resulting images. Characterising the gratings and detectors is therefore vital for an optimised setup.

Angular X-ray transmission (AXT) measurements allow for the evaluation of absorption gratings at laboratory X-ray tubes. Data acquisition, processing and analysis required for AXT measurements are presented in this thesis.

Furthermore, methods for characterising detector noise and spatial resolution performance are introduced to examine the performance of various detectors for laboratory use and utilization at the PHELIX facility.

Finally, the method for spatial resolution characterisation is adapted to examine the influence of the Moiré pattern and detector resolution on the spatial resolution of the entire imaging setup. A phantom is designed specifically for this adapted method.

The methods and results presented in this thesis will help enable the first imaging of a plasma shock, unlocking a significant milestone for laboratory astrophysics.

2. Theoretical background

The following chapter aims to introduce the physical concepts required in this Master's Thesis. First, X-rays and their production processes are introduced, then methods for their detection are presented. Finally, the fundamentals of Moiré-Imaging, the resulting image modalities and experimental setups are explained.

2.1. X-rays

X-rays are electromagnetic radiation consisting of photons with an energy in the range of about 100 eV to 100 keV [Dem18]. The X-ray spectrum is bordered by ultraviolet radiation on the lower energy end of the spectrum and by gamma radiation on the other side.

X-rays for medical and industrial imaging applications are usually produced with X-ray tubes. In these tubes, electrons are emitted from a cathode and accelerated in a vacuum using high voltage. Upon reaching the anode, the electrons interact with the anode material and photons are emitted via Bremsstrahlung and characteristic emission. An example spectrum is sketched in Figure 2.1.

- Bremsstrahlung continuum (part marked with orange line in Figure 2.1): Charged particles that are accelerated or decelerated emit Bremsstrahlung. This part of the spectrum is a continuous distribution with energies up to the acceleration voltage.
- Characteristic lines (part marked with blue line in Figure 2.1): Interactions of the high energy electrons can remove bound electrons from inner shells of the atoms in the anode. The vacancies are filled by outer shell electrons, and the discrete energy difference between the two participating states is emitted as a single photon. These lines are specific to the atom. Hence, the choice of anode material determines the resulting energy spectrum.

Although the working principle of different X-ray tubes is similar, special designs have been developed in order to fulfil special needs. Experiments in this thesis were conducted using a liquid metal jet tube, the excillum MetalJet C2 [AB21]. Here, the anode is realised as a liquid metal alloy jet consisting of gallium and indium that is constantly regenerated. This design allows for a high power density of the electron beam and therefore higher X-ray fluxes compared to the conventional microfocus tubes with solid anodes. Since the constant regeneration efficiently removes waste heat from the focal spot, damage to the anode is prevented. With this design, electron beam spot sizes on the anode in the micrometer range are possible. A more detailed description and the data sheet can be found at [AB21].

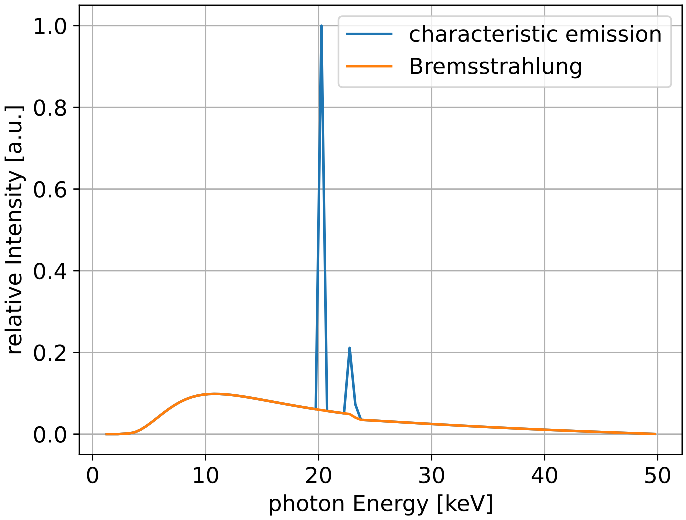

Figure 2.1.: Sketch of the relative intensity of X-ray emission over the photon energy in keV created by an X-ray tube using 50 kVp acceleration voltage and a rhodium anode. Plot created using [POB21].

A source for high energy physics experiments are X-ray backlighter sources. They produce X-rays using a high-powered ultrashort laser burst. The laser is focussed onto a target, for example a tungsten wire or foil, where it accelerates electrons to high energies. These electrons subsequently emit Bremsstrahlung and interact with the material, allowing for emission of characteristic X-rays. The target is destroyed in the process and the X-ray emission last only for a very short time interval.

2.2. Interaction of X-rays with matter

One property of X-rays is their capability to propagate through matter opaque to visible light. X-ray-photons propagating through material can interact with its atoms via the following three processes [Dem17]. Their cross-sections are shown in Figure 2.2 alongside the total atomic cross-section defined as the sum of the individual cross-sections.

Photons with energies higher than the binding energy of the atom can be absorbed entirely by an inner shell electron in a process called photoelectric absorption. During this process, the atom is ionized. The freed electron is called photoelectron and receives all the absorbed energy. The vacancy left by the electron can be filled by an outer shell electron under the emission of characteristic radiation as explained in section 2.1. The cross-section of the photoelectric effect is given by:

$$\sigma_{\text{photo}} \propto Z^5 / E_\gamma^{3.5} \tag{2.1}$$

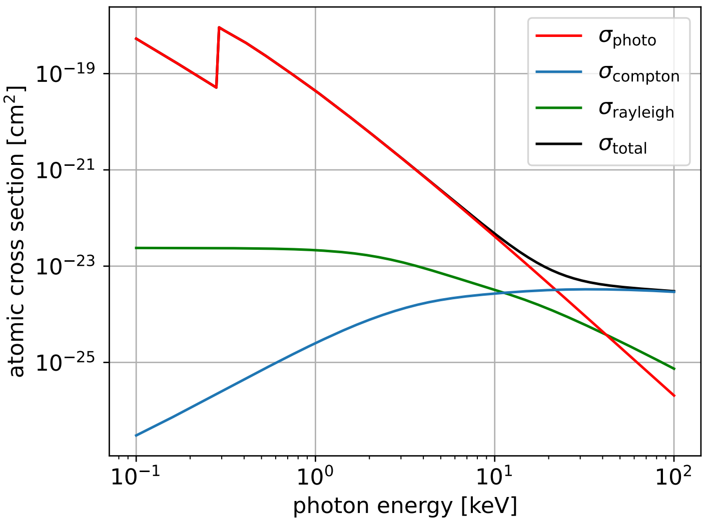

Figure 2.2.: Atomic cross-sections of photon interactions with carbon in cm^2 over the photon energy in keV. Shown are the contributions listed in section 2.2, namely photoelectric absorption, the Compton effect, and Rayleigh scattering. Data taken from [ERS02]. Also shown is the sum of the individual cross-sections as σ_{tot}.

where Z is the atomic number and E_γ the photon energy. Due to the discrete nature of ionisation energies, the cross-section of the photoelectric effect contains sharp absorption edges, where the photon energy surpasses the energy required to remove an electron from an inner shell. The photoelectric effect is especially dominant for materials with high atomic numbers and falls off quickly with increasing energy.

Photons with energies higher than the binding energies of the material can inelastically scatter with loosely bound or free electrons. This process is called Compton scattering. A part of the photon energy is transferred to the electron, resulting in an energy loss of the photon. The interaction cross-section of the Compton effect is proportional to the atomic number of the material over the photon energy:

$$\sigma_{\mathrm{c}} \propto Z/E_\gamma \tag{2.2}$$

After the interaction, the electron can move freely through the material. Compared to the photoelectric absorption, the Compton effect becomes dominant at higher energies.

For photon energies smaller than the binding energy of the atoms in the material, the main interaction is Rayleigh scattering. X-ray photons excite electronic shells of the atoms, which subsequently deexcite via the emission of photons of the same energy. The passing radiation is not permanently absorbed, therefore no attenuation takes place. Instead, the effective speed of light within the material is reduced by repeated absorption and emission.

The cross-sections of the three aforementioned processes are plotted for carbon in Figure 2.2. For energies up to 10 keV the dominant process is photoelectric absorption.

For higher energies, the Compton effect becomes the more dominant effect. An absorption edge within the cross-section of the photoelectric effect can be found at about 200 eV in Figure 2.2.
A single photon can undergo the processes listed above multiple times until it is either completely absorbed or leaves the material. Considering a beam of X-ray photons I passing through a thin layer of absorbing material with a number density of atoms n and thickness Δz, the following relation holds [CAS17]:

$$\frac{I}{I_0} = -n\sigma_{\text{tot}}\Delta z \tag{2.3}$$

where

$$\sigma_{\text{tot}} = \sigma_{\text{photo}} + \sigma_{\text{compton}} + \sigma_{\text{rayleigh}} \tag{2.4}$$

is the total interaction cross-section for an entire atom [HS96]. Equation 2.3 can be solved for materials with thickness z to obtain

$$I(z) = I_0 e^{-n\sigma_{\text{tot}} z} = I_0 e^{-\mu z}, \quad n\sigma_{\text{tot}} = \mu, \tag{2.5}$$

the Lambert-Bert law. In Equation 2.5 μ is called the absorption coefficient. The attenuation of the X-ray beam intensity follows an exponential decay and depends on the density of the absorber, its atomic composition, thickness and the photon energy. Any energy lost to the X-ray beam is converted within the material either to thermal energy or into kinetic energy of secondary particles, for example electrons. These secondary particles can be detected, allowing for an indirect measurement of X-ray photons. This will be discussed in the following section.

2.3. Detection of X-rays

In order to use X-rays for imaging purposes, spatially resolved detection of X-ray photons is required. Unlike visible light, X-rays have a long range in most detector materials like silicon. This makes their detection challenging. Different types of detectors have been developed, all rely on the interactions of X-ray photons with matter as described in section 2.2. Three of these types are used and characterised in this thesis: Analogue imaging plates, direct and indirect detection semiconductor devices. Of interest in this thesis are the properties of spatial resolution and the noise characteristic. Spatial resolution determines the smallest distance at which two point sources can be distinguished by the detector and therefore the minimum size of structures that can be resolved by the detector. The detectors noise characteristic determines the amount of photons required to produce a clearly visible signal within the image. Both parameters are discussed in greater detail in chapter 4.
The following sections describe the detectors, their working principles and their imaging properties.

2.3.1. Imaging plates

Imaging plates are phosphor screens that store the image information temporarily. Their main component is a layer consisting of photostimulable phosphor crystals suspended in an organic binder [Miy+86]. Upon illumination of the imaging plate with X-rays, electrons are freed from ions within the crystal and are trapped in lattice defects [Fik+12], saving the information as electrons in metastable states. By illuminating the imaging plate with visible light, these electrons can obtain the necessary energy to leave the defects and recombine with their origin ions, leaving those in an excited state. The subsequent deexcitation happens under emission of light, which can be detected. The emission of light under illumination of the crystal is called photostimulated luminescence (PSL) [Miy+86]. The amount of luminescence photons is proportional to the amount of X-ray energy the imaging plate was exposed to. The recombination also happens spontaneously causing the image to fade over time, even if not exposed to light.

The readout using the effect of PSL is performed by an imaging plate scanner, consisting of a laser and a photomultiplier tube [Miy+86]. A scan width, equivalent to a pixel size, can be selected by varying the step width with which the laser is moved across the imaging plate. Choosing a larger step size means more PSL photons are measured per pixel, at the cost of a decrease in spatial resolution and vice versa. This scanning process digitizes the previously analogue image information. After the image is read out, the imaging plate can be erased by exposing it to visible light for a few minutes.

The main advantage of imaging plates is their lack of electronic components during image acquisition, allowing for their usage at locations exposed to electromagnetic pulses without any problems. On the other hand, the manual readout adds complication to experimental procedures, especially in vacuum and severely limits the achievable acquisition rate.

2.3.2. Semiconductor detectors

Another type of X-ray detector are the semiconductor detectors. They come in a wide variety depending on the special requirements different experiments impose. Specialised designs have emerged to detect charged and neutral particles, light with different photon energies and even single photons. Of interest for this thesis are pixelated and charge integrating detectors for visible light or X-rays. This section provides a brief overview of semiconductors and the mechanisms and structures used in the detection of X-rays following [Lut+07] and [BP18].

A semiconductor is a solid state material with special conduction properties stemming from its electronic energy band structure. These energy bands represent the available free states for electrons within the lattice structure of the material. The most important energy bands are the valence and conduction band. States within the conduction band have higher energy than states within the valence band. In a semiconductor, both bands are separated by a band gap. Electrons can be excited from the valence into the conduction on the condition that they receive at least the band gap energy. Excitation can happen as a result of a variety of different physical interactions. For photons, the interactions are listed in section 2.2, other processes include interactions with charged particles. Electrons can also be thermally excited by interaction with the lattice of the material. The probability for an electron to be excited thermally increases exponentially with increasing temperature [Lut+07].

When an electron is excited from the conduction band to the valence band, a hole is left behind. The hole can be filled by neighbouring electrons within the valence band, effectively creating a freely moving positive charge. Hence, excitations of electrons produce two elementary charges worth of charge carriers. Electrons from the valence band and holes from the conduction band can recombine releasing the band gap energy. In most cases the energy is released as heat and in some cases via radiation of electromagnetic radiation.

By doping a semiconductor with atoms that have a different number of valence electrons, the properties of the semiconductor can be altered. This allows for the creation of structures like depletion zones. The number of free charge carriers within a depletion zone is significantly lower than in the undoped semiconductor, reducing its conductivity [Lut+07]. As mentioned above, incident photons can interact with the material. If this interaction takes place within the depletion zone, the free charge carrier that are created by the interaction can be separated by an external voltage. The flow of charge carriers through the depletion zone can be measured as a current. In this way, a light sensitive structure is obtained. The higher the photon incidence, the higher the number of free charge carriers within the depletion zone and the higher the current.

A detector that relies on the detection of X-rays within the depletion zone is called direct detection detector. An alternative approach, called indirect detection, is described in subsection 2.3.3.

For imaging purposes, pixelated charge integrating detectors are used. They integrate a signal in each pixel over a certain exposure time, after which each pixel is read out. Two major designs exist for this purpose, the charge-coupled device, CCD in short, and CMOS (complimentary metal-oxide-semiconductor) active pixel detectors. They are described in the following.

CCDs CCDs consist of a passive pixel array and a single read out register. The layout of the array is shown in Figure 2.3a. A depletion zone is covered by an insulating layer of silicon oxide upon which metal or polysilicon contacts are placed [Lut+07]. By applying different voltages to neighbouring contacts, local potential wells (Figure 2.3b) can be created within the depletion zone. Free charge carriers are trapped within these potential wells, storing them within the pixel they were created in. A two-dimensional pixel matrix can be achieved by placing many of these columns next to each other.

After illuminating the CCD detector, a readout must be performed in order to digitize the signal. By applying different periodic alternating voltages $\Phi_1 - \Phi_3$, the potential wells can be moved. This pushes their content pixel by pixel towards the readout registers, shown at the bottom in Figure 2.3a. Similarly, these readout registers are one by one pushed towards the output amplifier and analogue to digital converter, where the charge is amplified and converted into a digital value. The process is repeated until all pixels are read out and digitized.

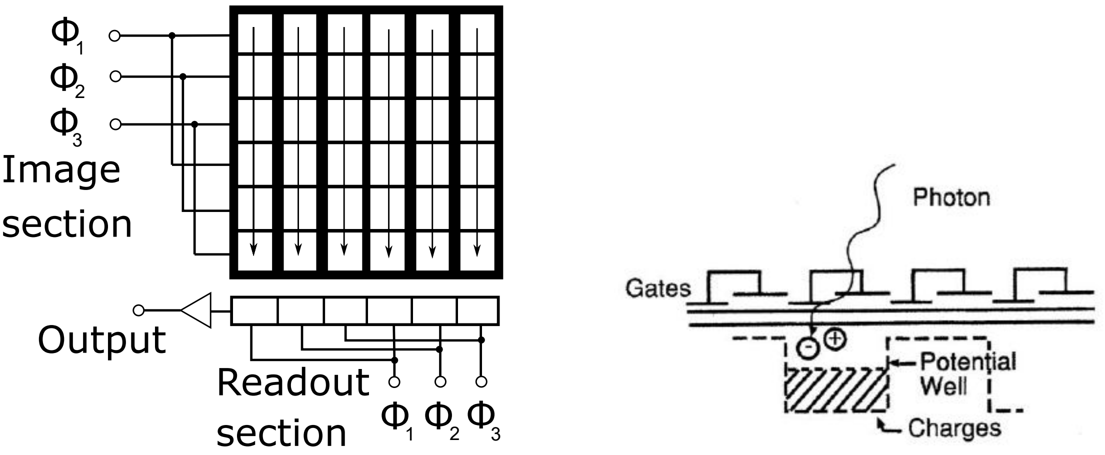

(a) Pixel matrix of a typical CCD. Shown are several columns and rows of pixels. The arrows depict the direction in which charges are shifted during readout. Image adapted from [GTE02].

(b) Electrodes along a CCD column and resulting potential wells created by the potential. Also shown are free charges created by incident photons captured within such a potential well. Image taken from [GTE02].

Figure 2.3.: CCD matrix and electrodes to create the potential wells. A detailed explanation can be found in the text.

The main advantage of this design is the fact that almost the entire pixel matrix can be sensitive to photons, increasing the detection efficiency. A major disadvantage of CCD cameras is their requirement for shutters, otherwise illumination during readout will lead to additional charges accumulated within pixels while they are moved towards the readout registers. This causes smearing of structures within the image. The shutter can either be implemented physically or electronically by providing additional shift registers for each pixel, which are not light sensitive and into which the pixel charge can be transferred after the desired integration time is over [GTE02]. This design is called interline CCD and reduces the light sensitive area of the detector. Another disadvantage of CCDs is the imperfect insulation of pixels against each other: Overexposure of single pixels can lead to an overflow of charges into neighbouring pixels, since the division between pixels is only created by potential wells of finite depth.

CMOS image Sensor Compared to CCD sensors, CMOS detectors use active pixels where parts of the readout electronics are integrated in each individual pixel. An example for a pixel circuit diagram is shown in Figure 2.4. In this example, each pixel consists of a photo diode followed by an amplifier (M_{sf}). Before image acquisition starts, the photo diode is reset by applying a defined reverse bias voltage via the reset transistor M_{rst}. During acquisition, the voltage over the diode drops proportional to the amount of incident light, as current stemming from the light slowly discharges the photo diode. At the end of acquisition, the voltage over the photo diode is amplified via the amplifier

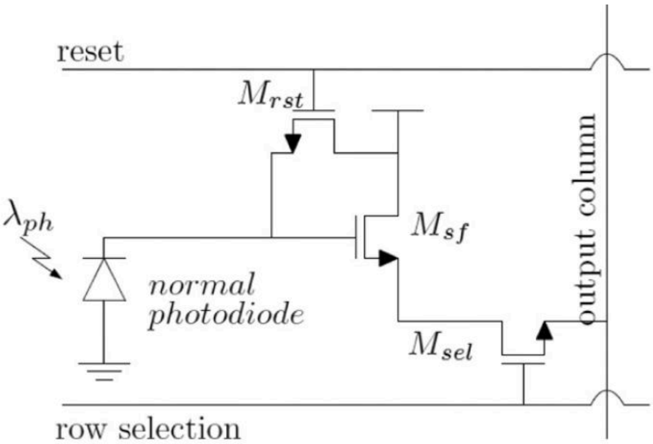

Figure 2.4.: Circuit schematic for a simple CMOS image sensor pixel [GC16]. Each pixel consists of a photodiode, which is the photosensitive part, a reset transistor to reset the photodiode and a source follower for signal amplification. Each pixel can be individually addressed via the appropriate selection line in combination with the selection transistor.

transistor and read out by setting the row selection of the pixel to high and reading the appropriate column output line.

The additional transistors allow for a direct readout of voltage. This can increase the readout speed, enable only partial readout of the image sensor and allow for fast binning of neighbouring pixels [Mag03]. Additionally, pixels are electronically insulated against each other, reducing flow of charges between pixels. The pixels can be read out individually without influencing other pixels of the sensor, making a physical shutter obsolete. The downside of this direct readout is the increased number of structures per pixel, reducing the light sensitive area.

2.3.3. Scintillators

Scintillating detectors use the luminescence of materials to convert X-ray photons into lower energy photons [KW16], which can be detected with higher efficiency by a CCD or CMOS camera. The detectors used in this thesis are fabricated using inorganic crystal scintillators, which can be made from materials with large atomic numbers. This increases the interaction probability, especially for photoelectric absorption (see section 2.2).

Inorganic crystal scintillators contain so-called luminescence centres. They either exist within a crystal naturally or can be added by doping a crystal. Lower energy photons are created in these luminance centres when free electrons and holes, created by incident X-rays or secondary electrons, recombine. These scintillating photons are emitted in random directions and have an energy lower than the band gap energy, allowing them to propagate through the crystal unimpeded. The thicker the scintillator, the more of the energy of the original X-ray photon can be converted into lower energy photons. However, the random direction of emission smears the signal within the scintillator. Therefore, the spread of photons at the exit surface increases with increasing scintillator width. This makes the choice of scintillator thickness a trade-off between detection efficiency and spatial resolution. Some scintillating crystals can be produced with microstructures to limit the signal spread, for example as very thin and long needles, trying to achieve the best of both worlds.

The luminescence photons leaving the scintillator at the exit surface have to be mapped to the surface of the CCD or CMOS sensor. Setups with different types of coupling between the scintillator and the semiconductor detector are possible (see [GTE02]).

Some scintillators can be built directly on the surface of the camera sensor. The **direct deposition** method requires no additional optical elements to focus the image from the scintillating layer onto the sensor. The lack of such a component also means, that no magnification can occur. As a consequence, the pixel size as well as the field of view of the entire detector is limited by the sensor.

A scintillating screen can also be coupled to a sensor using a **fibre optic** taper. Here, many fibres are bonded on one end to the screen and on the other side to the surface of the sensor. The main advantage of this setup is, that the screen and the sensor need not have the same size, the taper performs the mapping of the image in the scintillator onto the sensor. Disadvantages include distortions in the image due to imperfect mapping and the fact, that the fibre taper is visible in the raw images produced by the detector.

Another way of coupling the scintillator to the sensor is **lens coupling**. The image from the scintillating screen is focused onto the sensor chip using optical lenses. Compared to the fibre optic coupling, lens coupling has no issues with image artefacts from a taper, but for certain geometric constellations the coupling efficiency is significantly lower [GTE02]. This decreases the number of photons reaching the sensor.

2.4. Grating-based X-ray phase-contrast imaging

Transmission based X-ray imaging relies on the varying absorption of X-rays in a material to produce an image. It is widely used in medical and industrial applications. With grating-based X-ray phase-contrast imaging (gbpci), two additional imaging modalities containing additional information can be obtained. An interferometer is used to retrieve the phase shift induced by objects in the propagation path of the wave. The following sections explain how the phase shift is generated, introduce the Moiré and Talbot effect and explain the steps for image modality retrieval.

2.4.1. Electromagnetic waves in matter

Phase-contrast imaging exploits wave properties of the X-ray radiation field. A brief introduction to the interaction of electromagnetic waves with matter is given in the following. It closely follows [Pag06].

Assuming a linear responding material like most dielectric materials, through which an electromagnetic wave propagates, the evolution of the radiation field can be described by a scalar wave equation:

$$\left[\epsilon(x,y,z)\mu_0\frac{\partial^2}{\partial t^2}-\nabla^2\right]\Psi(x,y,z,t)=0 \tag{2.6}$$

with ϵ the local permittivity of the material and μ_0 the vacuum permeability. ϵ contains the material response. The wave field Ψ can be rewritten as an integral of monochromatic fields with angular frequency ω:

$$\Psi(x,y,z,t)=\frac{1}{\sqrt{2\pi}}\int_0^\infty \psi_\omega(x,y,z,t)\exp(-i\omega t)d\omega \tag{2.7}$$

By combining Equation 2.6 and Equation 2.7, an equation for each component ψ_ω can be obtained:

$$\left[\nabla^2+k^2n_\omega^2(x,y,z)\right]\psi_\omega(x,y,z)=0 \tag{2.8}$$

The refractive index n_ω can be rewritten using the wave number k and the speed of light in vacuum c

$$n_\omega(x,y,z)=c\sqrt{\epsilon_\omega(x,y,z)\mu_0},\quad k=\frac{\omega}{c}. \tag{2.9}$$

n_ω is generally a complex number and can be written as:

$$n_\omega=1-\delta_\omega-i\beta_\omega \tag{2.10}$$

For a wave propagation in z-direction through an object with a refractive index n_ω, wave equations like Equation 2.8 can be solved using a plane wave ansatz [Bor99]:

$$\psi_\omega(x,y,z)=\psi_{0,\omega}\exp(-in_\omega kz)=\psi_{0,\omega}\underbrace{\exp(-ikz)}_{\text{vaccum propagation}}\underbrace{\exp(-k\beta_\omega)}_{\text{attenuation}}\underbrace{\exp(ik\delta_\omega z)}_{\text{phase shift}} \tag{2.11}$$

The first term in Equation 2.11 is the vacuum propagation of the wave. The second term describes the attenuation of an X-ray beam in matter as analogous to the description in section 2.2. The third term is a phase term, which describes the change of the phase oscillation by a phase shift $ik\delta_\omega z$ due to the presence of matter. This change can not be seen in the description of X-rays as particles given in section 2.2. Using gbpci allows for measuring this phase shift through one of the additional image modalities.

2.4.2. The Talbot effect

Phase shifts can not be measured directly. Instead, interference phenomenons are used to indirectly measure the influence of the phase shift on the wave field. The Talbot effect ([Tal36]) is an interference phenomenon, where a periodic structure creates images of itself in certain distances behind the structure when illuminated with a spatially coherent source. These special distances are called Talbot-distances. For a plane monochromatic wave and absorption gratings, the Talbot-distances are [Pag06]

$$d_{\mathrm{t}}^m=\frac{mp^2}{\lambda}, \tag{2.12}$$

where m is an integer, λ the wavelength of the incident light and p the period of the grating. An important property of a Talbot pattern is its visibility defined as [Pag06]:

$$V = \frac{I_{\text{max}} - I_{\text{min}}}{I_{\text{max}} + I_{\text{min}}} \tag{2.13}$$

with I_{max} and I_{min} the maximum and minimum measured intensity of the pattern. The visibility is a measure for the contrast of the Talbot pattern, how much lighter the light areas of the pattern are compared to the dark areas.

The aforementioned absorption gratings, produced for example from gold with a large structure height block most of the transmission at the location of the grating bars. A different type of gratings called phase gratings, is also used in grating-based X-ray phase-contrast imaging. An ideal phase grating only shifts the phase of a wave but does not absorb it. The grating structure imprints a phase shift onto the passing wave and the Talbot pattern is produced by self interference of the wave due to its varying phase. The different properties of phase gratings compared to absorption gratings are sometimes advantageous in grating-based X-ray phase-contrast imaging.

Since the Talbot effect is an interference phenomenon, a high spatial coherence of the source is required for it to work. This can be ensured by choosing a sufficiently small source, like the focal spot of a microfocus X-ray tube. In this case, the X-rays are emitted in a cone beam geometry, causing a magnification of the Talbot pattern with increasing distance from the focal spot [Eng+07].

Wave fields with polychromatic components, such as from X-ray tubes, create a Talbot pattern for each energy component. In this polychromatic case, a superposition of all individual Talbot pattern is measured. Each pattern has its own Talbot distances, smearing out the total measured intensity and thereby reducing the visibility.

2.4.3. The Moiré effect

For gratings used in gbpci, with periods in the order of magnitude of 10 µm, the small shifts in the periodic structure due to the phase shift caused by an object, are not spatially resolved by typical X-ray detectors with pixels of equal or larger size. A second grating, called G_2 or analyser grating, is placed close to a Talbot distance of G_1 to observe the change in the intensity distribution. In the polychromatic case, any energy component's Talbot distance with sufficient visibility can be used. Two methods are available to measure the intensity distribution with this analyser grating. The first method is called phase stepping. It involves sampling the Talbot pattern with analyser grating, by moving it in small increments and measuring the change in the intensity pattern behind it. The result is a sinusoidal curve that is compared with a reference image, taken without an object in the interferometer. For a more detailed description see [Lud20], [Sch16] or [Sei20].

The method used in this thesis is called Moiré imaging. It uses the fact that the periodic Talbot pattern and the analyser grating G_2 interact when overlaid and form a new periodic structure called a Moiré pattern [Ami09]. If the period of the analyser grating

p_{G2} and the period of the Talbot pattern p_{T}, at the location of the analysing grating, are roughly equal, the period of this structure p_{m} is given by [Ami09]:

$$p_{\mathrm{m}} = \frac{p_{\mathrm{T}} p_{\mathrm{G2}}}{\sqrt{p_{\mathrm{T}}^2 + p_{\mathrm{G2}}^2 - 2 p_{\mathrm{p}} p_{\mathrm{G2}} \cos(\theta_{\mathrm{T}} - \theta_{\mathrm{G2}})}}, \quad p_{\mathrm{T}} \approx p_{\mathrm{G2}} \tag{2.14}$$

The angular difference $\alpha = \theta_{\mathrm{T}} - \theta_{\mathrm{G2}}$ is the angle between the grating bars of both gratings. The Moiré period for three different grating configurations is plotted over the angle α in Figure 2.5. As can be seen, depending on the match of the periods p_{T} and p_{G2}, the Moiré pattern period can be orders of magnitude larger than the Talbot period, making it easier to resolve. Figure 2.5 also shows the importance of matching the analyser period to the Talbot period, as the maximum possible magnification of the Moiré pattern period is larger, the smaller the mismatch is, and falls off quickly for even small mismatches.
The angle of the Moiré pattern depends on the angles of the gratings [Ami09]:

$$\varphi_{\mathrm{m}} = \arctan\left(\frac{p_{\mathrm{G2}} \sin(\theta_{\mathrm{T}}) - p_{\mathrm{T}} \sin(\theta_{\mathrm{G2}})}{p_{\mathrm{G2}} \cos(\theta_{\mathrm{T}}) - p_{\mathrm{T}} \cos(\theta_{\mathrm{G2}})}\right). \tag{2.15}$$

All angles are defined as in Equation 2.14 and measured relative to the same but arbitrary axis. The Moiré hence pattern depends on the Talbot period, analysing grating period and the relative rotation of G_1 and G_2. This enables fine control of the pattern's direction and period. While changing the angles can be achieved by tilting the gratings, the period of G_2 can be indirectly adjusted relative to the Talbot period by changing the distances and therefore the magnification of the gratings.
The phase shift caused by an object changes the Talbot pattern. As a result, the Moiré pattern also shifts. Hence, the information about the relative phase shift is transferred via the Talbot pattern to a change in the Moiré pattern, where it can be measured more easily.

2.4.4. Image acquisition, retrieval and modalities

The change in Moiré pattern encodes the information required for retrieving the additional image modalities in gbpci called differential phase contrast and darkfield image. They are available in addition to the attenuation image. Two images are required to perform Moiré imaging. One image with the object, the object image, and one without any object in the beam path, the reference image. The method used is first described for visible light in [TIK82]. For X-rays the method is described in [Ben+10] and [Bev+12]. In the following, the retrieval process is explained, before the three image modalities are described in more detail. The example reconstruction is performed on a sample image containing a 3-D printed object shaped like the logo of the Erlangen centre for astroparticle physics. The lettering, thin lines and outer area are extruded to a thickness of 5 mm, 3 mm and 2 mm respectively [Die19]. A part of one of the gratings used to image the object is damaged. No Moiré pattern is produced in the damaged area, allowing to see which of the image modalities require the pattern.

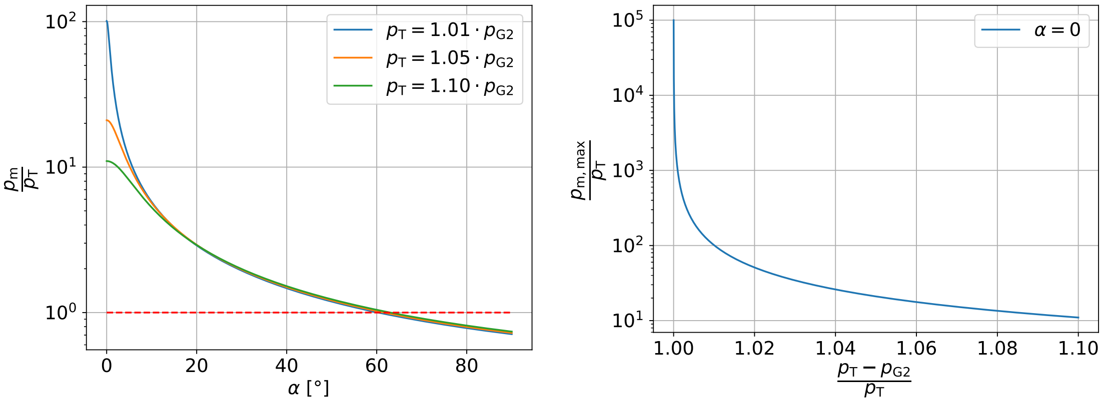

(a) Period of the Moiré pattern from two gratings depending on the angle between them. Plotted are three different relative period proportions between the Talbot pattern and the analyser grating.

(b) Maximum period of the Moiré pattern achieved at 0° relative angle, depending on the relative mismatch of individual periods between Talbot pattern and analyser grating.

Figure 2.5.

The steps of the reconstruction algorithm are also shown in Figure 2.6. First, both the object, denoted as “obj”, and the reference frame, referred to as “ref”, are Fourier transformed ($\mathfrak{F}$). The transformation yields an image of the spatial frequencies. Three peaks are prominent: One at the centre of the Fourier image, where the spatial frequency is zero. Hence, this is called the zeroth order Fourier peak. It contains all the non-periodic contents of the image, for example the standard attenuation information. The other two peaks are the first order peaks at the spatial frequency of the Moiré pattern. One peak has a positive sign, the other has the same magnitude at a negative frequency. Both encode the Moiré pattern.

A cut within the Fourier spectrum is now applied to separate the Moiré pattern from the other information and two new pixel arrays can be obtained for each of the original images ([Sei+18]): One that contains only one of the first order peaks, $\mathfrak{F}_{1,\mathrm{ref/obj}}$, and $\mathfrak{F}_{0,\mathrm{ref/obj}}$ containing the zeroth order peak. These four arrays are now transformed back ($\mathfrak{F}^{-1}$). At this stage, each pixel contains a complex number. The real and imaginary parts of the different arrays are used to retrieve the image modalities:

Attenuation The attenuation image contains information about the absorption of X-rays within the object. It is similar to the images obtained by standard X-ray radiography. The attenuation image is reconstructed analogous to [Bev+12] via

$$\mathrm{T} = \frac{\left|\mathfrak{F}^{-1}_{0,\mathrm{obj}}\right|}{\left|\mathfrak{F}^{-1}_{0,\mathrm{ref}}\right|} \tag{2.16}$$

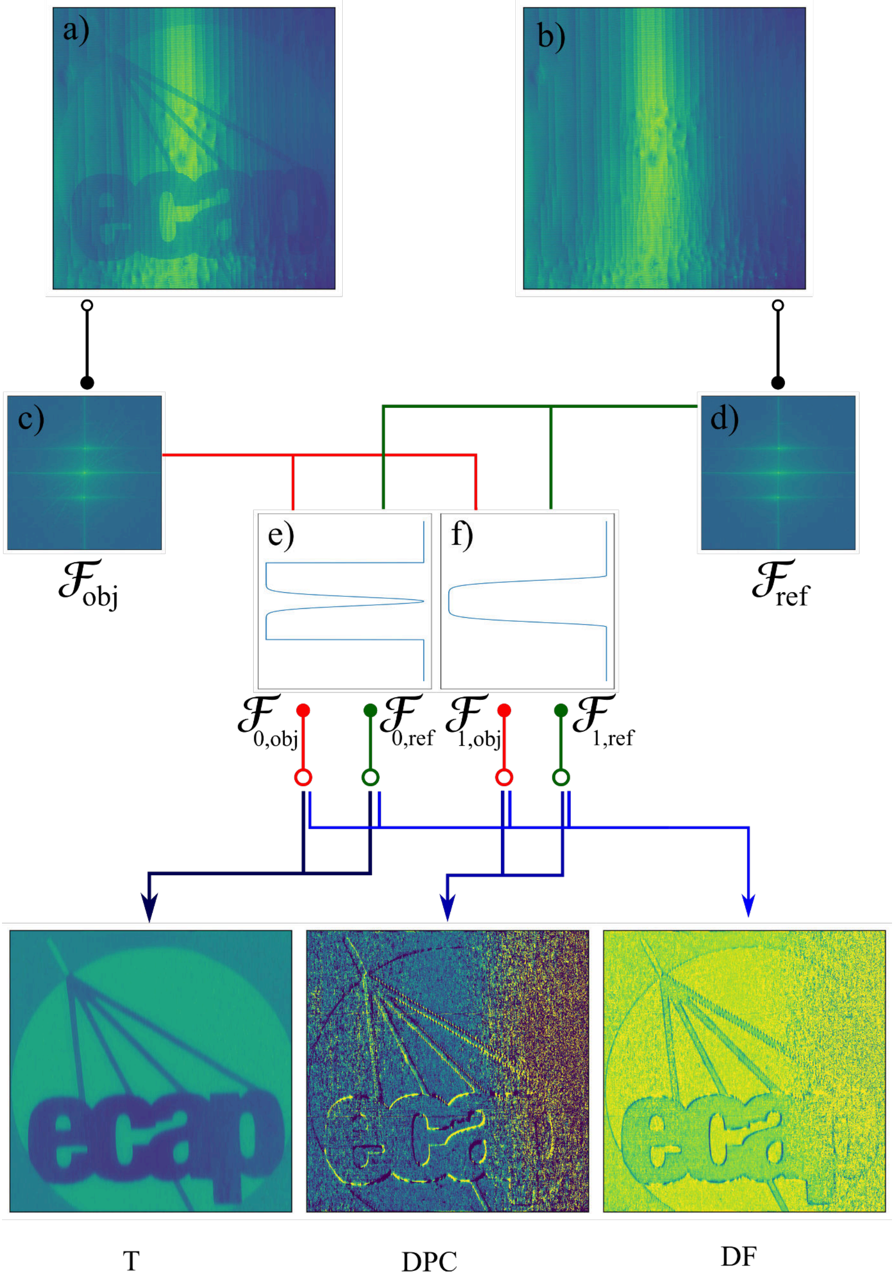

Figure 2.6.: Flowchart of the reconstruction process for Moiré imaging. The process starts at the top with an object image (a) on the left side and a reference image (b) on the right side. Both are Fourier transformed. Shown here are the moduli of the complex Fourier transforms (c, d, shown are 1D projections). The transformations are then multiplied with two different filters (e, f), splitting each into two new arrays. These arrays are transformed back and combined in different ways to retrieve the image modalities **T**ransmission, **D**ifferential **P**hase **C**ontrast and **D**arkfield. A detailed explanation of the individual steps can be found in the text. One of the gratings is damaged, causing the reconstruction to fail in the right third of the DPC and darkfield images.

from the absolute values of the back transformed zeroth order peaks. The division by the reference $\mathfrak{F}^{-1}_{0,\mathrm{ref}}$ serves to normalise the pixel values. In this form, highly absorbing materials will be seen as areas with values close to zero. Areas where little to no absorption takes place will produce pixel values close to one. This convention creates a linear mapping between absorption and pixel value. Since the reconstruction of the attenuation image uses only zeroth order information, the damaged grating on the right side of the image in Figure 2.6 has no negative influence.

Differential Phase Contrast The Differential Phase contrast (DPC) image can be retrieved using [Bev+12]:

$$\Delta\Phi = \Phi_{1,\mathrm{ref}} - \Phi_{1,\mathrm{obj}} = \arg(\mathfrak{F}^{-1}_{1,\mathrm{ref}}) - \arg(\mathfrak{F}^{-1}_{1,\mathrm{obj}}). \tag{2.17}$$

In Equation 2.17 arg is the complex argument calculated from the imaginary and real part by:

$$\arg(\mathfrak{F}^{-1}_{1,\mathrm{i}}) = \arctan\left(\frac{\mathrm{Im}\left\{\mathfrak{F}^{-1}_{1,\mathrm{i}}\right\}}{\mathrm{Re}\left\{\mathfrak{F}^{-1}_{1,\mathrm{i}}\right\}}\right), \quad i \in (\mathrm{ref}, \mathrm{obj}). \tag{2.18}$$

The DPC image is sensitive to a change in thickness of the object [Pag06]. This effect can be seen in the DPC image in Figure 2.6: Areas where no target is present share their differential phase value with areas where a target of constant thickness is present. The edges, where the thickness changes rapidly, produce an easily visible signal within the DPC image. Due to the mono-directional nature of the gratings, the DPC image only shows components of gradients perpendicular to the orientation of the grating bars. Gradients perfectly parallel to the bars would produce no signal. The reconstruction of the DPC image relies on the first order peaks, so the quality of the reconstruction depends on the quality of the gratings as seen in the right area of the DPC image in Figure 2.6, where one of the gratings is damaged. In this area, the retrieval fails.
The relative phase shift $\Delta\Phi$ is related to the real part of the refractive index $\delta(z)$ of the imaged object via (see [Hof18] or [Sch20]):

$$\Delta\Phi = \frac{d_\mathrm{T} \cdot 2\pi}{p_{\mathrm{G2}}} \frac{\partial\varphi}{\partial x} \frac{\partial \int_0^{d_{\mathrm{obj(x)}}} \delta(z) dz}{\partial x} \tag{2.19}$$

Here, d_T is the Talbot distance at which $G2$ is placed, p_{G2} the period of the analyser grating and $\dfrac{\partial\varphi}{\partial x} = k_x$ the x-component of the wave vector. Furthermore, the refractive index depends on the electron number density ρ_e [Pag06]

$$\delta(z) = \frac{r_\mathrm{e}}{2\pi}\rho_\mathrm{e}(z)\lambda^2, \tag{2.20}$$

with r_e the classical electron radius and λ the wavelength of the X-rays. Hence, the data in the DPC image can be used to obtain information about the spatial distribution of electrons in the imaged object.

Darkfield The Darkfield image can be reconstructed by [Bev+12]:

$$\mathrm{DF} = \frac{V_{\mathrm{obj}}}{V_{\mathrm{ref}}}, \quad V_i = \frac{\mathfrak{F}^{-1}_{1,i}}{\mathfrak{F}^{-1}_{0,i}}, \quad i \in (\mathrm{ref}, \mathrm{obj}) \tag{2.21}$$

It measures the decrease in visibility due to the presence of the object. It is particularly sensitive to small angle scattering in the object often produced by fibres, pores and small cracks in the material. The darkfield also relies on information from the first order peaks, hence in the example image in Figure 2.6, where a damaged grating was used, the right side of the darkfield image is damaged as well.

3. Angular X-ray transmission measurements

The retrieval process in Figure 2.6 shows that the quality of the obtained images relies on the quality of the gratings used. Apart from the large and obvious damages, gratings can also have smaller defects or variations of their parameters. In [Gus+19] and [Sch+16] a method for finding such grating defects and evaluating the absorber height, the duty cycle and the absorber inclination angle of absorption gratings is described. The method relies on the change of transmission through a grating depending on the angle of the absorbing structure relative to the incident X-ray radiation. This method, called Angular X-ray transmission (AXT) measurement, allows for local characterisation of the grating structures over large grating areas with standard X-ray radiography equipment, without the need of specialised instruments like electron microscopes. The following chapter explains AXT measurements and introduces a method for improving the spatial resolution of the obtained parameter maps.

3.1. Grating Parameters

A line grating consists of grating bars with a structure width b on a substrate. The grating bars are placed at a grating bar distance d from each other, the empty space between grating bars is filled with photo resist. The grating period p is calculated as the sum of structure thickness and grating bar distance. A sketch of a grating with these parameters of a line grating can be found in Figure 3.1.

The height of the absorbing structures determines how much of incident X-ray radiation is absorbed by the grating bars, following the Lambert-Beer law (Equation 2.5). Higher photon energies hence require greater structure height to achieve the same absorption as with lower energy photons.

An ideal line grating has perfectly parallel grating bars that are perpendicular to the substrate upon which the grating is built. In a real grating, the absorbing structures may be slightly tilted by an inclination angle α, effectively reducing the absorber height and increasing the absorber width at these bars. For gratings with high aspect ratios, meaning a high ratio of structure height over grating bar width, even a small deviation from the perfect inclination angle can decrease the usability of the grating due to decreased transmission [Gus+19].

The duty cycle is defined as the proportion of grating area with absorbing structure compared to the total grating area. It can be calculated from the structure with and grating bar distance via:

$$DC = \frac{b}{p}. \tag{3.1}$$

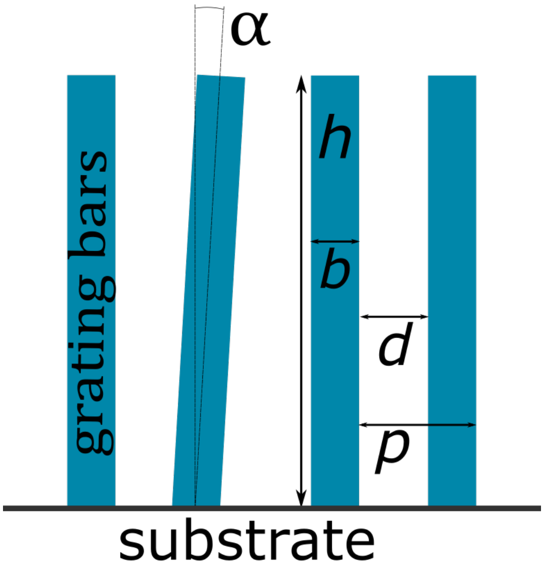

Figure 3.1.: Side view onto a grating structures consisting of the grating bars (blue) and the substrate at the bottom. The annotations mark the grating parameters structure height h, absorber inclination α, structure width b, grating bar distance d and period p.

AXT measurements allow for the evaluation of duty cycle, absorber height and absorber inclination. The method requires knowledge of the grating period, that has to be obtained through different means.

3.2. Method

AXT measurements rely on the change of the projected height profile with varying incident angle of X-rays ([Sch+16]). The varying incidence angle is achieved by rotating the grating parallel to the grating bars. The change in projected height profile due to the rotation of a grating, along with the resulting transmission through the grating, is illustrated in Figure 3.2. For a parallel beam, or a small area of the grating, where the incidence angle of a cone beam does not change significantly, the height profile starts out as a series of rectangular functions, just as the grating itself (Figure 3.2 a)). At increasing angles, the height profile changes towards a series of triangular functions (b)). The triangular state is reached at the following angles [Sch+16]:

$$\varphi_{\text{triangular},n} = \tan^{-1}\left((n + DC)\frac{p}{h}\right),\ n \in \mathbb{N} \tag{3.2}$$

At higher tilting angles, the overlap of neighbouring grating bars increases further, until a uniform effective height profile (c)), consisting of a single rectangular function, is approached. The angles at which this happens are given by [Sch+16]:

$$\varphi_{\text{uniform},n} = \tan^{-1}\left(n \cdot \frac{p}{h}\right),\ n \in \mathbb{N} \tag{3.3}$$

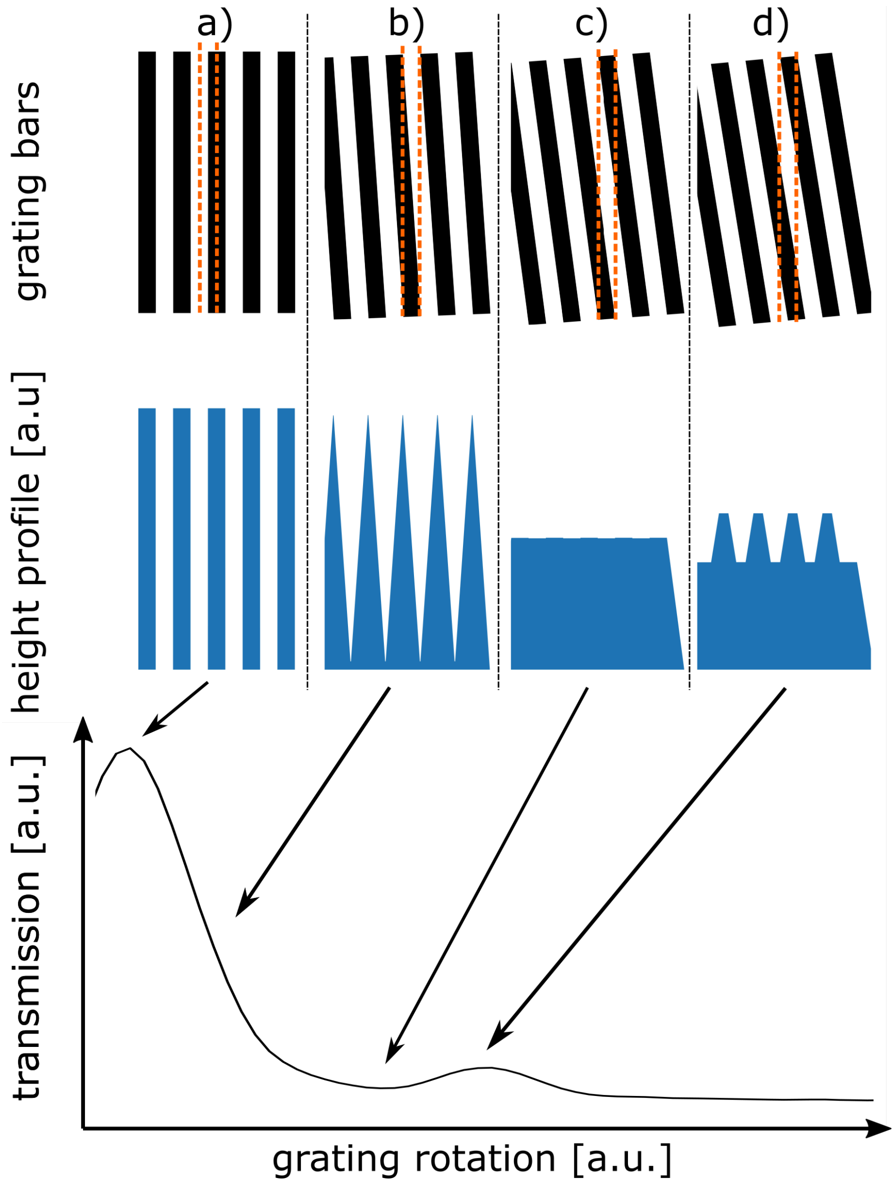

Figure 3.2.: Sketch of the angular X-ray transmission principle. Shown in the top row are grating bars at different rotation angles and path of incident X-rays through the grating bars as orange lines. The row below shows the resulting effective height profile seen by the X-rays for each rotation point. The last row shows the transmission curve expected from illuminating the grating at different angles. The arrows denote transmissions corresponding to the rotation points in the upper half of the image. a) and c) correspond directly to the global maximum and local minimum respectively, whereas b) and d) are found in the region denoted by the arrowhead. The figure is adapted from [Sch+16].

Combinations of these shapes are repeated at larger angles (d)).
By illuminating the grating at these varying angles, the changes in the effective height profile can be translated into a change in transmission. The transmission is governed by the Lambert-Beer law (Equation 2.5) and hence depends exponentially on the effective absorber height. The shape of such a transmission curve, in the following called AXT curve, is shown in the last row of Figure 3.2. It consists of a nearly triangular maximum at an angle φ_{m} and two minima at the base. The peak corresponds to the angle at which the X-rays incidence is parallel to the grating structures and the height profile is a series of rectangular functions (a)). Its height is determined by the duty cycle and the inclination angle of the structures. Rotating the grating in either direction reduces the transmission, as the effective absorber thickness increases on average by a factor of $1/\cos(\varphi)$ [Sch+16]. The minima on both sides (c)) of the peak base are located at the angle where the height profile approaches uniformity [Sch+16]. The exact positions depend on the absorber height. For larger rotation angles, local maxima follow. They correspond to angles in the proximity of the triangular height profile [Sch+16].
All information required to retrieve the grating parameters obtainable from AXT measurements is hence contained within the global maximum and the first minima.

3.3. Experimental setup and measurements

The setup for performing AXT measurements consist of three components aligned on an optical axis. It is sketched in Figure 3.3. The grating under test is mounted on a rotational axis in between a detector and an X-ray source. By changing the distance between the detector and the grating, the magnification of the grating can be chosen. The distance between the rotational axis and the X-ray source d_{sg} should be chosen such that it is significantly larger than the change in distance resulting from the rotation of the grating Δx. This ensures that the magnification of the grating does not vary significantly during measurements.
Measurements are taken by illuminating the grating with the X-ray source and measuring the transmission behind the grating as an intensity value in each pixel. Rotating the grating allows for the measurement of the transmission at different angles, thereby obtaining an AXT curve in each pixel. The global maximum and the surrounding local minima need to be sufficiently sampled over the entire grating area, since they contain the important information. Their angular position can be estimated from Equation 3.3 using the design parameters.

3.4. Data processing

After measurements are performed, the data is available in the form of one image for each rotation point, typically around one hundred. Multiple steps are required to obtain the parameter maps for the absorber height, local inclination angle and duty cycle. The entire process of retrieving the parameter maps is sketched in Figure 3.4, and each step is explained in the following.

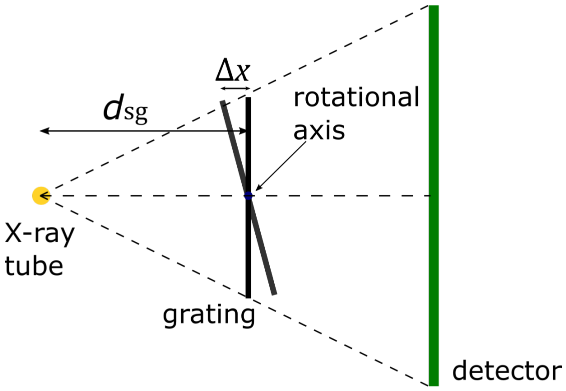

Figure 3.3.: Experimental setup for AXT measurements in a top-down view. The grating (black) is mounted on a rotational axis between the detector (green) and the X-ray source (yellow circle). Rotating it on the axis changes the angle of incidence on the grating surface.

First, the images are **gain and offset corrected**. In a next step, a **wafer gain correction** is applied. The investigated gratings are built on a substrate, for example graphite or PMMA. These substrates contribute to the total absorption. The wafer gain correction is performed by dividing the entire image by the average transmission value of an area containing only the wafer. This removes the effects of the substrate from all the pixels and normalises the transmission to the wafer transmission. Without this correction the duty cycle can not be properly determined, as it relies on the average transmission through the grating bars.

The rotation of the grating results in a distortion of the projection of the grating in the detector plain. The amount of distortion depends on the rotational angle and the magnification. A result of the distortion is a shift of position of grating points in the detector. For larger rotation angles, the image of the grating is squeezed and points are shifted towards the rotational axis. An example of this effect is shown in Figure 3.5a. The position of the grating edge in the two images is misaligned, the edge is shifted about 20 pixels towards the centre of the image at 7.1°.

3.4.1. Projective correction

The shift causes a blur in the resulting parameter maps, since data from multiple grating points now contribute in each pixel. To counteract this undesired phenomenon, a projective correction is applied. This correction aims to remap the pixel values of the images of the rotated images back to their original position, such that each pixel corresponds to the same area within the grating in all images.

First, a **scaling factor** f_s is calculated for each image from the rotation angle φ of the grating:

$$f_{\mathrm{s}} = \frac{1}{\cos(\varphi)} \tag{3.4}$$

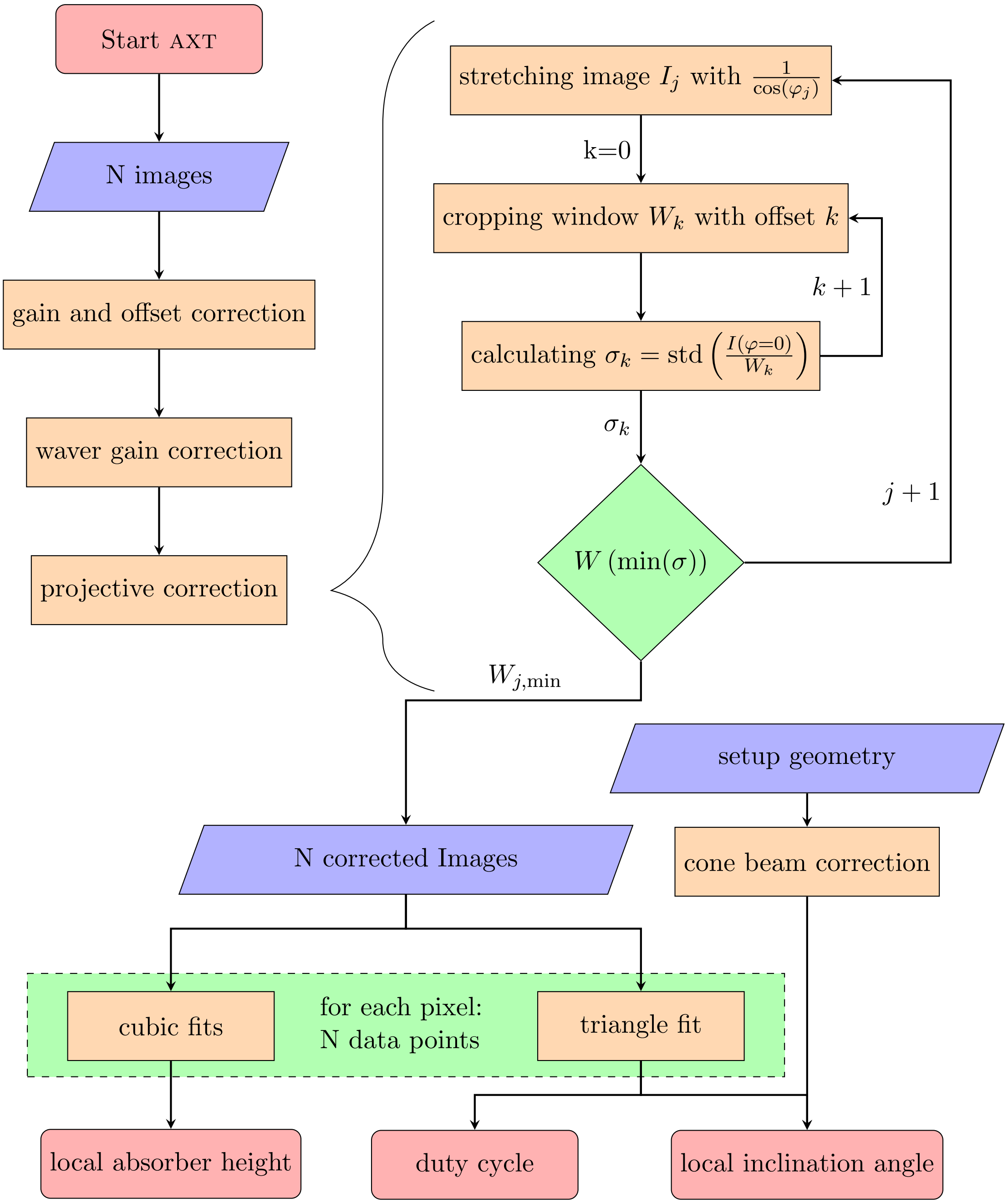

Figure 3.4.: AXT data flowchart showing the steps required for the retrieval of the parameter maps. The steps can be grouped in three major sections. First, different gain and wafer corrections are applied to the images. Then, the projective correction is applied. Finally, fits are performed to the corrected data and the parameter maps are obtained. A detailed explanation of each individual step can be found in section 3.4.

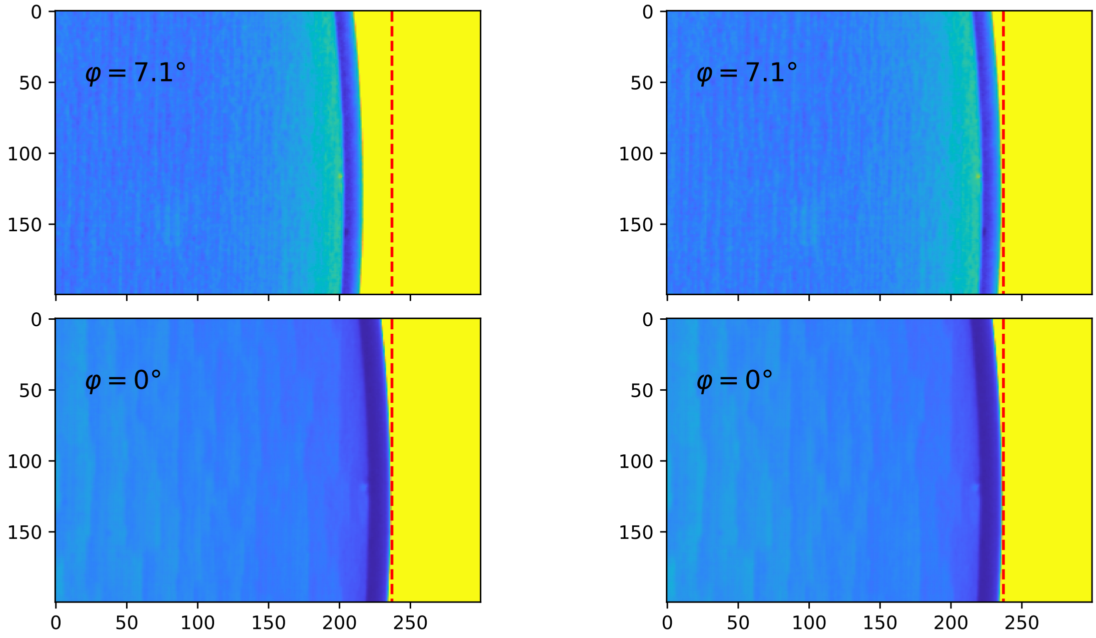

(a) Right edge of the grating at two different rotations φ without the application of the projective correction.

(b) Same image area as in a) after application of projective correction. The grating is stretched back to its original dimension.

Figure 3.5.: Effect of the projective correction. All images show transmission images of the same area.

The image at $\varphi = 0°$ is left in its original state and is used as a reference image. All other images are **resized** with the scaling factor, stretching them to a size larger than the original image. The grating area within the resized images is now stretched to be the same size as in the reference image at 0°. If the position of the rotational axis is known exactly, the resized image can be cropped symmetrical to the axis back to its original size. However, the position of the rotational axis within the images is often not known and the rotational axis could be offset from the grating plane, causing additional distortions. Hence, a matching algorithm instead of the approach in [Gus+19], that uses only the setup geometry, is employed.

Each resized image is **cropped** back to its original size using a sliding window approach. First, a window centre is chosen in a way, that the window fits wholly inside the stretched image. The cropped image is saved, and the window centre is moved to the next pixel. This procedure is repeated until all possible window centres have been realised.

Each cropped window is then compared with the reference image. The image that is the most similar is chosen and saved for further analysis, all other windows are discarded. For images with clearly visible structures such as the grating mounts, the following algorithm has proven viable for determining the image that is the most similar: The window is divided by the reference image, then the **standard deviation** of this matrix is taken as measure for similarity. The window with the **lowest standard deviation** is chosen as the one that is the most similar to the reference image. The result of this correction and matching can be seen in Figure 3.5b, where the right edge of the grating area of the 1626-grating is shown at two different rotation steps, 0° and 7.1°. The position of the edge aligns very well, compared to Figure 3.5a, showing the same area for the same rotational steps, but before the correction is applied. The sliding window correction is performed on all but the reference image.

3.4.2. Fits to the image data and grating parameter retrieval

After the projective correction, each pixel corresponds to the same grating area at all rotation angles. The change of transmission with varying rotation angle contains the local information about absorber height, inclination angle and duty cycle. To retrieve the information, two kinds of fits are applied to each AXT curve $I_{x,y}(\varphi)$ of pixel coordinates x and y over the rotation angle φ.

By fitting appropriate functions to the data, grating parameters can be determined automatically. The fits are performed for each AXT curve using the fitting algorithms provided by scipy. The returned fitting parameters are then saved in an image like pixel matrix with the same dimensions as the original images, before they are used for grating parameter retrieval. Gustschin et al. propose in [Gus+19] the usage of a **triangular fit** close to global maximum, so the function

$$\Lambda(\varphi, a, b, c) = a \cdot (1 - |b \cdot \varphi - c|) \tag{3.5}$$

is used.

Duty cycle: The duty cycle can be calculated from the triangular fit using the height a. For absorption gratings, the height of the absorbing structures is high enough to completely absorb the X-ray radiation behind the grating bars. Hence, the transmission of the entire grating only depends on the ratio of absorbing area to non-absorbing area, which is the duty cycle. Since the images are already gain- and wafer-gain corrected, a is a value in the range of $[0, 1]$ and corresponds to the maximum amount of transmission of the grating relative to the transmission of only the wafer. The duty cycle is then calculated as

$$DC = 1 - a \tag{3.6}$$

This formula only holds for sufficiently low energies. At higher energies, the penetration power of X-rays increases and a higher proportion of the radiation can pass through the grating bars resulting in an incorrect determination of the duty cycle.

Local inclination angle: Maximum transmission through the grating is expected, when the X-ray beam impinges parallel to the grating bars. The angle, at which the triangle fit reaches its maximum is

$$b \cdot \varphi_{\mathrm{m}} = c \Rightarrow \varphi_{\mathrm{m}} = \frac{c}{b}. \tag{3.7}$$

Due to the cone beam geometry of X-ray tubes, the incidence angle of the X-ray beam varies over the grating area. Hence, ϕ_{m} is not the local absorber inclination. A cone beam angle correction as explained in subsection 3.4.3 is necessary to retrieve the local absorber inclination in this case.

The fits to the local minima are performed using a **cubic polynomial** of the form

$$P_3(\varphi, a, b, c, d) = a \cdot \varphi^3 + b \cdot \varphi^2 + c \cdot \varphi + d, \tag{3.8}$$

since it is the lowest order polynomial that can replicate the local minimum and the neighbouring local maximum. Example fits are shown later in section 3.5.

Local absorber height: The height of the absorbing structures is retrieved by using the cubic fit, specifically the local minimum, and Equation 3.3. The fit is used to determine the angle φ_{min} at the position of the minimum. Its distance $\Delta\varphi$ to φ_{m}, the angle with maximum transmission, can be used in Equation 3.3 to obtain:

$$h = \frac{p}{\tan(\Delta\varphi)} \tag{3.9}$$

where n is set to one, since the first minimum is used. The AXT curves contain two first order minima. Either can be used for the analysis. Due to noisy measurements, the determination of a minimum can be difficult, using both minima and averaging the distance yields more reliable results than relying only on one of the minima.

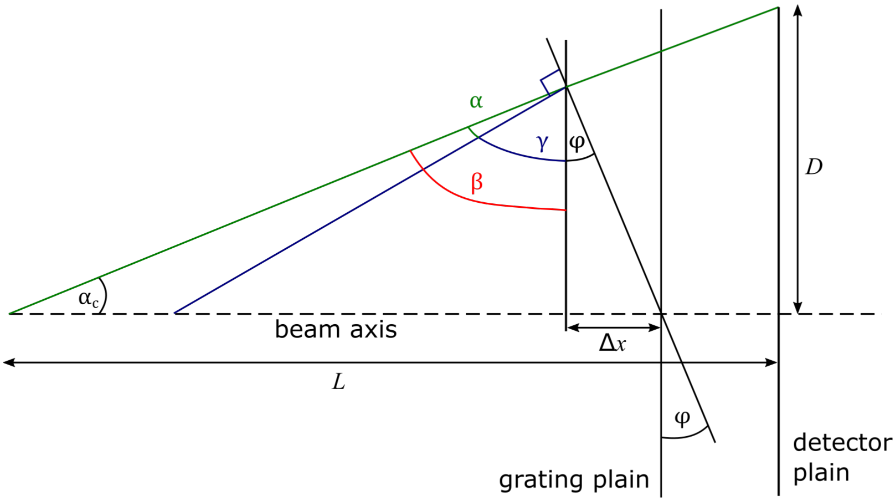

Figure 3.6.: Sketch of the angles and distances used for the retrieval of α and the cone beam correction. The grating is shown under the rotation angle φ. The grating point is projected into the detector plane at a distance D from the beam axis. L is the distance between source and detector. β and γ are auxiliary angles, that help in calculating α.

3.4.3. Cone beam correction

The second correction required due to the magnifying geometry of the setup is the cone beam correction. It accounts for different incident angles of the X-rays onto the grating for points far from the beam axis. The influence of this correction is limited to the results of the inclination angle α, since it is the only parameter obtained by AXT measurements that uses absolute angles.

Figure 3.6 shows the geometry on which the correction is based. All the following calculations assume, that Δx, the change in distance of the grating from the source, is significantly smaller than L, the distance between source and detector, and the distance between the grating and the source. In this case, the magnification of the grating can be assumed to be constant over the grating and all rotation angles. For a grating with dimension of five by five centimetres and a typical maximum rotation of ten degrees, Δx is about

$$\Delta x = 2.5\,\mathrm{cm} \cdot \sin(10^\circ) \approx 0.5\,\mathrm{cm}, \tag{3.10}$$

so significantly smaller than typical source grating distances of several tens of centimetres. Hence, the condition is easily fulfilled and small-angle approximation can be used.

The cone beam angle α_c is the angle at which radiation impinges onto the grating and detector plain, it can be calculated as:

$$\tan(\alpha_c) = \frac{D}{L} \tag{3.11}$$

where D can be calculated from the pixel pitch of the detector d_p and the distance from the beam axis in pixels n via

$$d = n \cdot d_\mathrm{p}. \tag{3.12}$$

L is the distance from source to detector. The local absorber inclination α is then the angular distance between the grating normal and the grating plain γ and β, the angle between the beam and the grating plain:

$$\alpha = \beta - \gamma \tag{3.13}$$

By using the right triangle, β can be expressed in the form of:

$$\beta = 180^\circ - \alpha_\mathrm{c} - 90^\circ \tag{3.14}$$

Furthermore, γ can be rewritten using:

$$\gamma = 90^\circ - \varphi_\mathrm{m} \tag{3.15}$$

Combining Equation 3.14 and Equation 3.15 and considering the sign of α is negative, due to it being defined clockwise, yields a corrected formula for the local absorber inclination angle:

$$\alpha = \alpha_\mathrm{c} - \varphi_\mathrm{m}. \tag{3.16}$$

As before, φ_m is the grating rotation angle at which maximum transmission is measured. The cone beam correction is especially important for grating areas further away from the beam axis, where α_c can reach a few degrees. To correctly apply the cone beam correction, a precise knowledge of the position of the beam axis within the images is required in order to calculate D. The position can be measured by placing a thin object, like a needle, centred on the rotational axis and taking an image.

3.5. Data analysis

The AXT method is used to examine the 1626 grating with a grating period of 6 µm, absorber height of 150 µm and a nominal duty cycle of 0.72 [Sch20]. It is fabricated on a 500 µm graphite wafer and consists of gold grating bars with a design height of 150 µm. In Figure 3.7 a scanning electron microscope image is shown for a section from the 1626 grating. The bright regular structure, that spans the entire image, is a support structure made of photo resist. The cavities within the support structure are filled with gold, seen as the darker areas in between. The grating bars are realised as many shorter grating lamellae, separated by resist bridges, rather than being continuous structures. The lamellae are depicted darker than the resist, indicating that they are recessed between the higher support structure.

Figure 3.7 also shows grating defects. The most prominent defect is in the centre of the image, where in an area of about 100 µm by 40 µm of the support structure is missing. Instead, the area is filled with gold. Other smaller defects can be seen at different locations as irregularities in the pattern, for example bent lamella.

The AXT measurements are performed at the liquid metal jet X-ray tube with 30 kV acceleration voltage, 50 W power and 50 µm spot size. The grating is placed at a distance of 44 ± 1cm from the source, followed by the Dalsa Shad-o-Box detector in a distance

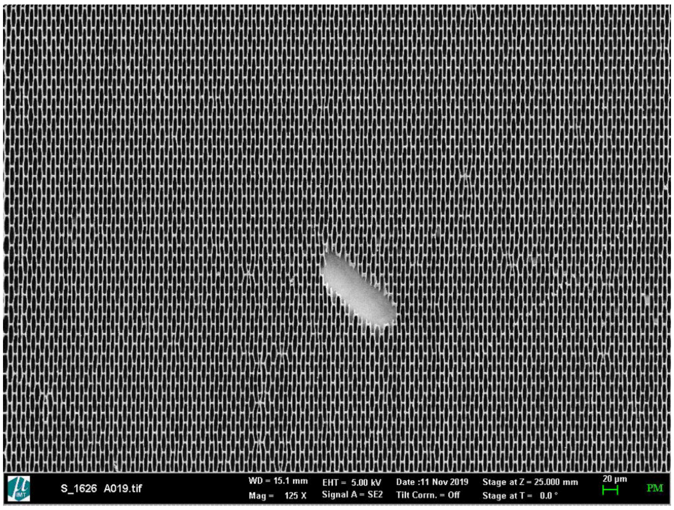

Figure 3.7.: Scanning electron image of a section from the 1626 grating [Pas]. Darker structures are more recessed than brighter structures. The bright regular pattern is the resist structure. The absorbing grating bars sit within the cavities of this structure. Resist bridges separate the grating bars into many smaller lamellae. A large defect, where no resist is present is visible in the centre of the image. The defect is filled with gold.

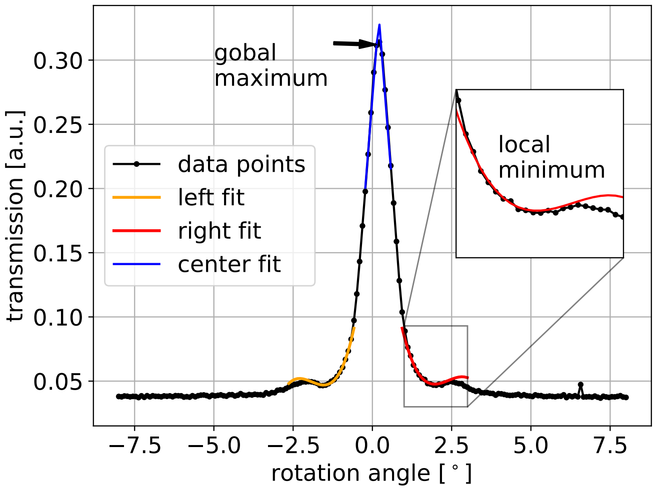

Figure 3.8.: Transmission curve of a centre pixel for the 1626 grating over the grating rotation angle. Clearly visible are the global maximum and the first minimum. The coloured solid lines represent the polynomial fit to the local minimum on the left side (orange), to the central peak (blue) and to the right minimum (red).

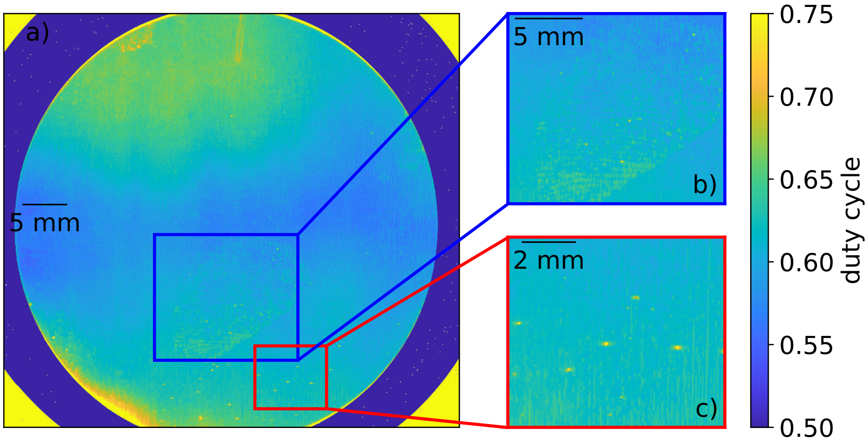

Figure 3.9.: Duty cycle map of the 1626 grating. The Large image shows the entire field of view, smaller images are zoomed image sections as indicated by the coloured rectangles. They contain a fingerprint in b) and grating defects in c).

of $52 \pm 1\,\mathrm{cm}$ from the grating. 180 images are taken over a rotation range of $-8°$ to $8°$. Figure 3.8 shows a sample AXT curve from the top centre area of the grating after all the corrections, including the projective correction, are applied. The curve follows the behaviour expected from the change in height profile, with a prominent central peak surrounded by two local minima. Also shown are the fits required for retrieval of duty cycle, absorber inclination and absorber height.

Figure 3.9 a) shows the duty cycle map over the entire FOV of the detector as determined from the fit to the global maximum in each pixel. The grating is located in the circular region in the centre of image a). It is surrounded by an area containing only the wafer, but no grating. Due to the determination of the duty cycle from the maximum transmission, this area shows values close to zero duty cycle since the maximum transmission of the wafer is set to one by the wafer gain correction. The yellow corners are caused by the grating mount. The thick aluminium blocks all radiation, so the transmission in the corners is zero. Only the duty cycle measurements within the grating region are meaningful and interesting.

A duty cycle between 0.55 and 0.7 is shown in Figure 3.9 a) over the entire grating area. It roughly follows a gradient from the centre towards the upper and lower border of the grating. Areas closer to the centre have a lower duty cycle in the range of 0.55 to 0.6 compared to the border regions, where the duty cycle increases to 0.65. Within the top left corner of the grating the duty cycle is generally the highest. Still, the duty cycle retrieved from the AXT measurements is lower than the design duty cycle of 0.72. The difference is most likely caused by the resist bridges between the lamellae as seen in Figure 3.7. They consist of photoresist and absorb less X-ray flux than the gold lamellae. Hence, the average transmission is increased by the amount of radiation passing through the bridges. This would also explain the gradient. Due to the cone beam nature of the X-ray tube, regions at the upper and lower edge of the grating are illuminated under a

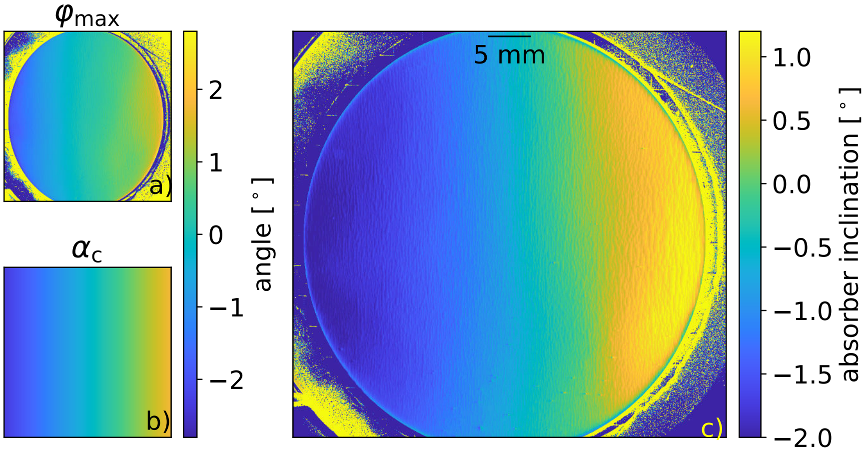

Figure 3.10.: Angle of maximum transmission (a)), cone beam angle (b)) as calculated for the cone beam correction and resulting local inclination angle map for the 1626 grating (c)).

larger angle than the centre regions. The angle prevents the X-ray beam from passing straight through the narrow resist bridges and forces it to at least partially pass through the gold lamellae, decreasing the average transmission. The resist bridges effectively create a second grating perpendicular to the original grating, with a period equal to the length of the gratin lamellae. In effect, a 2D grating is obtained, that shows AXT effects in both directions. The tilting of the grating on one axis does not consider the other. Hence, the gradient in both directions is probably a measurement artefact. The area in the top left corner of the grating shows an additional increase in duty cycle that is larger than explainable by this gradient. It is therefore probably a real difference in duty cycle due to manufacturing tolerances.

Figure 3.9 b) shows a zoomed region of the duty cycle parameter map in a). A fingerprint is visible in this area. The change in duty cycle between the locations of the ridges and in between is very small, yet since the duty cycle is almost uniform in the area, the fingerprint is clearly visible. Figure 3.9 c) shows the section marked with the red rectangle. It contains small spots where the duty cycle is significantly higher than in the surrounding area. The spots have a size of only a few hundred micrometers, showing that the spatial resolution of the AXT method is in the order of magnitude of the pixel size. A source of these spots could be defects like the one seen in Figure 3.7, where the resist structure is damaged and instead gold is deposited. The gold absorbs more of the X-ray flux, reducing the maximum transmission through the defect and subsequently increasing the calculated duty cycle by decreasing a in Equation 3.6. The duty cycle parameter map can hence be used to identify small defects within the grating structure, if they change the absorption significantly, as well as defects that change the duty cycle little, if the surrounding duty cycle is uniform enough. Additionally, large scale deviations of the real duty cycle from the design duty cycle are also made visible.

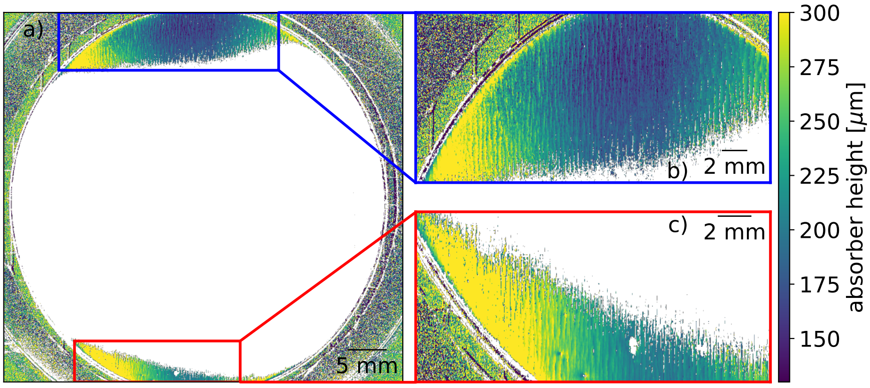

Figure 3.11.: Local absorber height of the 1626 grating. Images on the right half of the figure show the magnified top and bottom area.

Figure 3.10 shows the angle of maximum transmission $\varphi_{\max}$, the cone beam angle α_{C} and the local inclination angle of the 1626 grating as calculated from the former, following Equation 3.16. Like with the duty cycle parameter map, a boundary between the grating area and the wafer area can be seen. A gradient in horizontal direction from angles of about $-2°$ to about $1°$ is visible within the parameter map. The map of $\varphi_{\max}$ looks similar. It also shows the grating area, and the surrounding wafer and grating mount. It contains the same gradient with a slightly higher amplitude. The map of α_{C} is added for reference. It is calculated from Equation 3.11 using the setup geometry and is therefore not limited to the grating area. The gradient in $\varphi_{\max}$ stems from the cone beam geometry and is expected. The fact that it partially remains after the cone beam correction is applied, indicates that a systematic curvature is present, for example due to a curved wafer.

An additional structure can be seen in Figure 3.10 as cracks running from the top of the grating to the bottom throughout the parameter map. It is especially strong and large towards the right edge of the grating, and can also be faintly seen in Figure 3.9 c). The grating is fabricated on a 500 µm graphite wafer and the structure could be cracks within the wafer material. At each crack, the area of the wafer is interrupted and neighbouring sub areas slightly tilt in different directions. These small but sudden shifts are seen as different angles of the absorbing structure built upon the surface, explaining why the cracks are seen more clearly in the absorber inclination map than in the duty cycle map.

The local absorber inclination can also be used to determine the curvature of the wafer, as proposed in [Gus+19], in order to adapt the gratings for cone beam geometry setups. Finding the right curvature could help in maximising the transmission through the grating over its entire width, increasing image quality and increasing the usable grating area.

The last parameter map obtainable with AXT measurements is an absorber height map. For the 1626 grating this height map is shown in Figure 3.11 a). Only two thin bands containing information close to the upper and lower edge of the grating can be seen. These two areas are magnified and depicted in Figure 3.11 b) and c) respectively. The

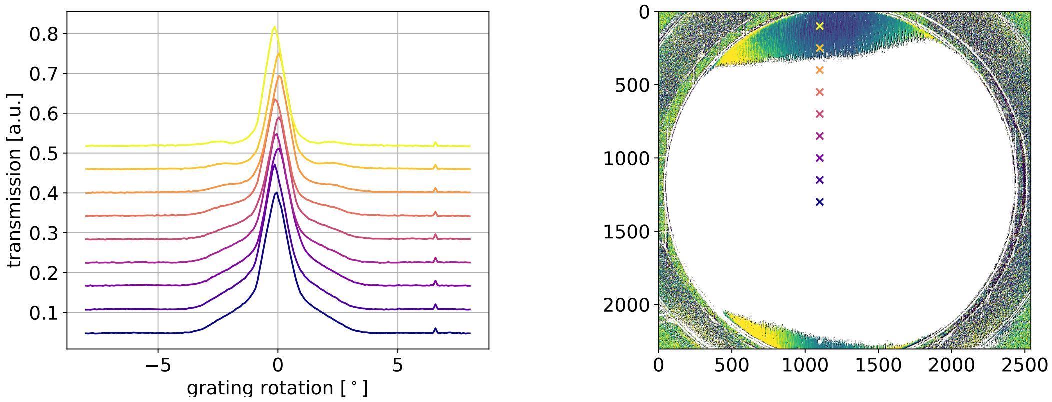

(a) Several AXT curves from the 1626 grating. A clear decline in prominence of the local minimum left or right of the global maximum can be seen for curves from bright to darker curves. Curves are shifted vertically for visual separation.

(b) Height profile map of the 1626 grating. “x” markers show the location of the AXT curves with corresponding colour in left plot.

Figure 3.12.

empty area within the grating is caused by failing calculations of the minima locations, which are most likely caused by the structure of this particular grating.

The values in areas, where the determination of the minima locations worked, are larger than the expected 150 µm. No measurements of the actual absorber height are available however, since a direct measurement using an electron microscope would require the destruction of the grating. Towards the left of both bands, an increase in measured structure height can be seen. Comparing these locations with the duty cycle map in Figure 3.9 reveals structures, that could be responsible for the increase in measured absorber height.

The reason for the failure in finding the local minima in a large area of the grating is found in the AXT curves, Figure 3.12a shows samples. While the expected global maximum is visible in all curves, the local minimum is hardly visible in some curves and clearly absent in most. The curves are taken from the points marked with corresponding colour in Figure 3.12b, where the height map is shown again. Instead of showing a minimum, the base of the AXT curve peak gets wider the closer the origin pixel lies to the centre of the grating, until the area at which the minimum is expected, is replaced by a linear behaviour.

The fit still works for these pixels. Due to the absence of the minima, no real solution for the minima can be found, and the affected pixels are left empty. At points, where a minimum is barely visible, the fit might converge, but the less prominent the minimum the less reliable the result. As a consequence, the fit minima are more prone to deviate from the location of the real minimum. Adding to this problem, the tangent is very sensitive to small changes, so even small shifts can alter the results significantly.

One contribution to the smearing of the minima is noise, drowning out especially the already faint minima. However, the failing of the method in the centre region of grating indicates a systematic origin for these artefacts. The most likely source are the resist bridges mentioned earlier. Made from photo resist, they divide the grating bars into segments and allow for higher average transmission independent of the expected height profile. The angled incidence of X-rays at the upper and lower edges of the grating prevents this transmission and hence, the smearing out of the local minima, whereas in the centre the vertical angle of incident X-rays is almost perpendicular allowing the X-rays to pass through the bridges. This explanation is supported by the fact, that the smearing of the minima gets more prominent in Figure 3.12a the closer to the centre the AXT curve is located.

3.6. Summary and outlook

Angular X-ray transmission measurements provide a method for characterising absorption gratings with resolutions as fine as pixel pitches of x-ray detectors. The data acquisition process can be performed at conventional X-ray imaging systems instead of requiring specialised equipment like electron microscopes. Opposed to characterisation with an electron microscope, duty cycle, absorber inclination angle and local absorber height are accessible without the destruction of the grating. Apart from finding defects as small as a few hundred micrometers, AXT measurements allow for a precise measurement of the grating curvature, helping to improve the image quality in grating-based X-ray phase-contrast imaging, where the gratings are used.

Cone beam X-ray sources and certain grating structures pose additional challenges on the method. While correcting the influence of the cone beam is possible after the measurements are taken, small differences from the ideal absorption grating structure can impact the results and even lead to failure in the determination of the absorber height. A solution to the problems encountered due to the resist bridges in the grating bars requires considering the effective two-dimensional nature of the gratings. This could be achieved for example by performing a two-dimensional AXT measurement, where the grating is tilted along two perpendicular axes to achieve the tilted incidence of X-rays onto the grating surface in both directions for all grating points. The downsides of this approach are a more complicated experimental setup and a higher number of measurement points. The latter point increases measurement times and the amount of data, which in turn complicates the data processing.

4. Detectors for grating-based X-ray phase-contrast imaging

One of the main components of any imaging system is the detector. Its properties are crucial for the quality of the resulting images. The detector should be adapted to the needs of a planned experiment to obtain the best possible results. Often, trade-offs have to be made in order to balance the detector properties like spatial resolution, field of view and noise characteristics with each other. The following section characterises detectors for laboratory and for backlighter experiments with a focus on spatial resolution and noise characteristics.

4.1. Spatial resolution

The spatial resolution of a detector determines its ability to resolve spatially modulated information in images. For pixelated detectors, the spatial resolution depends on the size of the pixels and on signal spread over neighbouring pixels. One way of characterising this spread is the point-spread function. It is defined as the signal produced within the detector under illumination by an ideal point source [Ros69]. When bringing two point sources close together, the signal spread will result in an overlap, until the two sources are no longer distinguishable. The wider the spread, the sooner two signals overlap and the worse the spatial resolution. Similarly, the line-spread function (LSF) can be used as a one dimensional projection of the point-spread function [Ros69]. The LSF is the detector's response to illumination by an ideal line source and can be accessed indirectly using the edge-spread function (ESF), which is the response of the detector to a highly absorbing edge [RPN91].

The LSF fully characterises the resolution in measurement direction. A more commonly used function for comparing detectors is the modulation transfer function (MTF) [EM04], obtained from the LSF using Fourier transform. The MTF describes how well a detector retains image contrast depending on the spatial frequency f within the object. From a given minimum desired length Δs, that needs to be resolved, an equivalent spatial frequency f can be calculated as

$$f = \frac{1}{2 \cdot \Delta s\,[\mu\mathrm{m}]} \cdot 1000 \left[\frac{\mathrm{lp}}{\mathrm{mm}}\right] \tag{4.1}$$

in the commonly used unit line pairs per millimetre (lp/mm). With f known, the MTF can be used to look up the retained contrast, compared to original object contrast. The retained contrast at any given spatial frequency can be easily compared between two detectors.

4.1.1. Slanted-edge method

An established method for the retrieval of the ESF and subsequently the MTF is the so called slanted-edge method (see [Sta21]). The slanted-edge method is adapted and implemented for X-ray detectors following [RPN91], [Bur00] and [EM04] that improve upon the standard method in [Sta21].

The method uses a sharp edge target to determine the ESF. While optical imaging systems can use target phantoms printed on papers, the special properties of X-rays require an edge that can be seen with X-ray attenuation imaging. A tungsten edge of a few millimetres thickness is used for this purpose. By placing it as close as possible to the X-ray sensitive component of the detector, the spatial resolution of the detector can be measured. If the edge is placed further away from the detector, contributions from the extended source spot or its movement negatively influences the measured spatial resolution.

The slanted-edge method requires three different images to be taken. The image containing the edge is taken with sufficiently high exposure time to minimise noise within the image. The standard offset and gain frames are used to correct for systematic differences in X-ray intensities or sensitivities of pixels and are taken with the same integration time as the edge.

The ESF is determined along the X-ray intensity gradient caused by the edge, hence perpendicular to the tungsten edge orientation in the image. In principle, the slanted-edge measurement can be performed for any edge orientation, but the results generally depend on the measurement direction. Hence, a common axis relative to the detector edges, like for example one of the axes parallel to the detector edges, should be used for all detectors.

Figure 4.1a shows an attenuation image of the tungsten edge used for the measurements in this thesis. The left area contains the highly absorbing tungsten plate, the area on the right side contains no absorbing object and shows high transmission values. Also shown in Figure 4.1a is a close up of the transition regions between these two areas. In this zoomed image, the signal spread over several pixels into the edge region can be seen.

Rather than being oriented perfectly vertical in the image, the edge is placed slightly tilted. This is done on purpose and the reasons can be seen in Figure 4.1b, where three different pixel-value rows perpendicular to the edge are plotted. They all show a steep increase from values close to zero to values close to one over a few pixels. This steep increase contains the information required for the retrieval of the ESF. However, two problems are present with the individual rows. First, the edge region is sampled sparsely, where the intensity changes most. Additionally, the data points lie at different relative positions of the real ESF. If the edge were oriented perfectly vertical, all curves would sample the ESF at the same points and the row pixel curves would be similar. However, which points are sampled in this case is dependent on the exact position of the edge. By slanting the edge, different rows of pixels will image the edge at slightly different sub pixel positions. Over the span of a few hundred pixel rows, nearly all relative sub pixel positions are present within the image. This can be used to increase the number of sampling points, by combining the individual pixel rows to a single ESF, from which the

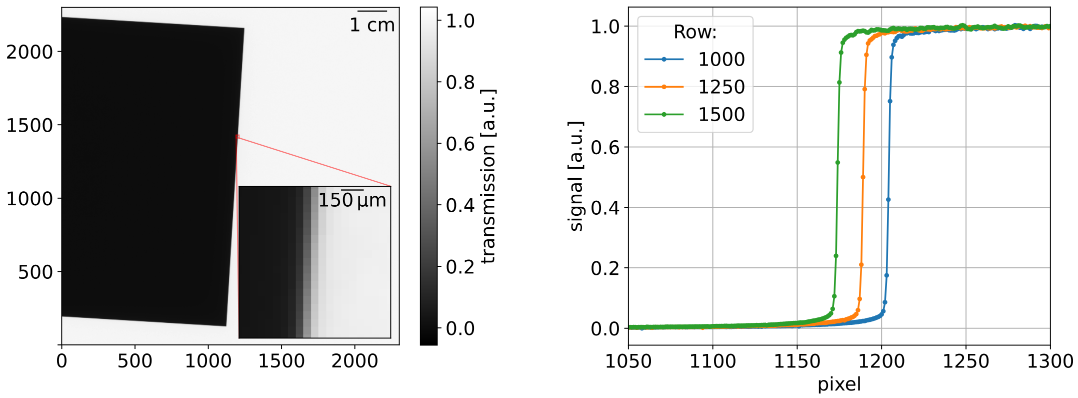

(a) Transmission image of the tungsten edge used in the slanted-edge method for characterising the spatial resolution of detectors.

(b) Plot of the measured signal in arbitrary units over the vertical pixel position. The plot shows different rows of the edge in the left image and their sampling points.

Figure 4.1.

MTF is calculated. The ideal angle of the edge is in the range of three to ten degrees [EM04], the exact angle is not important.

4.1.2. Data processing

The combination of the different individual pixel rows to a single super sampled ESF uses the angle of the edge relative to the pixel edges. Instead of measuring this angle at the time of data acquisition, it is retrieved directly from the images. An edge finding algorithm is employed to determine the exact position of the edge in the image. For each pixel row y, the column x, in which the centre of the edge is located, is retrieved. A linear fit

$$y = m \cdot x + t \tag{4.2}$$

is subsequently performed to this data. The angle of the edge can be calculated from the fit parameters m as $\alpha_{\text{edge}} = \arctan(m)$. Determining the angle in this way, rather than measuring it from the experimental setup, reduces the systematic errors and increases precision.

A region of interest (ROI) is then chosen around the edge. This ROI should contain the entire edge structure in the direction perpendicular to the edge and a sufficient amount of rows in the direction along the edge. The exact amount of rows depends on the noise characteristics of the detector. The more rows are chosen, the smaller the influence of noise on the results. At least one hundred rows have proven to be a lower limit during experiments conducted for this thesis.

The width of this ROI is then super sampled to combine the different pixel rows into a single ESF. A super sampling factor n is chosen with which the number of columns in

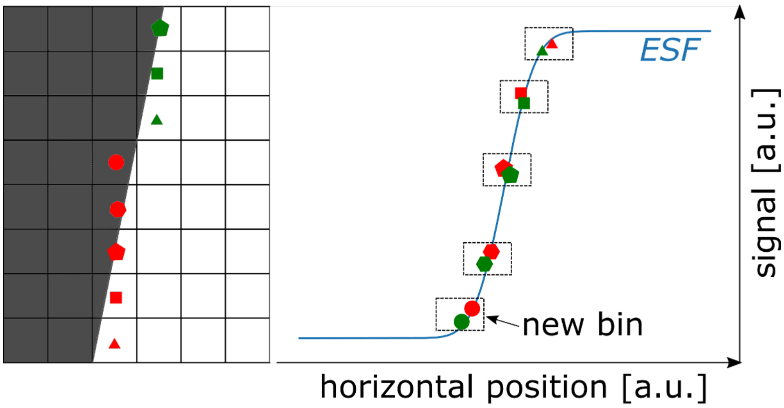

Figure 4.2.: Schematic sketch of the rebinning process. The left image shows the pixel array with the edge overlaid in grey. The pixel values are placed at the right position within the ESF, shown in right image, according to their x and y position. Pixel values with approximately the same illumination are combined into bins, seen as black rectangles. Figure adapted from [EM04].

the ROI n_x is multiplied. The result $n_i = n \cdot n_x$ is the number of bins. Each pixel of the ROI is then sorted in one of these bins i according to its x and y coordinates and the angle α_{edge} of the edge expressed through the fit parameter m from Equation 4.2:

$$i = \left\lfloor n\left(x + \frac{y}{m}\right)\right\rceil . \tag{4.3}$$

Here $\lfloor\rceil$ is the function that returns the nearest integer value. The effect of the sorting and rebinning process is sketched in Figure 4.2 for a small section of the edge. Values from different pixels are collected into bins, such that the illumination of all pixels in each bin is roughly equal. The pixels in each bin now sample the ESF at roughly the same location. At the same time, the number of data points that contain the edge increases from one pixel to four bins in the example shown in Figure 4.2.

Equation 4.3 is valid, if the edge is aligned vertically. For other orientations, the image is first rotated until the edge is aligned vertically. A rotation that is not an integer multiple of 90° requires interpolation. In this case zeroth order interpolation is used, so that pixel values are just copied. In this thesis, only the directions parallel and diagonal to the pixel edges are examined.

The choice of n depends on the noise characteristics and the number of available rows. A high n reduces the number of data points per bin, leading to a higher contribution of noise in the obtained ESF. For a too low n, the number of points at which the ESF is sampled is low. During experiments, an n between the standard of four [Bur00] and six has proven to work. To complete the rebinning process, the content of each bin is averaged.

The resulting ESF is shown in Figure 4.3a. Due to the super sampling, the sampling frequency of ESF in the interesting region, where the signal changes the most, has increased compared to the individual pixel rows in Figure 4.1b. Yet the super sampled ESF retains the behaviour seen for the individual rows.

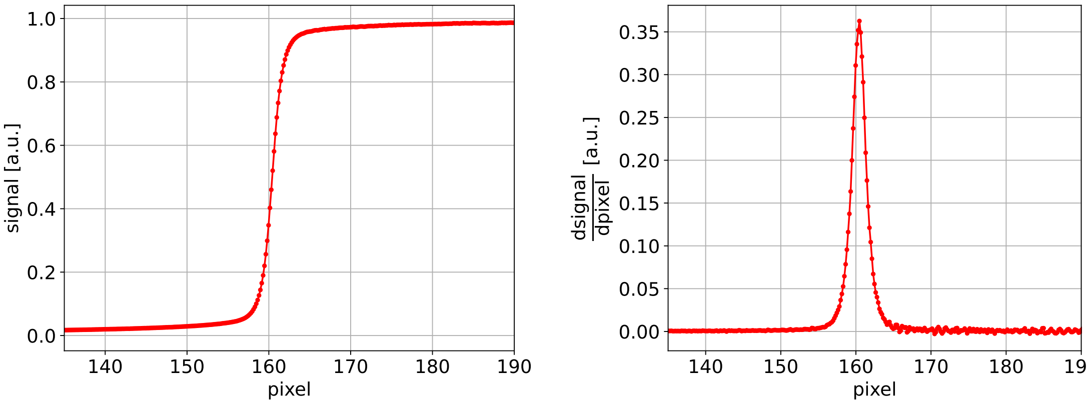

(a) Edge spread function of the Dalsa Shad-o-Box detector as determined with the slanted-edge method. The pixel signal is plotted in arbitrary units against the position in units of pixel.

(b) Line spread function calculated as derivative of the edge spread function in Figure 4.3a. The derivative is plotted in arbitrary units over the position in units of pixel.

Figure 4.3.

The next step is the numerical differentiation of the ESF using the three point derivative numpy.gradient

$$LSF = \frac{\mathrm{d}ESF}{\mathrm{d}x}, \quad \frac{\mathrm{d}ESF_i}{\mathrm{d}x} = \frac{ESF_{i+1} - ESF_{i-1}}{2 \cdot d}, \tag{4.4}$$

yielding the LSF [EM04]. ESF_i are the values of the edge-spread function at sampling point i and d the distance between the evenly spaced sampling points. The fact that a three point derivative is used, will become important later.
As mentioned before, the LSF characterises the spatial response of the detector when imaging an infinitely thin line. Figure 4.3b shows a real LSF. Due to the high number of points around the location of the edge, the sampling frequency of the LSF is high without a strong, visible influence of noise. The peak shows a width at the base of around ten pixels, meaning that in this example the signal is spread over multiple pixels. Apart from for the next steps, the LSF can already be used to simulate the signal produced S_{detector} by the detector when exposed to a certain object signal S_{object} by convoluting it with the LSF:

$$S_{\text{detector}} = LSF * S_{\text{object}}, \tag{4.5}$$

Obtaining the modulation transfer function from the LSF requires a discrete Fourier transform followed by a normalisation. However, the normalisation is prone to disturbance by noise, especially noise occurring in regions outside the central peak of the LSF. Since the information about the spatial resolution is located within the peak, the noise outside the peak can be suppressed using a filtering window. The filtering is achieved by multiplying the LSF with a Tukey window centred around the peak. The Tukey window

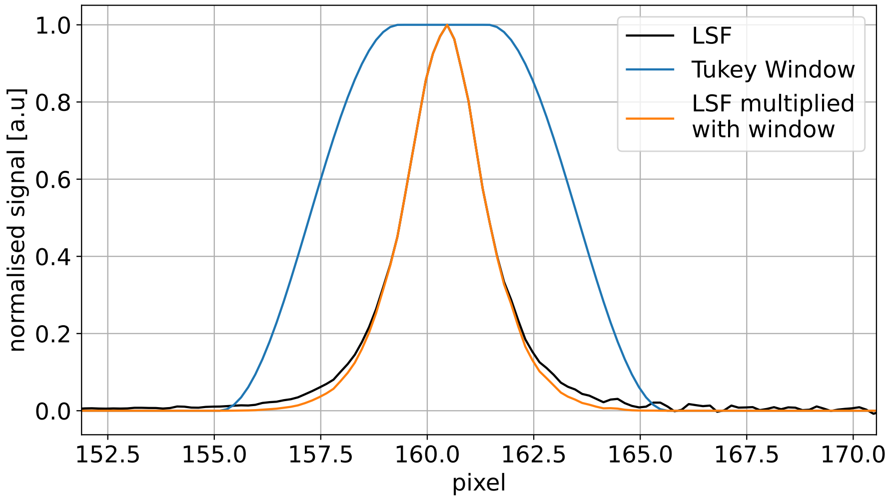

Figure 4.4.: Plot of line spread function (black), Tukey window (blue) and filtered line spread function (orange). The plot shows the signal in arbitrary units over the pixel position. Filtering is achieved by multiplying the Tukey window with the LSF. The curves are normalised to have a maximum value of one for better visibility.

is a box window convoluted with a cosine function defined as [Har78]

$$T(x) = \begin{cases} 1, & 0 \leq |x| < \alpha\frac{W}{2} \\ 0.5\left(1+\cos\left(\pi\frac{x-\alpha\frac{W}{2}}{2(1-\alpha)\frac{W}{2}}\right)\right), & a\frac{W}{2} \leq |x| \leq \frac{W}{2}. \end{cases} \tag{4.6}$$

Here, W is the window width and α is a parameter that defines the width of the flat top in the centre of the window. For $\alpha = 0$ the Tukey window is just a box window, for $\alpha = 1$ the top is round. An $\alpha = 0.8$ is chosen in this thesis, whereas W is chosen individually depending on the width of the LSF. With this choice, the central part of the peak is unaltered, but the quick drop-off on the flanks ensures effective noise suppression. The window, the original LSF and the filtered LSF are shown in Figure 4.4. As can be seen, a large part of the peak structure is practically unaltered by the window while the window pulls the LSF to zero around the base points, removing the noise visible on the right-hand side of the peak.

The next step is the application of a discrete Fourier transform to the filtered LSF and normalising with the zeroth frequency component to obtain the MTF. For sufficiently large ROIs, the normalisation can be conducted via the zero order frequency component [FC08]:

$$MTF(f) = \frac{|\mathfrak{F}\left[LSF(x)\right]|}{|\mathfrak{F}\left[LSF(x)\right](f=0)|} \tag{4.7}$$

$$|\mathfrak{F}\left[LSF(x)\right](f=0)| = \int_{-\infty}^{\infty} LSF(x)dx. \tag{4.8}$$

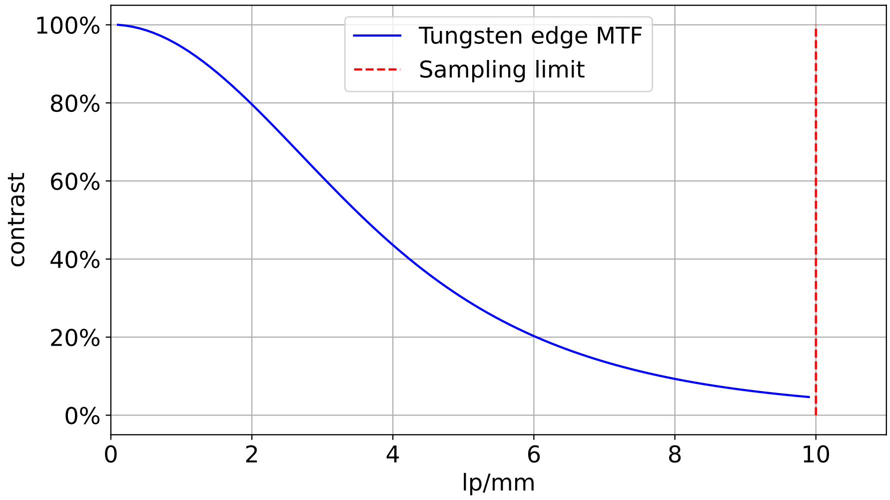

Figure 4.5.: Modulation transfer function (blue line) of the Dalsa Shad-o-Box as calculated using the slanted-edge method from the line spread function in Figure 4.4. Plotted is the retained contrast over spatial frequency in lp/mm. Also shown are the sampling limit due to the Nyquist-Shannon theorem (red dashed line).

The discrete derivative calculated earlier uses information from neighbouring bins, effectively acting as a weak low pass filter. As a result, higher frequencies are suppressed compared to lower frequencies [Bur00]. Therefore, a correction is applied to the MTF to counteract this attenuation [EM04]

$$MTF(f) = \frac{MTF_{\text{uncorrected}}(f)}{MTF_{\text{derivative}}(f)} \tag{4.9}$$

The correction factor can be calculated by [Bur00]

$$MTF_{\text{deriv}}(f) = \frac{\sin(\pi\delta k f)}{\pi\delta k f} \quad \delta = \frac{\text{pixel pitch}}{n}, \quad k = 2 \tag{4.10}$$

where delta is the sampling width and k is a constant depending on the derivative chosen. In case of the 3-point derivative used throughout this thesis, k is 2. n is the super sampling factor introduced earlier.

An example MTF is shown in Figure 4.5. Also shown in Figure 4.5 is the upper limit of resolution for a pixelated detector due to the Nyquist-Shannon [Sha49] sampling theorem. This theorem states, that to sufficiently sample a signal, the sampling frequency must be at least twice the signal frequency. The sampling frequency of a pixelated detector is given by its pixel pitch d_p, so the sampling limit can be calculated as:

$$f_{\text{limit}} = \frac{f_\text{p}}{2} = \frac{1}{2 \cdot d_\text{p}} \tag{4.11}$$

Information within an image with a frequency above the sampling limit can never be reliably resolved, but due to the super sampling performed on the ESF, the MTF

continues beyond this limit. For slanted-edge measurements along the diagonal of the pixel edges, an effective pixel pitch equal to $\sqrt{2}$ times the detector's pixel pitch is assumed. The slanted-edge method is verified with a second method for determining the spatial resolution. The process is described in section A.2.
When comparing the spatial resolution of two detectors, the detector with the MTF that retains higher contrast values at higher frequencies has the better resolution. It preserves more contrast, even when objects are closer together. This makes the MTF a suitable tool for comparing different detectors.

4.2. Noise characteristics

4.2.1. Fundamentals

Noise negatively impacts image quality of any imaging system. In measurements with digital semiconductor detectors three main sources of random noise contribute to the measured output: The photon noise σ_{photon}, the dark current noise $\sigma_{\text{darkcurrent}}$ and readout noise σ_{readout} ([Mul21], [Mul+94]). The noise contributions are uncorrelated, as the sources are independent physical processes. Hence, the total noise is the uncorrelated sum of the three contributors:

$$\sigma_{\text{tot}} = \sqrt{\sigma^2_{\text{photon}} + \sigma^2_{\text{darkcurrent}} + \sigma^2_{\text{readout}}} \tag{4.12}$$

The photon noise stems from the fact that the emission of photons is a statistical process. For a source with certain flux, the photon emission in a time interval Δt follows a Poisson distribution. The noise, meaning the standard deviation σ_{photon} of the mean number of photons N_{photon} is hence $\sqrt{N_{\text{photon}}}$. For a constant flux source, the photon number can be expressed in terms of integration time as $N_{\text{photon}}\Delta t$ and the measured photon noise becomes

$$\sigma_{\text{photon}} = \sqrt{Q_{\text{e}}\phi\Delta t}. \tag{4.13}$$

Here, ϕ is the average photon incidence rate in a pixel and Q_{e} the quantum efficiency of the detector. The quantum efficiency represents the statistical nature of the detection process and reduces the mean measured photon number.
Another type of noise present in digital semiconductor detectors is the dark current noise. As explained in section 2.3, free charge carriers are created via thermal excitation of electrons. This random process contributes to the detectors output in a manner indistinguishable from the true signal. The dark current follows a Poissonian distribution and hence the dark current noise can be expressed as:

$$\sigma_{\text{darkcurrent}} = \sqrt{D\Delta t} \tag{4.14}$$

Here, D is the average dark current rate and Δt the integration time. The dark current $D\Delta t$ adds a statistical but in average constant offset onto the detector output. The average offset can be corrected for by subtracting the offset pixel wise from the image. The statistical fluctuations $\sigma_{\text{darkcurrent}}$ remain in every pixel and contribute towards the total noise. Reducing the temperature of the semiconductor can greatly reduce the dark current and therefore the dark current noise [Iri+08].

Readout noise σ_{readout} adds an integration time independent noise component to the measurements and hence acts as a lower total noise floor [Mul+94].

The impact of noise on image quality also depends on the amplitude of the useful signal S. The signal-to-noise ratio [JT 11]

$$SNR = \frac{S}{\sigma_{\text{tot}}} = \frac{Q_{\text{e}}\phi\Delta t}{\sqrt{Q_{\text{e}}\phi\Delta t + D\Delta t + \sigma^2_{\text{readout}}}} \tag{4.15}$$

can be used to quantify the relation between both. It measures how well the signal stands out above the noise. The higher the SNR, the better the achievable image quality.

In cases where the photon flux and quantum efficiency is high enough ($Q_{\text{e}}\phi\Delta t \gg D\Delta t + \sigma^2_{\text{readout}}$), the detector is limited only by photon noise and the SNR can be approximated as

$$SNR \approx \frac{Q_{\text{e}}\phi\Delta t}{\sqrt{Q_{\text{e}}\phi\Delta t}} = \sqrt{Q_{\text{e}}\phi\Delta t} \tag{4.16}$$

Hence, the SNR follows a square root behaviour with diminishing returns for an increase in integration time. In this way, the quantum efficiency Q_{e} of a detector also influences the SNR. Instead of considering the total amount of photons N_{photon}, a detector with a quantum efficiency of lower than one measures a reduced number of photons $Q_{\text{e}}N$ and therefore has a lower SNR.

A sensor additionally contains fixed-pattern noise σ_{FPN}. This type of noise does not cause pixel value fluctuations from image to image but in an individual image fluctuations between pixels. Two types of fixed-pattern noise, the offset fixed-pattern noise and the photon response non-uniformity ([Iri+08] and [KW14]), are commonly distinguished. Offset fixed-pattern noise depends on the sensor temperature and integration time, as it is caused by a variation in dark current rate between pixels. The photon response non-uniformity depends on the incident photon rate. A source for this noise is for example a variation in amplification gain between the active pixels in a CMOS detector. Performing a gain and offset correction reduces the fixed-pattern noise. Hence, its contribution is not considered in Equation 4.15.

The pixel values are returned by the detectors in analogue to digital units (ADU), which is the output of the analogue to digital converters (ADC) used during readout. The ADU value of a pixel depends on the original signal, for example the collected charge in CCDs and the gain G, meaning the ratio between electron and ADU $\text{ADU} = G \cdot N_{\text{e}}$ [Mul+94]. The gain varies between detectors, hence ADU values of different detectors can not be compared directly. The gain also influences the dark current noise and photon noise. Measured in ADU, both noises can be calculated as [Mul+94]:

$$\sigma_{\text{darkcurrent, ADU}} = \sqrt{D_{\text{ADU}}\Delta t} = \sqrt{GD_{\text{e}}\Delta t}, \quad \sigma_{\text{photon, ADU}} = \sqrt{GQ_{\text{e}}\phi\Delta t}. \tag{4.17}$$

The SNR calculated from the ADU output and image quality subsequently also depends on the gain. To compare the image quality of different detectors, only the ADU values are considered in the following.

4.2.2. Data acquisition and analysis

In the following, a method capable of estimating the noise characteristics from a series of images taken at the liquid metal jet X-ray tube is introduced. However, results relying on measurements using an X-ray source depend on the spectrum of the source and can be used at different sources only with special considerations.

A series of images is taken at different integration times with illumination from the X-ray tube and without an object in the beam path. These images are in the following referred to as flat frames. The flat frames contain the detectors response to a number of X-ray photons, depending on the distance of the detector from the source and the integration time. If the photon flux from the source is sufficiently constant over the measurement, photon number and integration time are proportional. Results presented in section 4.3 indicate, that the liquid metal jet X-ray tube fulfils this condition. The same time series is then taken without the illumination by the X-ray tube. These dark frames contain only the readout and dark current noise, whereas the flat frames contain contributions from all three noise components as well as the signal. By combining data from both series, all required information for noise characterisation can be retrieved.

A statistical analysis is then performed on the pixel values within a small ROI. The ROI is necessary due to possible non-uniform illumination from the cone beam of the X-ray source, adding a variation between pixel values depending on the X-ray source, rather than on the detector. By choosing a ROI, that ideally contains no gradient, the impact of the non-uniform illumination on the results can be reduced. To make measurements comparable between detectors, the ROI should be chosen at a similar location within the X-ray beam.

Within the ROI the ensemble mean $\mu_{\text{flat/dark}}$ is determined for the dark frames and flat frames using the estimator function

$$\mu_{\text{flat/dark}} = \frac{1}{N_{\text{R},k}} \sum_{i=1}^{N_{\text{R},\,k}} x_i \tag{4.18}$$

Here, $N_{\text{R},\,k}$ is the total number of pixels in the ROI considering all images with the same integration time and x_i are the individual pixel values. The flat frame mean μ_{flat} contains the signal S, the dark current, and a constant offset that is added by the readout electronics. μ_{dark}, the dark frame mean, contains only the constant offset and dark current. By subtracting the two, the useful signal is retrieved:

$$S = \mu_{\text{flat}} - \mu_{\text{dark}}. \tag{4.19}$$

The estimation of the noise is conducted by calculating the root-mean-square (RMS) value of the difference of image pairs taken at the same integration time [Mul+94]:

$$\sigma_{\text{flat/dark}} = \sqrt{\sum_{i=1}^{N_{\text{R, diff}}} \frac{(A_i - B_i)^2}{2 \cdot (N_{\text{R, diff}} - 1)}} \tag{4.20}$$

Here, A_i and B_i are the individual pixel values in the first and second image respectively. $N_{\mathrm{R,\,diff}}$ is the number of pixels within the ROI of the difference image. The calculation uses the fact, that the fixed pattern noise does not vary between exposures, but between pixels. By subtracting two images taken with the same integration time, the fixed pattern noise is therefore cancelled out. The difference image now contains only the uncorrelated sum of both individual images

$$\sigma_{\mathrm{diff}} = \sqrt{\sigma_A^2 + \sigma_B^2} = \sqrt{2}\sigma_{A/B} \tag{4.21}$$

as noise. So, to retrieve the RMS of an individual image, the RMS value is corrected by the division with $\sqrt{2}$ in Equation 4.20. The mean of the difference image is 0, since the mean in both individual images is equal. Hence, the RMS value is equal to the standard deviation.
With signal and noise known, the SNR can be calculated from both estimates as

$$SNR = \frac{\mu_{\mathrm{flat}} - \mu_{\mathrm{dark}}}{\sigma_{\mathrm{flat}}}. \tag{4.22}$$

The statistical ensembles can also be used to estimate the uncertainties on S, σ and SNR, in the following denoted with Δ. For S, the uncertainty can be obtained via Gaussian error propagation from the uncertainty estimations on the individual μ:

$$\Delta\mu = \sqrt{\frac{1}{N}\sum_{i=1}^{N}\frac{(x_i-\mu)^2}{N-1}}, \quad \Delta S = \sqrt{\Delta\mu_{\mathrm{dark}}^2 + \Delta\mu_{\mathrm{flat}}^2}. \tag{4.23}$$

The sum is performed over all N_{R}, k pixels contained in the ROIs of all images at a given integration time. The statistical uncertainty on $\sigma_{\mathrm{flat/dark}}$ is estimated as an uncertainty of the RMS within the ROI of the difference images [Met20]:

$$\Delta\sigma_{\mathrm{f}} = \sqrt[4]{\frac{2\left(\sum_{i=1}^{N_{\mathrm{R,\,diff}}}(A_i-B_i)^2/(N_{\mathrm{R,\,diff}}-1)\right)^2}{N_{\mathrm{R,\,diff}}-1}}, \quad f \in (\text{flat, dark}). \tag{4.24}$$

As before, $N_{\mathrm{R,\,diff}}$ is the number of pixels in the ROI of a difference image and A_i, B_i are the pixel values of the original flat and dark frames. If more than one pair of images is taken at an integration time, the uncertainty is used to calculate the weighted average of $\sigma_{\mathrm{flat/dark}}$. The individual $\Delta\sigma_i$ errors are added accordingly through the inverse sum

$$\Delta\sigma_f = \frac{1}{\sqrt{\sum_i \Delta\sigma_i^{-2}}} \quad f \in (\text{flat, dark}). \tag{4.25}$$

Using Gaussian error propagation, an estimation on the uncertainty of SNR is obtained from the individual contributions:

$$\Delta SNR = \sqrt{\left(\frac{\Delta S}{\sigma_{\mathrm{flat}}}\right)^2 + \left(\frac{S}{\sigma_{\mathrm{flat}}^2}\Delta\sigma_{\mathrm{flat}}\right)^2} \tag{4.26}$$

However, due to the large sample sizes, the uncertainties for most measurements are small, in the order of magnitude of one percent of their corresponding values. Hence, uncertainties are shown in the plots in section 4.3 only if they are significant, which is the case for dark frame noise estimates. Nevertheless, all uncertainties are considered for the following fits.

The data obtained from the dark frame series is further used to examine the dark and readout noise characteristics. By calculating σ_{dark} following Equation 4.20, the readout and dark current noise can be examined. Furthermore, μ_{dark} is used to characterise the dark current. A linear function

$$I_{\text{fit}}(t) = a \cdot t + b \tag{4.27}$$

is fitted to μ_{dark} over the integration time. From the fit parameters, the dark current rate in ADU/s and a mean offset in ADU can be determined.
Similarly, the flat frame series additionally allows for investigating the linearity of the detector response. The linearity measures whether an increase in photon numbers causes an equal increase in signal. For detectors with non-linear responses, additional corrections are required. The linear function of Equation 4.27 is fitted to the signal over integration time using the uncertainty from Equation 4.23 as fitting weights. From the fit parameters, the fit residuals

$$\Delta I(t) = I_{\text{data}}(t) - I_{\text{fit}}(t) \tag{4.28}$$

are calculated. The relative fit residuals R are then used as a measure for relative deviation from linearity of the detector response:

$$R = \frac{\Delta I(t)}{I_{\text{data}}(t)} \tag{4.29}$$

Fit uncertainties and the uncertainties on the original data points are used to estimate uncertainties on R. The lower the relative deviation from linearity is the more linear the detector's response.

4.3. Individual detector characterisation

In the following six detectors are characterised. Unless otherwise stated, all corrections like automatic gain or offset correction are disabled and no other adjustments to the settings are performed. Each detector is first examined in regard to its noise characteristics, then for its spatial resolution, before special remarks and optimum measurement parameters are given. Characterisation measurements are performed for only one specific setup per detector, but the optimal measurement parameters obtained can still be used to optimise differing setups. For example, if the distance between source and detector is halved, a good starting point for integration times is a quarter of the times provided.

4.3.1. Dalsa Shad-o-Box

The Dalsa Shad-o-Box 6K is a flat panel CMOS detector with direct deposition GadOx scintillator and a pixel size of 49.5 µm [Ima20]. It has a resolution of 2304 by 2940 pixels and a field of view of 11.4 cm by 14.6 cm.

Measurements for the characterisation of the Dalsa Shad-o-Box are taken at the liquid metal jet X-ray tube with an acceleration voltage of 30 kV. The distance between the source and the detector is 150 ± 2 cm, the total output power is set to 20.0 W and a spot size of 20 µm is chosen.

Noise characteristics: Images with integration times from 1 s to 30 s are taken with a time step of 1 s between each measurement. For each integration time, ten images are taken. The same amount of images is taken for the Dark frame series without illumination by the X-ray tube. Figure 4.6a shows the results of the noise characterisation in a 50 by 50 pixel area in the centre of the detector. Shown are the expected signal according to Equation 4.18, the estimated noise σ_{flat} in the ROI and the signal-to-noise ratio. The Dalsa Shad-o-Box uses 14 bit analogue to digital converters, the maximum measurable signal lies hence at $2^{14} = 16384$ ADU. None of the integration times create a high enough signal to reach this saturation signal, as the maximum measured signal is around $12,000$ ADU. The measured noise σ_{flat} rises with integration time to a value of about 70 ADU at 30 s. Hence, the measured SNR reaches values slightly above 175. The SNR curve of the Shad-o-Box in Figure 4.6a has its steepest incline for integration times up to about 10 s. At higher integration times, the SNR increases more slowly, due to the square root behaviour of the SNR on photon number.

Figure 4.6b provides insight into the dark noise. As can be seen, a σ_{Dark} increases from about 4 ADU at 1 s to about 6 ADU at 30 s, probably due to dark current noise. The low standard deviation means, that only a small amount of noise measured in the flat frames stems from dark current or readout noise. The detectors' performance is hence limited by photon noise. Large differences between estimated standard deviations can be found around the integration times 6 s, 14 s and 27 s. These fluctuations are also seen in the flat noise. A possible source could be an automatic switching of some of the detector's parameters with changing integration time.

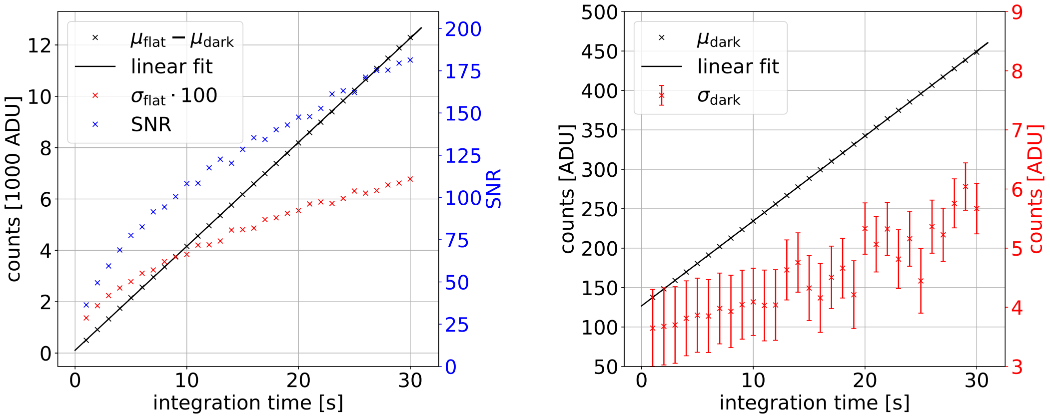

(a) Flat frame noise characteristics of the Dalsa Shad-o-Box detector. The units are counts in ADU over integration time in seconds. Black data points represent the mean signal, red data points the noise. The solid black line represents a linear fit. The blue data points use the right y-axis and show the SNR.

(b) Dark frame noise characteristics of the Dalsa Shad-o-Box detector. Black data points represent the mean pixel values in ADU. Red data points show use the right y-axis and show the measured pixel value standard deviation in ADU. Both are plotted over the integration time in seconds. The solid black line represents a linear fit to the mean pixel values.

Figure 4.6.

From the linear fit in Figure 4.6b, a dark current of

$$D(t) = (10.452 \pm 0.015)\,\frac{\text{ADU}}{\text{s}} \cdot t + (130.49 \pm 0.10)\,\text{ADU} \tag{4.30}$$

is obtained. The 10.45 ± 0.05 ADU/s are slightly better than the value of 12 ADU/s given by the manufacturer (see [Ima20]), possibly due to a lower ambient temperature during measurement.

From the linear fit in Figure 4.6a, the linearity of the Dalsa Shad-o-Box is examined. The result is shown in Figure 4.7. Over the entire measured integration times, the relative deviation is smaller than 3.5%, if only values for integration times larger than seven seconds are considered, the relative deviation is smaller than 1%. The larger deviation at shorter integration times is also seen for the other detectors. It therefore probably stems from the method rather than from the detector. The small deviation from linearity also indicates that the X-ray flux from the liquid metal jet tube varies little over the measurement times examined.

Spatial resolution: Slanted-edge measurements are performed for the Dalsa Shad-o-Box detector both parallel to the detector's edges as well as tilted 45°. These measurements are performed under the same conditions as the noise measurement at an integration time of 10 s. The tungsten edge is placed directly in front of the detector.

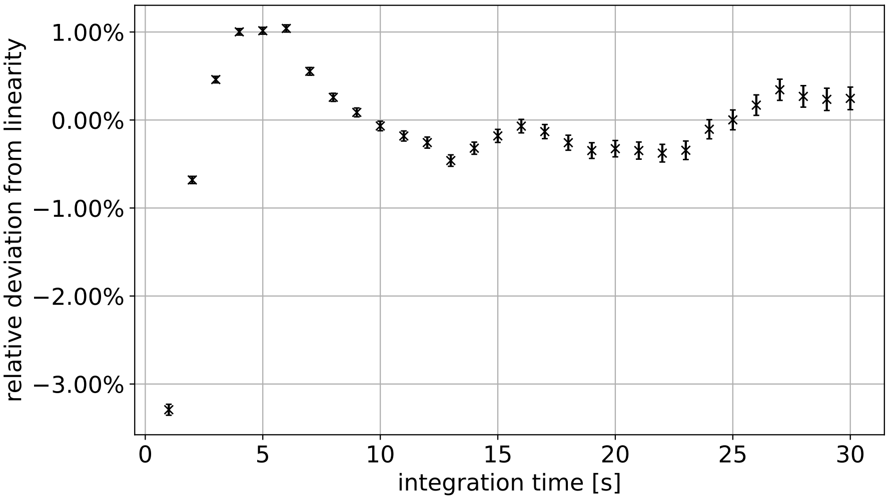

Figure 4.7.: Relative deviation from ideal linear behaviour of the Dalsa Shad-o-Box detector over integration time in seconds.

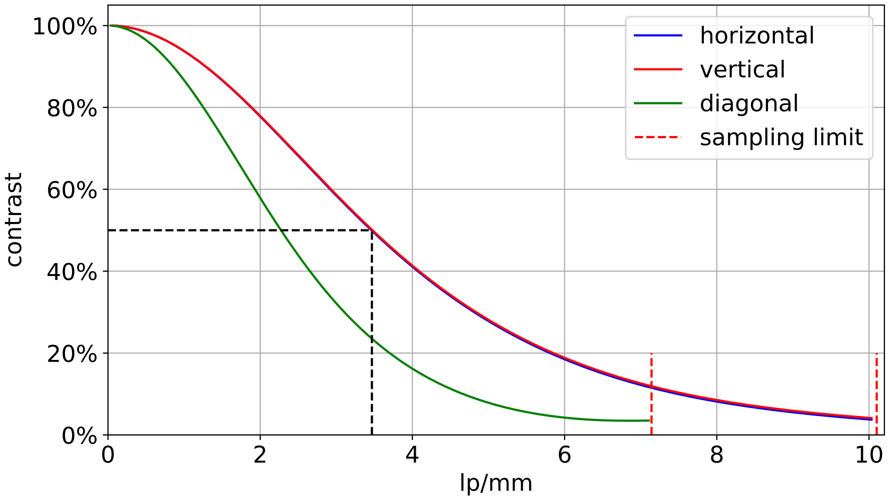

Figure 4.8.: Spatial resolution of the Dalsa Shad-o-Box detector. Shown are the $MTFs$ in horizontal, vertical and diagonal directions relative to the pixel edges. They indicate the retained contrast depending on the spatial frequencies in lp/mm. The dashed red line represents the sampling limits due to the pixel pitch. The effective diagonal pixel pitch is calculated as $\sqrt{2}$ times the pixel pitch, assuming a square pixel shape. The dashed black lines indicate the location at which the contrast decreases to 50% for the two main detector axes.

The results are plotted in Figure 4.8. The MTF for both major axes are practically identical, whereas the MTF measured diagonally to the pixel edges falls off more quickly. The two major axes $MTFs$ reach low contrast values long before the sampling limit of 10 lp/mm imposed by the pixel pitch. They drop to 50% contrast at around 3.8 lp/mm, even before half the sampling limit. This result indicates that the limiting factor of the spatial resolution is not the CMOS sensor, but the scintillator spreading the signal over multiple pixels.

In conclusion, under the conditions given in this chapter, the Dalsa Shad-o-Box is best used with integration times between ten and twenty seconds. At higher integration times, the increase in SNR diminishes. The Dalsa Shad-o-Box achieves impressive signal-to-noise ratios with excellent linearity over the entire dynamic range. Under no circumstances should the integration time exceed two minutes, since the dark current will use ten percent of available dynamic range at this integration time. The spatial resolution is equal in horizontal and vertical direction and slightly worse when measuring along the pixel grid diagonal. Structures or objects should be no smaller than 130 µm in the detector plain, as smaller objects will be imaged with less than 50% of their original contrast.

4.3.2. Dalsa Xineos

The Dalsa Xineos is a flat panel CMOS detector with an active area of 14.73 cm by 11.37 cm and a resolution of 1488 by 1148 pixels. The pixel pitch is 99 µm. Its X-ray sensitivity is achieved via a direct deposition microstructured CsI scintillator [Dal].
The characterisation measurements are performed at the liquid metal jet X-ray tube at 30 kV acceleration voltage, 20 W output power and 20 µm. The Xineos flat panel detector is placed at a distance of 150 ± 2 cm from the source.

Noise characteristics: The detector's performance is examined for integration times between 1 s and 60 s. Up until 30 s measurements are taken with a 1 s separation, at higher integration times the separation is 5 s. Each integration time is sampled with ten individual images. A 50 by 50 pixel area is chosen in the centre of the detector for analysis. Figure 4.9a shows the results of the flat frame analysis. The mean signal $\mu_{\text{flat}} - \mu_{\text{dark}}$, shown in black, rises linearly until an integration time of 20 s is reached. Here, the mean signal saturates.
The saturation also influences the measured standard deviation. If the incident radiation intensity is high enough to cause a pixel to saturate, noise can not further increase the measured intensity, only allowing fluctuations towards lower intensities. This cuts the pixel value distribution at its maximum and reduces its width. As soon as an increasing number of pixels reach this state, the standard deviation of the ensemble decreases.
Before the saturation is reached, the standard deviation σ_{flat} shows similar behaviour to the Shad-o-Box, by increasing to about 80 ADU. The signal reaches ADU values higher than the Dalsa Shad-o-Box for the same exposure times. Considering that both detectors use 14 bit ADCs, and the slightly worse flat frame noise of the Xineos detector,

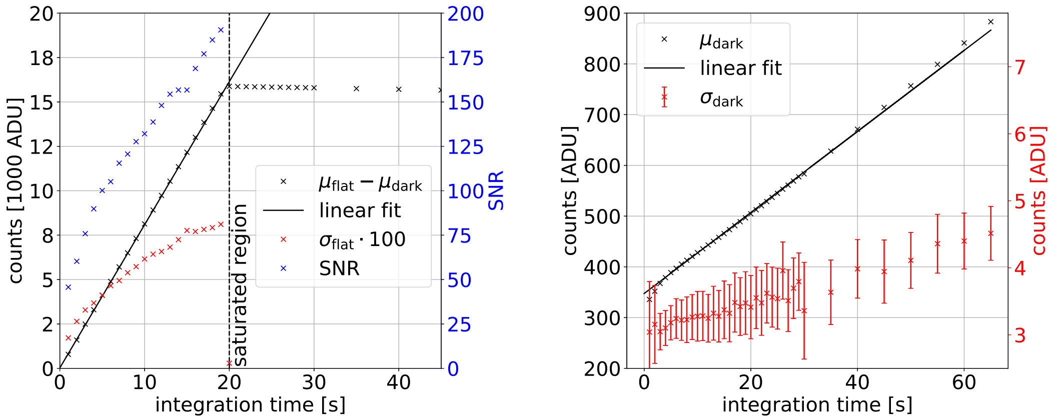

(a) Flat frame noise characteristics of the Dalsa Xineos detector. The units are counts in ADU over integration time in seconds. Black data points represent the mean signal, red data points the noise. The solid black line represents a linear fit. The blue data points use the right y-axis and show the SNR. Points lying right of the dashed black line are saturated.

(b) Dark frame noise characteristics of the Dalsa Xineos detector. Black data points represent the mean pixel values in ADU. Red data points show use the right y-axis and show the measured pixel value standard deviation in ADU. Both are plotted over the integration time in seconds. The solid black line represents a linear fit to the mean pixel values.

Figure 4.9.

a similar maximum signal-to-noise ratio is achieved. However, the pixel pitch of the Xineos detector is twice that of the Shad-o-Box, meaning that due to the same distance between source and detector during measurements, each pixel in the Xineos detector received four times the amount of photons a pixel of the Shad-o-Box received. The Xineos detector uses the available photons less efficient than the Shad-o-Box, possibly due to its lower quantum efficiency at lower energies [Dal].

Figure 4.9b shows the dark frame noise behaviour. The Dark noise increases from about 3 ADU to 5 ADU in the 60 s integration time range. Figure 4.9b also contains a linear fit to the measured dark current to characterise it. The fit parameters obtained are

$$D(t) = (8.26 \pm 0.05)\,\frac{\mathrm{ADU}}{\mathrm{s}} \cdot t + (351.8 \pm 1.2)\,\mathrm{ADU} \tag{4.31}$$

The first three average pixel values deviate from the expected linear behaviour by showing lower values, toward higher integration times, the measured *ADU* increase slightly more than expected. A possible reason for these deviations could be an increase in detector temperature, due to heat dissipation from the detector's electronics.

A fit is also performed to the non-saturated mean signal in Figure 4.9a in order to characterise the linearity of the detector response. The relative fit residuals of this fit are plotted in Figure 4.10. For integration times longer than two seconds, a maximum deviation from linearity of smaller than 2% can be seen. The first two measurement points show once again a stronger deviation, that probably stems from the method. At

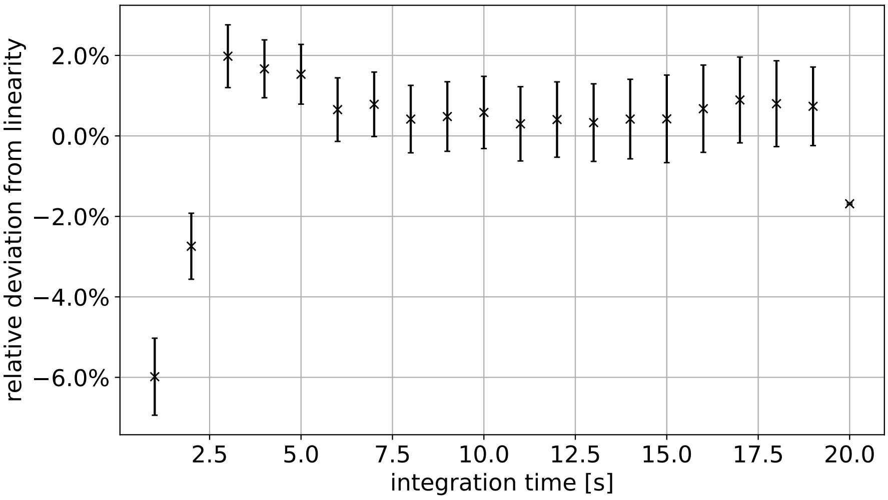

Figure 4.10.: Relative deviation from ideal linear behaviour of the Dalsa Xineos detector over integration time in seconds.

20 s, the detector's response deviation changes by more than 2%, which is a consequence of the beginning saturation.

Spatial resolution: The slanted-edge method is used to examine the spatial resolution of the Xineos flat panel detector in both major directions parallel to the pixel edges and once diagonally. The tungsten edge is placed directly in front of the detector and an integration time of 10 s is chosen. Figure 4.11 shows the result. As can be seen, the resolution in both major directions is once again practically equal, whereas the diagonal resolution is inferior. Due to the 99 µm pixel size, the spatial resolution of the Xineos is limited to a maximum of 5 lp/mm. However, the contrast decreases to 50% already at about 2 lp/mm, meaning that the scintillator is the limiting factor for spatial resolution.

The Dalsa Xineos detectors overall performance is slightly worse than its most comparable counterpart, the Dalsa Shad-o-Box. A lower spatial resolution mean that the Xineos detector is best suited for applications where spatial resolution is not critical. Similar signal-to-noise ratios are achieved after shorter integration times. Hence, in some applications the total measurement time could be reduced with the Xineos detector. If the detector is used, care must be taken that the saturation region is not reached. For the measurement parameters given in this section, an integration time of about 10 s is optimal, as about 60% of the saturation level is reached at this integration time. The minimum structure size resolvable is about 250 µm in the detector plain.

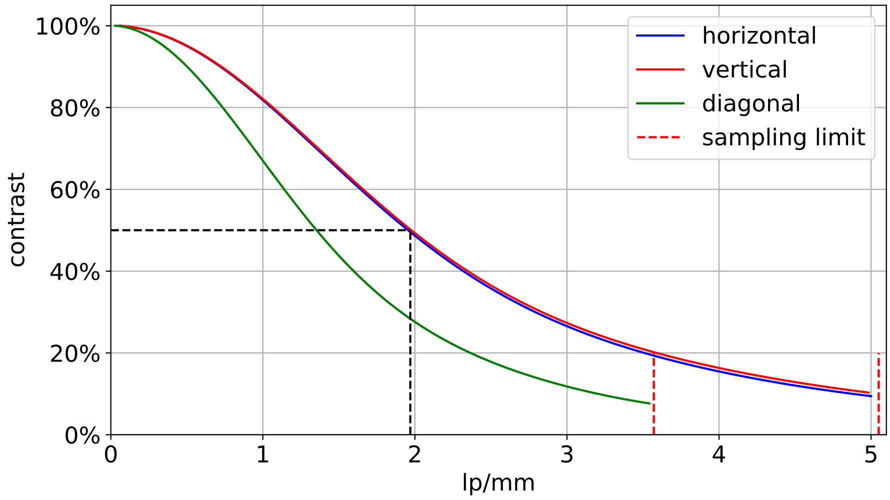

Figure 4.11.: Spatial resolution of the Dalsa Xineos detector. Shown are the $MTFs$ in horizontal, vertical and diagonal directions relative to the pixel edges. They indicate the retained contrast depending on the spatial frequencies in lp/mm. The dashed red line represents the sampling limits due to the pixel pitch. The effective diagonal pixel pitch is calculated as $\sqrt{2}$ times the pixel pitch, assuming a square pixel shape. The dashed black lines indicate the location at which the contrast decreases to 50% for the two main detector axes.

4.3.3. Rigaku XSight Micron LC

The Rigaku XSight Micron LC camera is a detector system consisting of a main unit with a thermoelectrically cooled CCD sensor and a lens unit that also contains the scintillator. The CCD has a resolution of 3300 by 2500 and an electronic shutter in the form of interline registers. Different lens units with different fields of view and effective pixel size are available. In the following, a lens unit with an effective pixel size of 0.27 µm and a field of view of 0.9 mm by 0.68 mm [Cor22] is tested. The small pixel size combined with the lens coupling of the scintillator to the CCD array means that a low number of photons is expected to reach the CCD array. The measurements are hence performed with a shorter distance of 45 ± 2 cm between source and detector to increase the amount of photons at the scintillator. The LMJ is set identically to the previous measurements to 30kV and 20W. During measurements, the CCD sensor is cooled to $-25\,°\mathrm{C}$ to obtain the best possible results.

Noise characteristics: Integration times are set between 1 s and 30 min. The amount of images taken at each time step depends on the individual integration time. For small integration times, 10 individual images are taken, while at 30 min only three images are taken. The same amount of images is taken without illumination by the X-ray tube. One additional image is taken at 1 h and 2 h each, only the mean according to Equation 4.18 is calculated for these data points, since estimation of noise requires two images. Although

the entry window of the detector is very small and the X-ray intensity can be assumed to be constant over the entire window, a ROI of 50 by 50 pixels is chosen for the analysis. Figure 4.12 shows the result of the flat frame analysis. The signal $\mu_{\text{flat}} - \mu_{\text{dark}}$ in Figure 4.12a increases linearly over the entire measured range reaching values of up to 10000 ADU and showing no signs of saturation. The SNR increases with increasing integration times up to about a value of 50 at 30 min integration time.
The dark frame results are shown in Figure 4.12b. The mean pixel values increase by only 20 ADU over the two-hour integration time range, the strongest increase is seen for the first four integration times 1 s, 10 s and 30 s, possibly due to the detector not being in thermal equilibrium. A fit is performed to μ_{dark}, excluding the first five data points in order to obtain an estimation of the dark current in integration time ranges, where measurements are sensible.

$$D(t) = (1.7 \pm 0.7) \cdot 10^{-3} \, \frac{\text{ADU}}{\text{s}} \cdot t + (1036.1 \pm 0.7)\,\text{ADU}. \tag{4.32}$$

These fit parameters show, that the CCD cooled down to −25 °C has very little dark current and therefore only a small dark current noise contribution to the total noise can be expected. This is corroborated by the fact, that the measured standard deviation in the examined range does not change within the measurement accuracy. The 14 ADU standard deviation is therefore mostly readout noise.
The fit in Figure 4.12a is used to analyse the linearity of the detector's response. The results are shown in Figure 4.13. The deviation from the linear behaviour stays below 1.5%, meaning the relative deviation from ideal linear behaviour is minimal for the Rigaku XSight LC camera.

Spatial resolution: For the Rigaku XSight micron LC camera, slanted-edge measurements are performed only in the horizontal direction, as the small field of view makes it almost impossible to align the tungsten edge. The result is shown in Figure 4.14. Although the measured resolution is very impressive with 50% contrast at 95 lp/mm, it is far from the sampling limit of 1852 lp/mm. The reason for this is probably the edge itself. While for detectors with pixel sizes of tens of micrometers an almost perfect edge structure is reasonable to assume, for a pixel size of 270 nm this is not the case. Since the camera is able to resolve a 6 µm grating structure, as explained in the following, the result of the slanted-edge method is just a lower limit on the resolution.

Sample image: To show the potential applications of the Rigaku XSight micron LC, a sample image is shown in Figure 4.15 containing a section of the 8077 grating (see Table A.1). This is a G_2 grating with a period of 6 µm. The transmission image reveals useful information about the structure of the grating. It shows that the grating bars are not one single long absorber but divided by resist bridges. In the right half of Figure 4.15 a grating defect, where two of the grating bar lamellae are missing, can be seen. The resolution of the camera is sufficient to measure the period of the grating period. This makes the detector useful in combination with the AXT method presented in chapter 3,

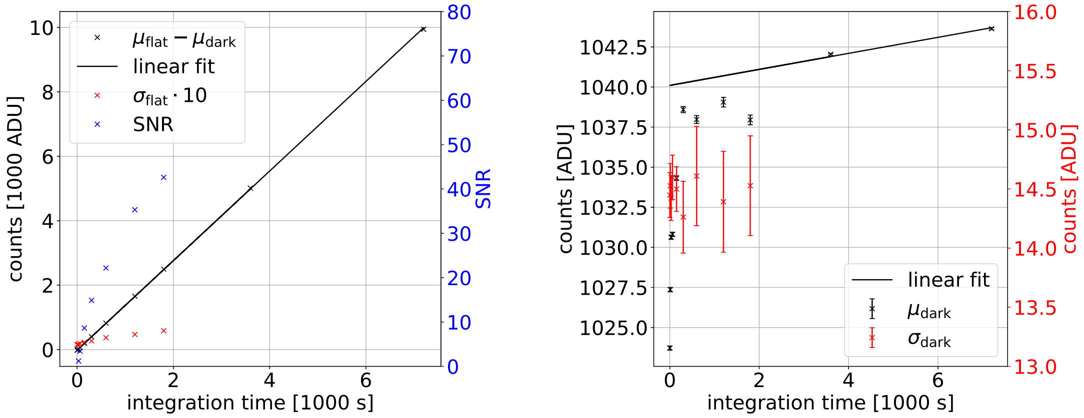

(a) Flat frame noise characteristics of the Rigaku XSight Micron LC detector. The units are counts in ADU over integration time in seconds. Black data points represent the mean signal, red data points the noise. The solid black line represents a linear fit. The blue data points use the right y-axis and show the SNR. Noise estimates are only performed up to 30 min integration time.

(b) Dark frame noise characteristics of the Rigaku XSight Micron LC detector. Black data points represent the mean pixel values in ADU. Red data points show use the right y-axis and show the measured pixel value standard deviation in ADU. Both are plotted over the integration time in seconds. The solid black line represents a linear fit to the mean pixel values. Noise estimates are only performed up to 30 min integration time.

Figure 4.12.

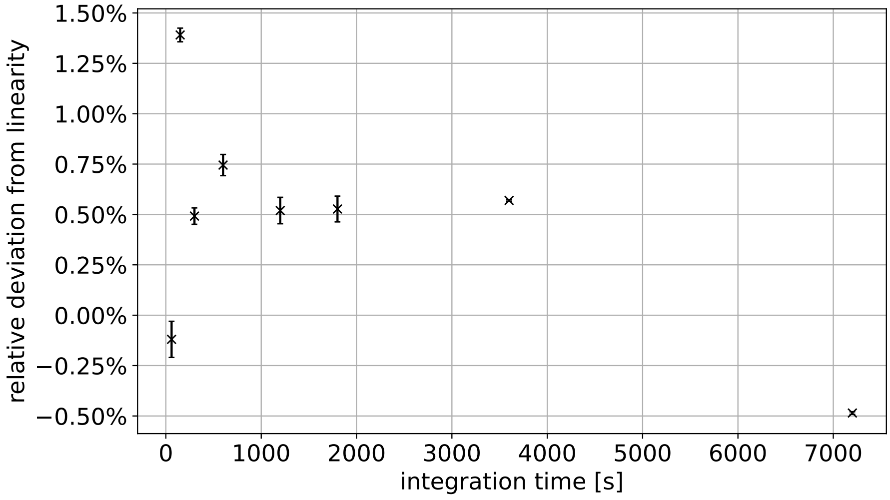

Figure 4.13.: Relative deviation from ideal linear behaviour of the Rigaku XSight Micron LC detector over integration time in seconds.

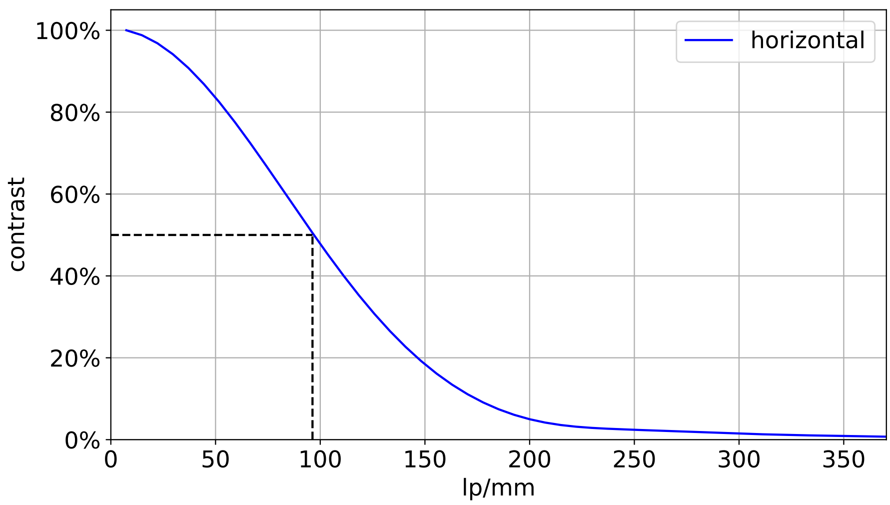

Figure 4.14.: *MTF* of the Rigaku XSight Micron LC detector measured using the tungsten edge. Shown is the *MTF* in horizontal direction. It indicates the retained contrast depending on the spatial frequencies in lp/mm.

where the grating period can not be measured but is required for the determination of the other grating parameters.
The image shows a spatial resolution of the Rigaku XSight micron LC camera that is unmatched by any standard X-ray detector for medical or industrial imaging. This resolution comes at the price of integration time and noise levels in the obtained images. A very high stability against movement of the object and the source spot is required within the setup to allow for the high integration times necessary to achieve acceptable noise levels. The image in Figure 4.15 is exposed for over 15 min, yet still contains clearly visible noise.

The Rigaku XSight micron LC camera is defined by its superior spatial resolution. This allows for X-ray microscopy without the need for magnification within the setup. The distance between the source and the entry window of the camera should be chosen as small as possible to achieve sufficient statistics within reasonable integration times. The optimal integration time at the LMJ with the given X-ray tube settings is between 10 min and 20 min. Longer integration times lead to a smearing in the images due to the focus movement of the tube. The detector can be used to achieve X-ray microscopy with effectively parallel beam geometry, allowing for example the examination of grating structures. In this way, the Rigaku XSight micron LC camera is useful in obtaining information about gratings that is not accessible with AXT measurements, like the grating period and the structure of grating bars.

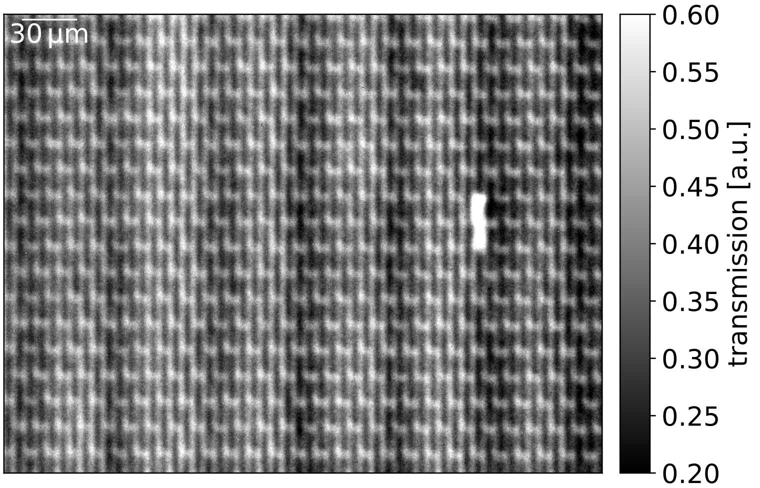

Figure 4.15.: Sample images taken with the Rigaku XSight micron LC. The image shows the transmission through a section of the 8077 absorption grating with a period of 6 µm. Integration time is 15 min. The image is taken with a detector to source distance of 45 cm and an X-ray tube power of 20 W. The distance between the sample and the entry window is smaller than 5 mm.

4.3.4. Imaging plates

Fuji-BAS SR imaging plates are an analogue imaging solution. Imaging plate characterisation measurements are performed with 30 kV acceleration voltage, 20 W and 20 µm spot size at a source to detector distance of 100 ± 2 cm. The scanning process is performed for the slanted-edge resolution measurements at a Fuji FLA 7000. This scanner is located at GSI centre in Darmstadt, hence a delay between exposure and scanning of several hours is unavoidable. The high number of exposures required for the noise characterisation measurements made using the same scanner unfeasible, and the long transport time would influence the results. Instead, the available Dürr Medical CR35 BIO scanner is used.

Noise characteristics: Both scanners allow for a selection of multiple step sizes, varying the effective pixel size from 25 µm to well above 100 µm. The scan width determines the area of the image plate that is considered for each individual pixel. This yields a situation similar to a pixelated detector with variable pixel pitch. The scan widths 25 µm and 50 µm are examined in the following at integration times between 1 s and 90 s. Since each integration time requires an empty imaging plate, only one image is taken at each step. This means, that Equation 4.20 can not be used to estimate the noise in the flat frames, as at least two images per integration time are required. Instead, the flat frame noise is estimated from the ROI using the estimator for the standard deviation

$$\sigma_{\text{flat}} = \sqrt{\sum_{i=1}^{N_{\text{pixel}}} \frac{(x_i - \mu_{\text{flat}})^2}{N_{\text{pixel}} - 1}} \tag{4.33}$$

over the N_{pixel} pixel values x_i of the ROI. Uncertainties on σ_{flat} can be estimated using [Met20]

$$\Delta\sigma_{\text{flat}} = \sqrt[4]{\frac{2\left(\sum_{i=1}^{N_{\text{pixel}}} (x_i - \mu_{\text{flat}})^2 / (N_{\text{pixel}} - 1)\right)^2}{N_{\text{pixel}} - 1}}. \tag{4.34}$$

The analogue nature of the imaging plates also means, that no dark current noise is produced in imaging plates themselves and readout noise stems from the scanning process. Furthermore, two types of photon noise are involved, one at the formation of the image from X-ray photons and one at the readout of the PSL photons. As another consequence, the integration time of the imaging plates can not be set in the detector but has to be varied with a shutter. In this case the shutter of the liquid metal jet X-ray tube is used. The manual opening and closing of the shutter causes an uncertainty within the actual integration time estimated to be ±1s, that is especially significant for short integration times. For the two lowest integration times, the actual time the shutter is opened is determined by placing the Dalsa Shad-o-Box detector behind the imaging plates and setting its integration time to 100 ms. The images around the exposure of the imaging plates are saved, and by counting the images in which the Shad-o-Box measured incident radiation. The true integration time can be determined with a precision of ±141 ms, stemming from an uncertainty of 100 ms on the start and stop image each. The uncertainties on the mean counts and standard deviations are smaller than 1% of their corresponding values and are hence not shown.

Figure 4.16 shows the results of the noise characterisation of the imaging plates for 25 µm and 50 µm scan width. Both datasets show qualitatively the same behaviour as the other detectors. The mean signal $\mu_{\text{flat}} - \mu_{\text{dark}}$ rises linearly until a saturation is reached beyond 40 s integration time. After this point, the increase of noise σ_{flat} turns into a decrease for the reasons explained in subsection 4.3.2. The signal-to-noise ratio for the 50 µm scan width reaches a maximum value of about 75. Compared to the 25 µm bandwidth, the SNR is consistently better over the entire sampled dynamic range, by a factor of 1.47 ± 0.07.

The high uncertainty in integration time entails a high uncertainty in the total number of photons, the imaging plates are exposed to at each time step. This uncertainty makes a fit to examine the linearity of the response unfeasible and no fit to the mean signal is attempted.

Spatial resolution Although imaging plates are analogue detectors with no pixels, the slanted-edge method described in section 4.1 can still be used for characterisation due to the fact, that the scanning required for image retrieval is done in discrete steps. These steps are then treated as if they were pixels from beginning. The characterisation

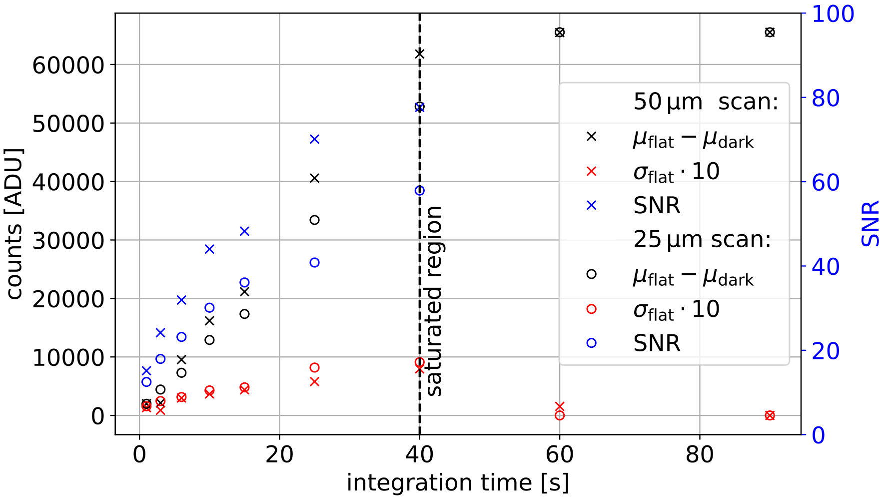

Figure 4.16.: Noise characteristics of the Fuji-Bas SR imaging plates. Shown are results for a scanning width of 25 µm and 50 µm denoted with cross- and circular markers respectively. Black and red markers represent mean signal and noise in ADU. The blue markers indicate the SNR and use the right y-axis. The x-axis indicates the integration time in seconds. The dashed black line shows the integration time after which the imaging plates reach saturation.

therefore also includes the influence of the scanner. Additionally, imaging plates also have an intrinsic signal spread limiting their resolution. [Fik+12].
The slanted-edge method is used to characterise the resolution of the imaging plates with a scan width of 25 µm and 50 µm. The scan process partially erases the information on the imaging plate, so each scan configuration requires separate exposure and scan. The results are shown in Figure 4.17. Both $MTFs$ are very similar, only diverging for higher spatial frequencies. The smaller scan width has its 50% contrast point at below half the sampling limit, while it lies far beyond half of the sampling limit for the larger scan width. The two different scan widths reach the 50% contrast point with only a difference of about 0.3 lp/mm, far less than to be expected from a halving of the pixel pitch. This indicates, that the limiting factor spatial resolution of this type of imaging plates with the given scan widths is the intrinsic signal spread and not the scan width.

The Fuji-BAS SR imaging plates offer a good compromise between noise characteristics and spatial resolution. However, they are limited in their usefulness by their analogue nature. The extra readout and the lack of electronically controlled shutter make them impractical in scenarios where many images have to be taken, where stability in detector position is required or where spatial information of many images needs to be compared. These factors also make them difficult to use in vacuum environments. The worse SNR when using 25 µm scanning width compared to 50 µm scan width is barely offset by the minimal gain in spatial resolution. The trade-off should hence only be taken if absolutely necessary and expected photon numbers permit it.

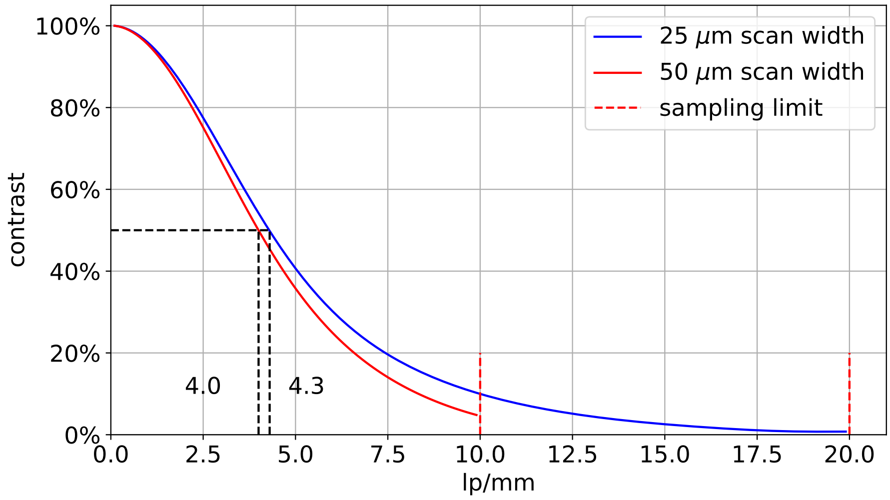

Figure 4.17.: Spatial resolution of the imaging plates scanned with two different scan widths. Shown are the *MTFs* for 25 µm and 50 µm scan width. They indicate the retained contrast depending on the spatial frequencies in lp/mm. The dashed red line represents the sampling limit.

4.3.5. Photonic Science sCMOS 4MP_68

The Photonic science CMOS detector (sCMOS 4MP_68) is an active pixel indirect semiconductor detector that uses a 10 µm thick GadOx scintillator coupled to the sensor via a fibre taper. It has a nominal pixel size of 23.4 µm resulting from a field of view of 48 mm by 48 mm and resolution of 2048 pixels in both directions [Scia] on the scintillator plain. The pixels are otherwise not structured. The semiconductor is cooled to −25 °C using thermoelectric cooling coupled to a water chiller. The detector offers two gain modes, a high and a low gain mode. During measurements, the high gain mode lead to an instant saturation of the pixels, hence the low gain mode is used.

Characterisation measurements are taken at 100 ± 2 cm distance between the source and the detector. The LMJ X-ray tube is set to 30 kV acceleration voltage, 20 W power and 20 µm spot size.

Noise characteristics: Data points for noise characterisation of the Photonic Science CMOS are taken for integration times between 1 s and 60 s with increasing spacing for higher integration times. Each integration time is sampled with at least ten individual images. An area, containing 40 by 40 pixels, close to the centre but wholly contained within a hexagonal structure shown later is chosen for analysis.

As seen in Figure 4.18a, the mean signal $\mu_{\text{flat}} - \mu_{\text{dark}}$ increases linearly up to the 40 s data point, after which saturation effects start to set in, seen as a deviation from the ideal linear behaviour. The measured counts of about 50,000 ADU at this point are far below the maximum ADC output value of 64,000. Therefore, saturation happens in the pixels and not the ADC as seen in subsection 4.3.2. The *SNR* rises quickly to values

around 70 after just 5 s. For higher integration times, the SNR increases even further to values about 150.
The results of the dark frame measurements, shown in Figure 4.18b, indicate that the detector has very little dark current noise as σ_{dark} is constant with the exception of the 40 s data point. The fit in Figure 4.18b contains additional information about the dark current within the detector. The parameters

$$D(t) = (1.13 \pm 0.28)\,\frac{\text{ADU}}{\text{s}} \cdot t + (840.2 \pm 0.8)\,\text{ADU} \tag{4.35}$$

are obtained. The low dark current rate confirms, that dark current noise contributes less to the overall noise in the flat frames than the readout noise. The dark current data points show deviations from the expected linear behaviour, especially at 40 s, where both the dark current and the dark noise is significantly higher than expected. A cause for these deviations could be an instability in temperature control, that lead to fluctuations in temperature. A higher temperature would be consistent with the increased dark current and noise at 40 s.
The linearity of the response is examined for the detector using a fit to the mean signal in Figure 4.18a. The detector shows larger deviations from linearity for short integration times and once again for long integration times, as can be seen in Figure 4.19. The deviation at lower integration times also appears for other detectors and is probably an artefact of the method. The deviation at larger integration times coincides with the saturation effects starting at around 50, 000 ADU. For integration times between these values, the measured deviation from linearity is within a 2.5% margin and therefore suitable for most applications.

Spatial resolution: The spatial resolution of the Photonic Science CMOS camera is determined using the slanted-edge method in both major directions and tilted 45° relative to the pixel array. The results are shown in Figure 4.20. As seen for other detectors, the $MTFs$ in both major directions are indistinguishable, whereas the MTF measured diagonally is slightly worse. Compared to most of the other detectors examined so far, the MTF shows a slightly different behaviour. It drops quickly for low frequencies, reaches its 50% point at about 4.6 lp/mm followed by a long stretch of comparatively slow decrease in contrast. This behaviour stems from a point-spread function, that has a thin peak, but a wide base, hence the 50 % point is reached so early. A point-spread function of this shape is produced, if a small number of photons propagates far from the location of their creation, while most photons are collected close to their place of origin. The scintillator used in the camera has no structures to prevent photon propagation over multiple pixels. On the other hand, its thickness of 10 µm means that most photons enter the fibre taper quickly. The observed MTF is therefore consistent with the design of the scintillator.

Fibre taper: The fibre taper used to couple the scintillator to the CMOS sensor influences the images taken with the camera. Figure 4.18a shows a flat frame image taken with

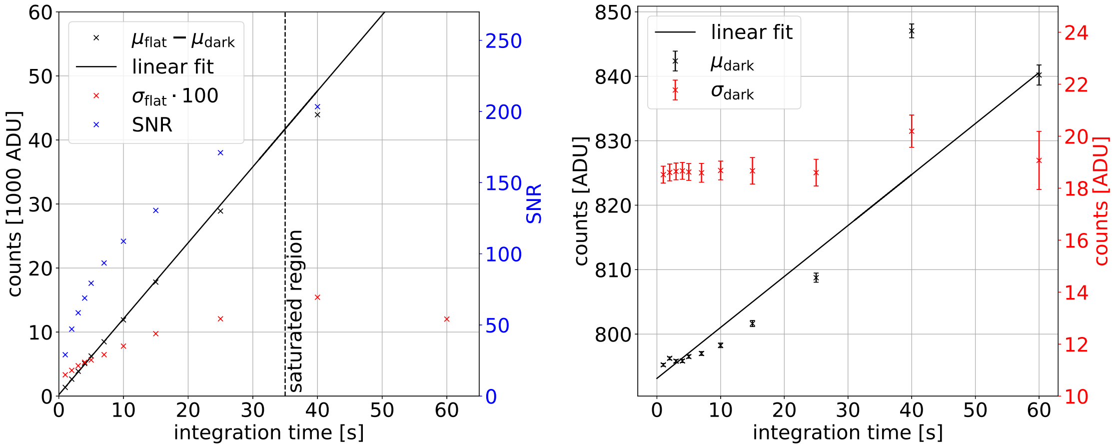

(a) Flat frame noise characteristics of the Photonic Science CMOS detector. The units are counts in ADU over integration time in seconds. Black data points represent the mean signal, red data points the noise. The solid black line represents a linear fit. The blue data points use the right y-axis and show the SNR. Points lying right of the dashed black line are saturated.

(b) Dark frame noise characteristics of the Photonic Science CMOS detector. Black data points represent the mean pixel values in ADU. Red data points show use the right y-axis and show the measured pixel value standard deviation in ADU. Both are plotted over the integration time in seconds. The solid black line represents a linear fit to the mean pixel values.

Figure 4.18.

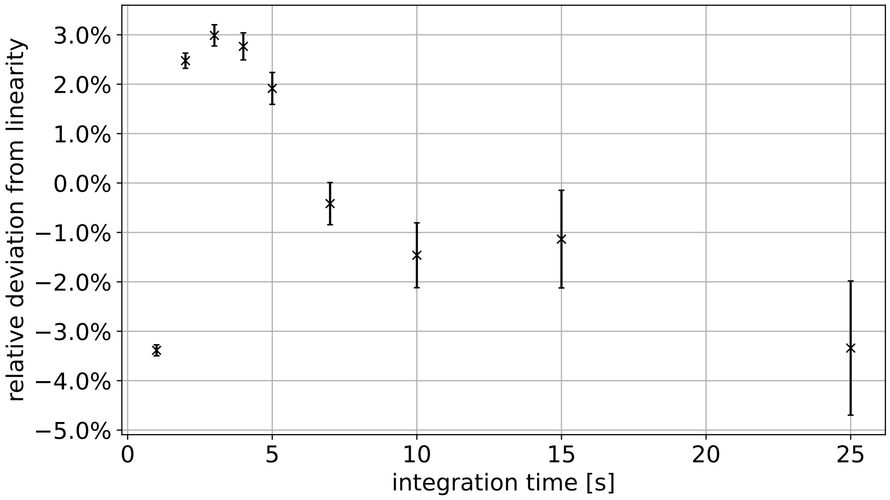

Figure 4.19.: Relative deviation from ideal linear behaviour of the Photonic Science CMOS detector over integration time in seconds.

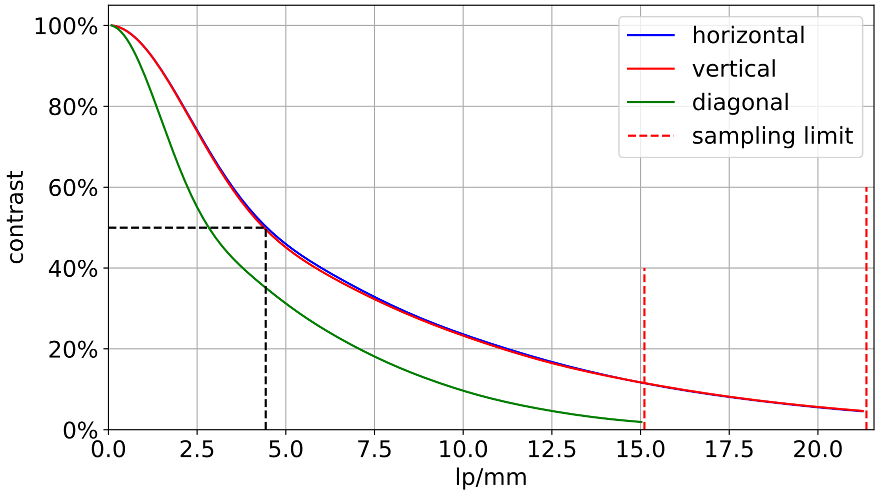

Figure 4.20.: Spatial resolution of the Photonic Science CMOS detector. Shown are the $MTFs$ in horizontal, vertical and diagonal directions relative to the pixel edges. They indicate the retained contrast depending on the spatial frequencies in lp/mm. The dashed red line represents the sampling limits due to the pixel pitch. The effective diagonal pixel pitch is calculated as $\sqrt{2}$ times the pixel pitch, assuming a square pixel shape. The dashed black lines indicate the location at which the contrast decreases to 50% for the two main detector axes.

the camera with 25 s integration time. Two major structures can be seen within this flat frame. The entire image contains a hexagonal pattern that stems from the fibre taper. The boundaries of the hexagons show lower counts than the areas within them. This is the reason for choosing a ROI within a single hexagon for the noise analysis. The other structure is a large scale irregular pattern mainly in the right half of the image also showing reduced measured intensity.

A line plot through the larger pattern is shown in Figure 4.21b. Large differences in counts can be seen in this line plot. The dotted lines in Figure 4.21b indicate the maximum and minimum counts measured in this pixel line. Compared to the mean count of both values they differ by about 30%. The structure responsible for this difference is caused by a defect in the GadOx scintillator. According to the manufacturer, parts of the liquid scintillator material did not properly crystallise during production. Additionally, changes in the structure, that look like small crystals formed in the two month of test measurements have been observed. They are the result of crystallisation processes from the uncrystallised scintillator material. These structures are removed from images by a gain correction. However, defective areas measuring fewer photons will suffer from worse signal-to-noise ratios.

The fibre taper also introduces mapping errors to the image, skewing objects over the field of view. This effect is easily corrected by remapping the pixels. The manufacturer calibrated a remapping image that determines how counts need to be moved from one pixel to another to produce images without the mapping error. The acquisition software offers multiple modes for this remapping. It can also be turned off completely, which

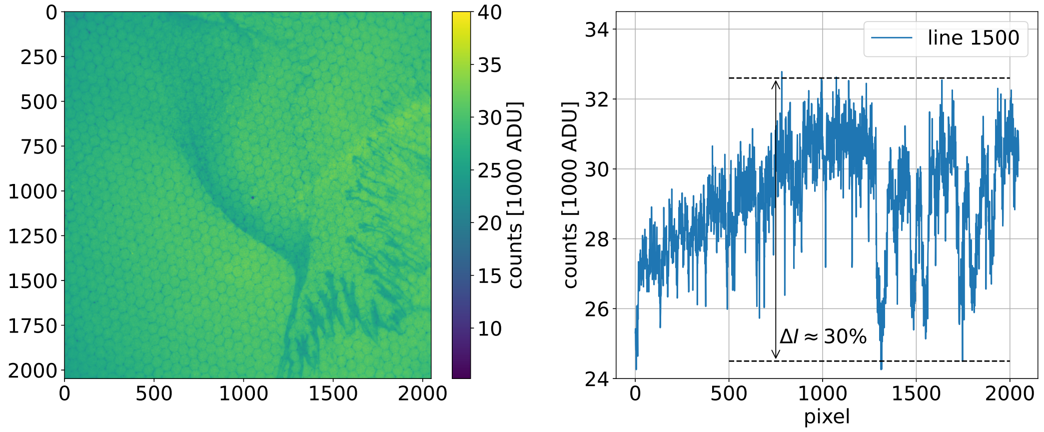

(a) Flat frame image of the Photonic Science CMOS taken at 30 kV and 25 s integration time. Visible is the hexagonal pattern caused by the fibre taper and a large dark structure from scintillating material that did not crystallise properly.

(b) Pixel line 1500 of the flat frame in Figure 4.21a. Shown are the counts of each pixel in ADU over the horizontal pixel position. The dark structure causes absorption of up to 30% of incident radiation, indicated by the dashed black lines.

Figure 4.21.

is not recommended, since there is currently no easy way of performing the correction after the image is taken. If the remapping is enabled, the pixel values can be additionally clipped and smoothed. According to the manual, clipping removes edge irregularities and smoothing applies sub pixel interpolation [Scib]. The MTF of the detector with the different settings is measured using the slanted-edge method. The results are shown in Figure 4.22. Two groups of $MTFs$ that differ in contrast for higher spatial frequencies can be seen. The $MTFs$ with no remapping, only remapping and remapping and smoothing form one group, where the contrast at higher frequencies is retained. The other MTF group, consisting of remapping and clipping and all corrections, lose contrast beginning at the 50% contrast point, compared to the first group. No additional information is provided by the manufacturer as to how exactly these two corrections influence the image. However, the manual states, that the clip option is useful, if sub areas of the sensor are read out. When using the full field of view, the clip option is therefore best left disabled.

Protective cover: The scintillator is not light tight and needs an additional cover to prevent ambient light from reaching the sensor. Two different materials are tested for this purpose. First, aluminium foil is used. It blocks visible light as well as helps with dealing with electromagnetic interference. The second cover tested consists of black carton.
The foil reflects the scintillating light, that is emitted towards the entry window back onto the scintillator. Due to the air gap of about one centimetre between the cover and the scintillator, a smearing of the signal over very large regions follows. This effect is

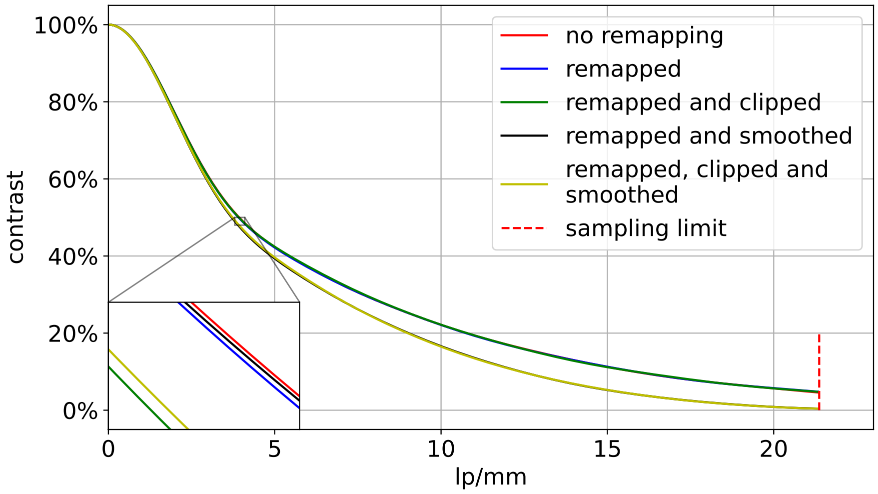

Figure 4.22.: Influence of the different remapping settings on the *MTF* of the Photonic Science CMOS camera. The figure shows *MTFs* taken with different settings available to compensate for the mapping error caused by the fibre taper.

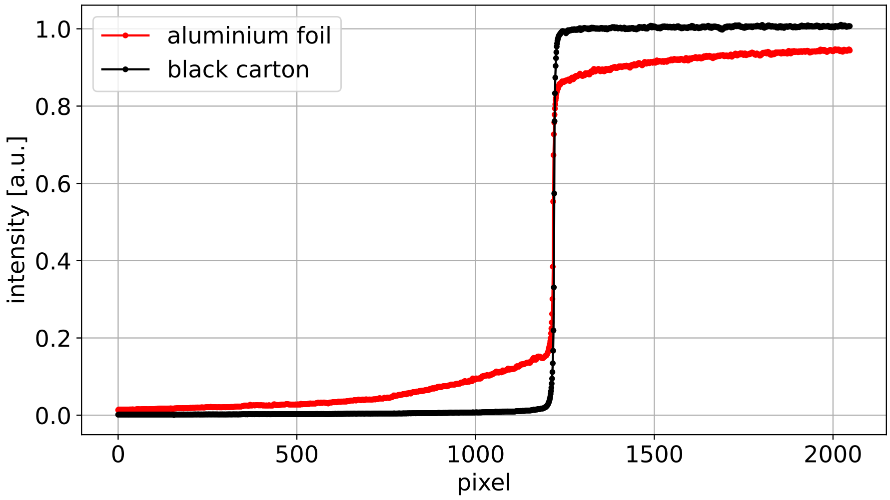

Figure 4.23.: Edge spread functions of the Photonic Science CMOS in ADU over pixel position taken with different protective covers. The reflection of scintillating light on the aluminium foil as cover moves counts from the bright area towards the dark area and thereby widens the edge, worsening contrast.

shown in Figure 4.23. The figure shows the edge spread functions of the Photonic Science CMOS camera once with aluminium foil as cover and once with a cover made from black paper. The edge with the paper cover is imaged sharper. Additionally, the maximum value of the ESF with aluminium is lower than for the other ESF. This effect can be explained as follows. During flat frame measurements for gain corrections the entire detector area is illuminated more or less uniformly. All emissions towards and reflections by the aluminium foil average out. The tungsten edge blocks a large area from exposure to X-rays. Hence, no emission of scintillating photons happens in this region and the averaging does not work. Instead, a net flux of photons from stronger illuminated areas towards darker areas is created.

The Photonic Science CMOS camera shows better noise and resolution characteristics than the imaging plates. It additionally provides all the benefits of a digital detector, like the electronic shutter and ease of use, while the active cooling keeps the influence of thermally generated charge carriers negligibly small for integration times under a minute. Exposures that create signals over $50,000\,\mathrm{ADU}$ should be avoided as saturation behaviour of the detector response start to set in at this signal strength. The detector is also suitable as a higher resolution, lower dark noise alternative to the Dalsa Shad-o-Box. This approach is most beneficial in low photon number and higher exposure time applications, or if the additional resolution is required. The remapping option is best set to only remapping with no additional corrections, as this yields the rawest images with the least amount of unknown modifications and without mapping errors. A non-reflective cover in front of the scintillator is absolutely necessary to prevent incident environmental light and reflected scintillating light from reaching the CMOS sensor.

4.3.6. Andor iKon-M SO

The Andor iKon-M SO is a direct detection CCD detector with a pixel pitch of $13\,\mu\mathrm{m}$, a resolution of 1024 by 1024 pixel and a field of view of 13 mm by 13 mm [Tec]. Its sensor is cooled by a thermoelectric element to $-25\,^{\circ}\mathrm{C}$. The lack of scintillating material means that the quantum efficiency decreases quickly for photon energies higher than 10 keV [Tec]. This imposes a restrictive limit on the usability of the detector and excludes it from grating-based X-ray phase-contrast imaging applications, where the gratings absorb large amounts of the low energy X-rays.
The LMJ is set to 30 kV, 20 W and $20\,\mu\mathrm{m}$ spot size. The Andor iKon is placed at a distance of $100 \pm 2\,\mathrm{cm}$ from the source.

Noise characteristics: Images with integration times between 1 s and 45 s are taken under illumination and with no active X-ray source. For each integration time, ten images are taken. A ROI containing 30 by 30 pixels is chosen. The results of the characterisation are shown in Figure 4.24a. The mean signal $\mu_{\text{flat}} - \mu_{\text{dark}}$ increases linearly with time until saturation starts to set in at 25 s. The saturation is first seen as a decrease in the noise σ_{flat}, as explained in subsection 4.3.2, before the signal reaches a maximum value of about $44,000\,\mathrm{ADU}$. The SNR increases as well, up to a value of about 10 at 15 s, at

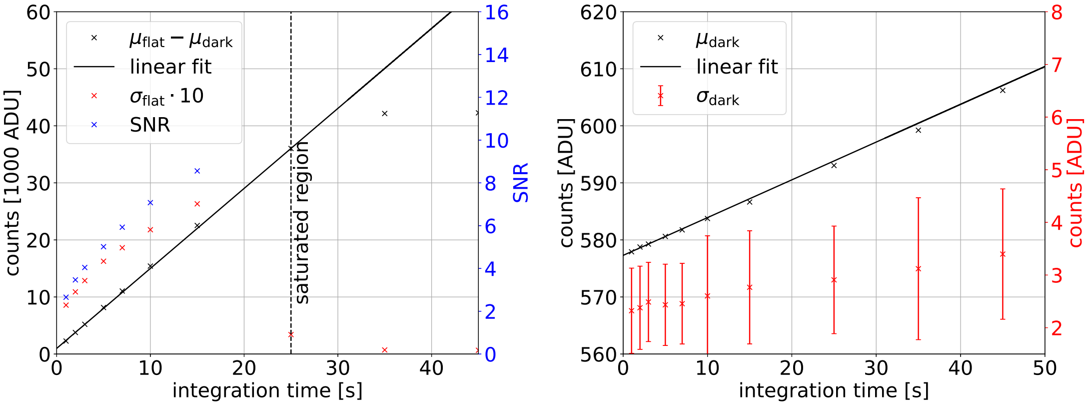

(a) Flat frame noise characteristics of the Andor CCD detector. The units are counts in ADU over integration time in seconds. Black data points represent the mean signal, red data points the noise. The solid black line represents a linear fit. The blue data points use the right y-axis and show the SNR. Points lying right of the dashed black line are saturated.

(b) Dark frame noise characteristics of the Andor CCD detector. Black data points represent the mean pixel values in ADU. Red data points show use the right y-axis and show the measured pixel value standard deviation in ADU. Both are plotted over the integration time in seconds. The solid black line represents a linear fit to the mean pixel values.

Figure 4.24.

higher integration times, the decrease in noise due to the cut-off of high intensities in the ADC makes a meaningful determination of the SNR impossible.

Figure 4.24b shows the results for the dark frame analysis. The cooled CCD sensor shows only small amounts of noise in the dark frames. The comparatively large uncertainties make it impossible to say, whether the noise increases with integration time. A fit is performed to the mean dark counts μ_{dark} in order to characterise the dark current. The resulting fit parameters are

$$D(t) = (0.62 \pm 0.06)\,\frac{\mathrm{ADU}}{\mathrm{s}} \cdot t + (577.2 \pm 0.3)\,\mathrm{ADU}. \tag{4.36}$$

Hence, the dark current rate is very low with only 0.62 ADU per second.

A fit is also conducted to the mean signal in Figure 4.24a, in order to examine the detector's response to different intensities of X-ray incidence. The relative deviation of the response from ideal linear behaviour is plotted in Figure 4.25. At 1 s integration time, the deviation is the largest with about 2.5%, again this is probably caused by the method itself rather than stemming from the detector. At higher integration times, the deviation decreases to values lower than 1.5% and stays in this range over the non-saturated part of the studied integration times.

Spatial resolution: The slanted-edge method is used to determine the spatial resolution of the Andor iKon CCD camera in horizontal, vertical and diagonal directions relative to

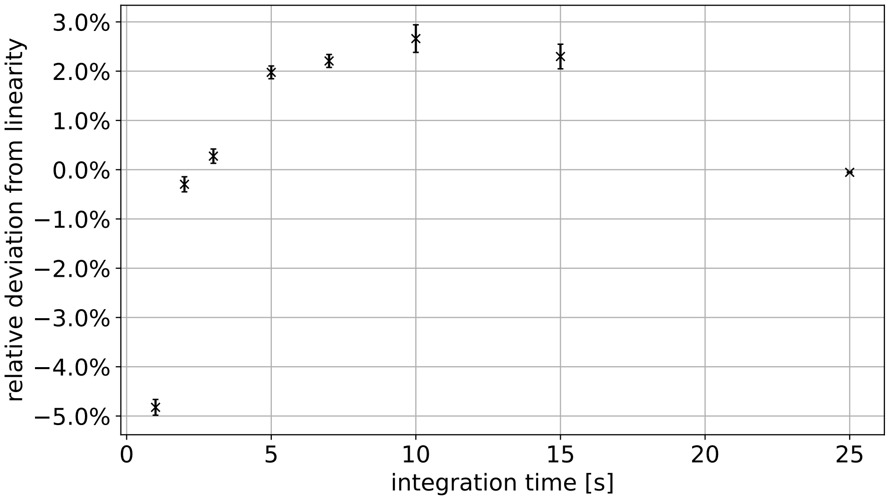

Figure 4.25.: Relative deviation from ideal linear behaviour of the Andor CCD detector over integration time in seconds.

the pixel edges. The sensor is recessed a few centimetres in its vacuum housing behind a carbon cover. The tungsten edge is placed directly in front of this cover, meaning that it is placed a few centimetres away from the sensor, possibly causing a reduction in measured contrast. The results of the slanted-edge method are plotted in Figure 4.26. As with all detectors before, the $MTFs$ for the major directions of the detector are practically equal, while the diagonal MTF is slightly worse. Unlike most of the other detectors, the decrease in contrast is slow, even at high spatial frequencies. The 50% point in horizontal and vertical direction is reached at about 35 lp/mm, which is 90% of the sampling limit of 38.4 lp/mm. This distinct behaviour stems from the fact that the Andor CCD is a direct detection detector with no scintillator smearing the signal over multiple sensor pixels.

The main advantage of the Andor iKon-M SO CCD is its superior spatial resolution. Compared with the Rigaku XSight Micron, the only other detector with an even better resolution, the Andor retains acceptable integration times. On the other hand, the comparatively small field of view of only $1.3x1.3\,\mathrm{cm}^2$ and the sharp decrease in quantum efficiency for photons with energies higher than 10 keV limits its usability in X-ray imaging applications, especially in gbpci.

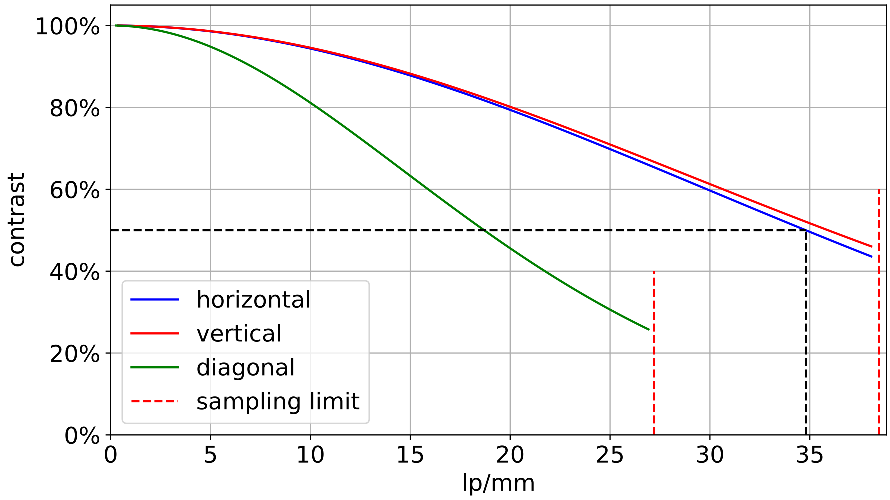

Figure 4.26.: Spatial resolution of the Andor CCD detector. Shown are the $MTFs$ in horizontal, vertical and diagonal directions relative to the pixel edges. They indicate the retained contrast depending on the spatial frequencies in lp/mm. The dashed red line represents the sampling limits due to the pixel pitch. The effective diagonal pixel pitch is calculated as $\sqrt{2}$ times the pixel pitch, assuming a square pixel shape. The dashed black lines indicate the location at which the contrast decreases to 50% for the two main detector axes.

4.4. Comparison of detectors for use at PHELIX

The Petawatt High-Energy Laser for Heavy Ion EXperiments (PHELIX) at the GSI Helmholtzzentrum für Schwerionenforschung in Darmstadt is a high-power laser, that can be used for backlighter experiments. These backlighter experiments pose unique challenges on the imaging setup. One of the main challenges is the low photon flux.

In order to maximise the amount of photons that contribute to the signal, the object to be imaged is best placed as close as possible to the backlighter source, increasing the solid angle that the object occupies. With the object position fixed, the detector position is constrained by the required magnification and the field of view of the detector. Since experiments are conducted in vacuum, where radiation is not absorbed, long source-detector distances are in principle possible. Hence, the spatial resolution of the detector is not as important as an insufficient resolution can be compensated by increasing the magnification.

The Photonic Science CMOS, the imaging plates and the Andor CCD are compared for their potential use at the PHELIX backlighter experiment using the data acquired at the liquid metal jet X-ray tube. Although the conditions are not the same, a characteristic emission line around 11 keV photon energy is present at the X-ray tube [AB21]. This is close to the design energy of the 2020 PHELIX setup and the weighted mean energy of the backlighter spectrum of $11 - 12\,\text{keV}$ [Sei+20].

A way of improving the photon noise characteristics of a detector is binning its pixels; Multiple pixels are averaged to increase the SNR compared to an individual pixel. The

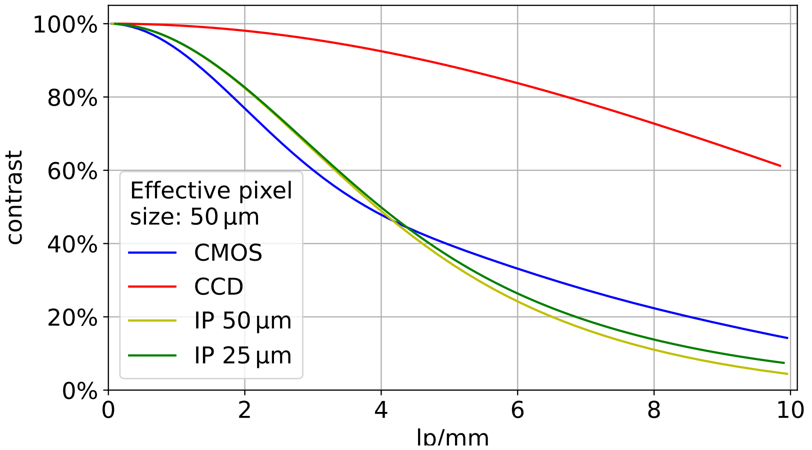

Figure 4.27.: $MTFs$ of detectors considered for the PHELIX experiment. The measurement behind the IP indicates the scan width used. The Andor CCD is binned four by four, the Photonic Science and IP 25 two by two, whereas the 50 µm scan width data is used without binning.

raw images from the detectors are binned to an effective pixel size prior to analysis. Since the measurements for the different detectors are conducted at the same source detector distance, the number of photons per binned pixel is equal, removing the influence of different pixel pitches on SNR.

Spatial resolution: The spatial resolution is examined for an effective pixel size of 50 µm using the slanted-edge method. Tungsten edge images taken for the characterisation of the Photonic Science and Andor CCD cameras in horizontal direction are rebinned by averaging two by two and four by four pixels respectively. For the imaging plate, both the data scanned with a scan width of 50 µm is taken where no rebinning is required, and the 25 µm scan width data, that is rebinned two by two pixels. All images are then analysed using the slanted-edge method.
The results are shown in Figure 4.27. The Andor iKon CCD retains its superior resolution compared to the other two detectors. The imaging plates and Photonic science CMOS show very similar contrast over the entire range of spatial frequencies. While the CMOS camera initially loses slightly more contrast with increasing spatial frequency, at around the 50% contrast point the $MTFs$ intersect. After the intersection, the CMOS camera shows a better spatial resolution for the rest of the range until the sampling limit at 10 lp/mm. Both imaging plates are indistinguishable up to this intersection point, then the rebinned 25 µm scan width scan is able to retain a slightly higher contrast.
The similar resolution of the CMOS camera and the imaging plates means, that the two detection systems can be used interchangeably, without the need of altering the magnification of the setup.

Noise characteristics: The SNR of the possible PHELIX detectors is examined for four different effective pixel sizes, from 25 µm to 100 µm. The images taken for the characterisation of the individual detectors are binned by averaging over different numbers of neighbouring pixels. The same regions of interest as in section 4.3 are then used to calculate the mean μ and standard deviation σ of the binned images following Equation 4.20. These means and standard deviations are combined according to Equation 4.22, to obtain the estimates for the SNR. Comparing the different detectors at the same effective pixel sizes has the additional advantage of equalizing the number of photons per pixel. Figure 4.28 summarises the results. It shows the $SNRs$ for the four different effective pixel sizes over an equivalent to the number of photons per unit area. Together with the binning, an x-axis proportional to the number of photons per pixel is created, allowing for easy comparison of $SNRs$ of different detectors. The error bars in x-direction reflect the uncertainty of the number of photons per unit area due to the uncertainty in distance from the source and due to uncertainty in integration time according to Gaussian error propagation via

$$\Delta \frac{t_{\mathrm{int}}}{d_{\mathrm{sd}}^2} \cdot N_{\mathrm{photon}} = \sqrt{\left(\frac{1}{d_{\mathrm{sd}}^2} N_{\mathrm{photon}} \cdot \Delta t_{\mathrm{int}}\right)^2 + \left(\frac{t_{\mathrm{int}}}{2 \cdot d_{\mathrm{sd}^3}} N \cdot \Delta d_{\mathrm{sd}}\right)^2}. \tag{4.37}$$

For both digital detectors an uncertainty of $\Delta t_{\mathrm{int}} = 10\,\mathrm{ms}$ on the integration time is assumed. The uncertainty on distance from source to detector for all detectors is estimated to be $\Delta d_{\mathrm{sd}} = 2\,\mathrm{cm}$. The uncertainties on integration time for the imaging plates are as described in subsection 4.3.4. The binning reduces the sample size with increasing binning factor, increasing the uncertainties on σ_{flat} and S.

Each segment in Figure 4.28 contains the SNR of the detectors for a specific effective pixel size, if the effective pixel size is an integer multiple of the original pixel size. Beginning at 25 µm, where the Photonic Science CMOS shows the best SNR over the entire measurement range. The Andor CCD is worse than both the imaging plates and the Photonic Science camera. Continuing with 50 µm effective pixel size, the larger scan width of the imaging plate is added. It is slightly worse than the imaging plate scanned with 25 µm binned two by two. All detectors show an improvement in SNR. At 75 µm effective pixel size, the noise performance of all detectors improves again. However, the improvement is now less than for the step before. The last effective pixel size examined is 100 µm. The two different scan widths of imaging plates perform practically equal at this pixel size, but still slightly worse than the Photonic Science, especially at low photon numbers. The improvement of performance of the Andor is now less than it is for previous binning steps and the eight by eight binning starts to negatively impact individual points differently, indicating that the binning algorithm introduces artefacts into the images.

The Photonic Science CMOS camera shows the best SNR, when compared to the other two detectors. In the measured range, a small improvement over the imaging plates used thus far can be expected. The photon sensitivity of the Andor CCD is the worst of the three detector systems. A reason for this is the decreasing quantum efficiency of the Andor CCD for photon energies higher than 10 keV [Tec]. When used in conjunction

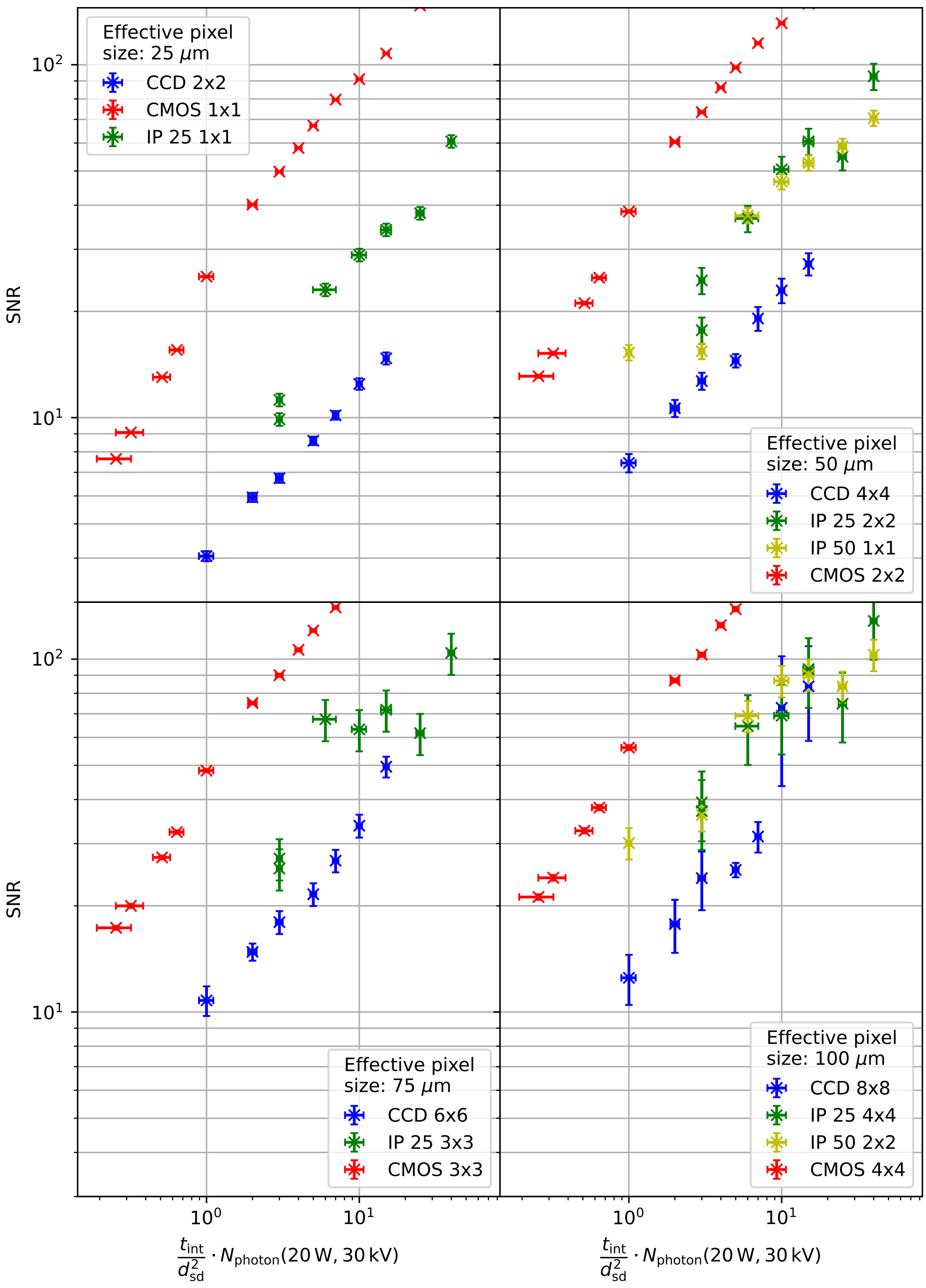

Figure 4.28.: Photon noise characteristics of multiple detectors usable at the PHELIX experiment: Photonic Science **CMOS**, Andor iKon **CCD** and the **I**maging **P**lates. Shown are the photon noise estimates over X-ray intensity for different effective pixel sizes achieved by binning the detectors. The numbers following the detector names are the numbers of pixels binned.

with an interferometer for grating-based X-ray phase-contrast imaging the Andor will see a further decrease in photon sensitivity, as a large part of the low energy photons is absorbed by the gratings. Using the Andor CCD offers therefore no improvement over the imaging plates.
Binning the images can improve the photon sensitivity at the cost of spatial resolution. For the detectors tested, an effective pixel size of either 50 µm or 75 µm is viable. At 75 µm effective pixel size, the improvement is already less than for the 50 µm pixel size. Going to larger pixel sizes reduces the improvement further.

Conclusion and outlook: The results indicate, that compared to the imaging plates used during the 2020 experiments, small improvements in photon noise performance can be expected from the Photonic Science CMOS camera. However, verifying that this improvement actually follows would require measurements at the backlighter for several reasons. The spectra of the liquid metal jet and the backlighter are similar, but not equal. Additionally, the gain correction of the Photonic Science CMOS camera poses a serious challenge, due to the variation of the X-ray flash from shot to shot. If the gain correction is not performed properly, additional fixed pattern noise will be seen in the resulting images, reducing the SNR.
The photonic Science CMOS camera received a new scintillator after the measurements for this thesis were performed. The new scintillator has an increased thickness of 30 µm, improving the scintillator quantum efficiency from about 50% to over 70% at 12 keV according to the manufacturer and thereby improving the quantum efficiency. The thicker scintillator will decrease the spatial resolution. The detector's performance should therefore be reevaluated once the detector returns from the manufacturer. Furthermore, the high gain mode of the Photonic Science CMOS could be tested to see whether it provides additional improvements regarding the noise characteristics in low light environments.
Should a fallback to the imaging plates be necessary, the 50 µm scanning width should be chosen, since the resolution gain with 25 µm scanning width is not worth the decrease in noise performance. The small field of view of the Andor iKon CCD and its quickly decreasing quantum efficiency for photons with higher energies than 10 keV make it unsuitable for the planned backlighter experiment, although its direct detection approach is promising.
The Jungfrau detector [Sch22], a different direct detection semiconductor detector, will be investigated soon. In the following a short outlook on its promising features is given. The Jungfrau detector uses gain switching on an individual pixel basis to achieve single photon sensitivity in addition to a high dynamic range. In conjunction with high frame rates (> 1 kHz) suppressing dark current, the only noise source impacting SNR is photon noise [Red+18]. Furthermore, the Jungfrau detector is sensitive to 12 keV photons and its spatial resolution is limited by its pixel pitch of 75 µm [Jun+14]. Each pixel is individually gain calibrated making a gain correction superfluous. Hence, the Jungfrau detector is superior to the tested detectors in every regard.

5. DPC resolution phantom

The last step in grating-based X-ray phase-contrast imaging is the image reconstruction process, described in subsection 2.4.4. In this chapter, the influence of the reconstruction algorithm and the parameters of the Moiré pattern on the spatial resolution within the DPC image is examined. A phantom is designed and characterised in regard to manufacturing defects. The phantom is subsequently used to perform slanted-edge measurements within DPC images to determine the spatial resolution.

5.1. Design of the phantom

To use the slanted-edge method for resolution measurements, the phantom needs to produce a signal in the DPC images similar to the attenuation signal produced by the tungsten edge. According to Equation 2.19, the phase signal $\Delta\Phi$ for a homogeneous material is proportional to the derivative of its thickness profile d_{obj}:

$$\Delta\Phi(x) \propto \delta \cdot \frac{\partial d_{\mathrm{obj}}}{\partial x} \tag{5.1}$$

The desired $\Delta\Phi$ is in the ideal case a Heaviside function. Differentiating a triangle function yields a similar signal. Both sides of the peak have an equal but opposite slope. At the maximum, the derivative of the triangle function therefore jumps from a positive to a negative value. Hence, the signal producing parts of the target are determined to be triangular prisms.

Due to the polychromatic spectrum of the X-ray source and the dependence of $\delta(z)$ on the photon energy (see Equation 2.20), a prediction about the absolute DPC signal amplitude is difficult, but increasing the slope of the prism increases the thickness gradients and therefore the expected signal. To ensure a usable phantom is obtained, multiple prisms with different angles are placed on the phantom. The resulting design is shown in Figure 5.1. The design consists of a support plate on which six triangular prisms with decreasing surface slope are placed. The support plate edge is angled on two sides, helping with tilting the edge in an angle of 3° to 10° as required by the slanted-edge method. Further structures are present to help with aligning the edges of the phantom within the field of view during measurements.

The phantom is manufactured from a 6 mm PMMA plate, as PMMA produces a weak absorption signal. The structures are milled from this plate using a five axes CNC milling machine. The support plate is thinned down to 3 mm, whereas the tips of the prisms are left at the original 6 mm height.

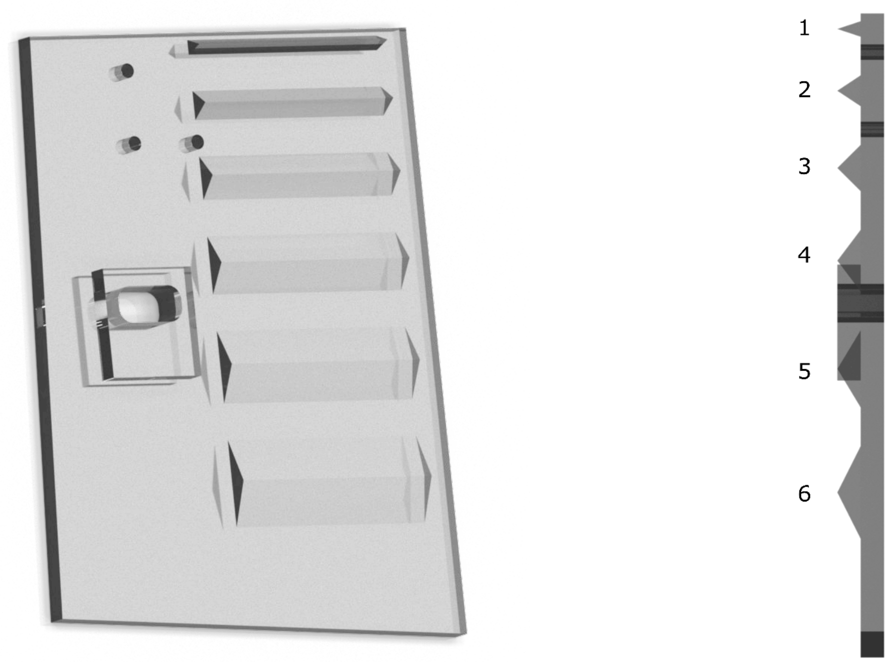

(a) Front view of the DPC phantom design.

(b) Side view of the transparent DPC phantom.

Figure 5.1.: Rendered images of the DPC phantoms design. The six triangular prisms produce a DPC signal similar to an *ESF*. They are numbered from steepest to least steep as shown in the right image.

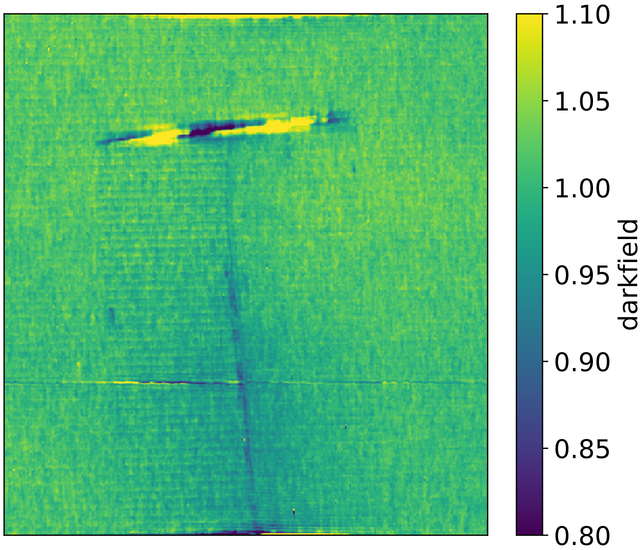

Figure 5.2.: Darkfield image of the second prism. The signal seen in the top of the image corresponds to the upper limit of the prism. The vertical line below in the centre of the image is located at the prism's ridge. The corresponding area of the DPC phantom can be seen in Figure A.8.

5.2. Phantom characterisation

A characterisation of the target is required, due to potential issues caused by the design or manufacturing process. A probable failure point are the ridges of the prisms, as they are the most likely parts to break or splinter when subjected to heat and mechanical stress during manufacturing. However, the ridges are also the most important part of the structure, as they lie in the transition region of the ESF. Another aspect is manufacturing precision possibly introducing object noise through surface roughness. Especially around the ridge, object noise could lead to noise contributions that do not average out properly, causing problems during the binning process of the slanted-edge method.

A visual inspection after manufacturing reveals that the ridge of the first prism is damaged. The top part of the ridge is broken off, making the prism unusable for the intended purpose. All other peaks with less surface inclination show no visible damage.

All prisms are examined using grating-based X-ray phase-contrast imaging next. A setup consisting of the 8078 $G1$ and the 1626 $G2$ is used at the liquid metal jet X-ray tube. The phantom is placed 42 $\pm$ 1cm from the source and at a distance of 67 $\pm$ 1 from the detector. The phantom is therefore magnified by a factor of about 2.6. Images are taken for each prism with the Dalsa Shad-o-Box. The tube is set to 30 kV voltage, 20 W power and 20 µm spot size.

Figure 5.2 shows the darkfield image of the second prism of the DPC phantom. The image shows a part of the prism close to its upper edge. The near horizontal line in the

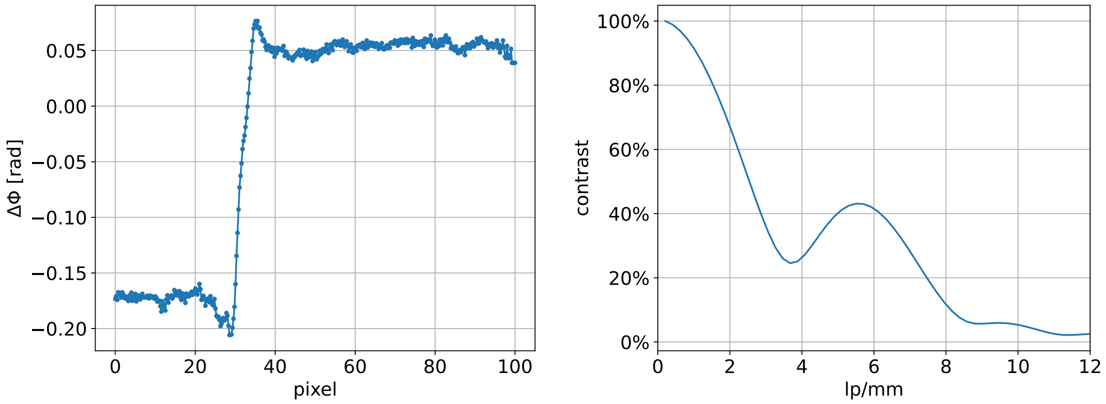

(a) Edge-spread function of the second prism ridge as determined using the slanted-edge method. Apart from the expected edge structure, structures are visible around the transition region. These signal swings cause problems shown in the right plot.

(b) *MTF* resulting from the *ESF* shown in the left plot. The structures around the edge region also cause structures within the *MTF*. This makes data from the second prism unusable.

Figure 5.3.

top part of the edge marks the upper edge of the prism. Most of the support and prism area produces no darkfield signal, represented by darkfield values close to one. At the location of the prism's ridge, the darkfield image shows lower values, indicating small angle scattering. The presence of small angle scattering suggests damage to the ridge structure, creating a rough surface or cracks. No dark field signal can be seen at the ridge locations of the other prisms.

An analysis is attempted to the second prism to examine the impact of the possible defects at the ridge. After the DPC image is retrieved, a ROI containing most of the prism is chosen. Within this ROI, the slanted-edge analysis as described in section 4.1 is performed. The *ESF* retrieved from the DPC data is shown in Figure 5.3a. While containing the expected transition in signal from negative to positive phase shifts, the data also contains strong signal swings at both sides of the edge. The signal swings negatively impact the resulting *MTF* plotted in Figure 5.3b. The measured contrast first decreases as expected, until at around 3.8 lp/mm, where a local minimum is reached. After this minimum, a local maximum follows at around 5.8 lp/mm. These structures in the *ESF* and subsequently *MTF* corroborate that the ridge of the second prism is damaged, and it is therefore not used in further measurements.

The third prism is used to examine the surface roughness of to assess manufacturing precision. Fifty images of the prism are taken with an integration time of 30 s each, totalling 25 min exposure time. The DPC images are retrieved individually and the noise in the DPC is examined. First, a standard deviation in each pixel over the set of images is calculated. A map of this standard deviation is shown in Figure 5.4 a), it is mostly uniform over the ROI with values between 0.15 rad and 0.2 rad. The only features are

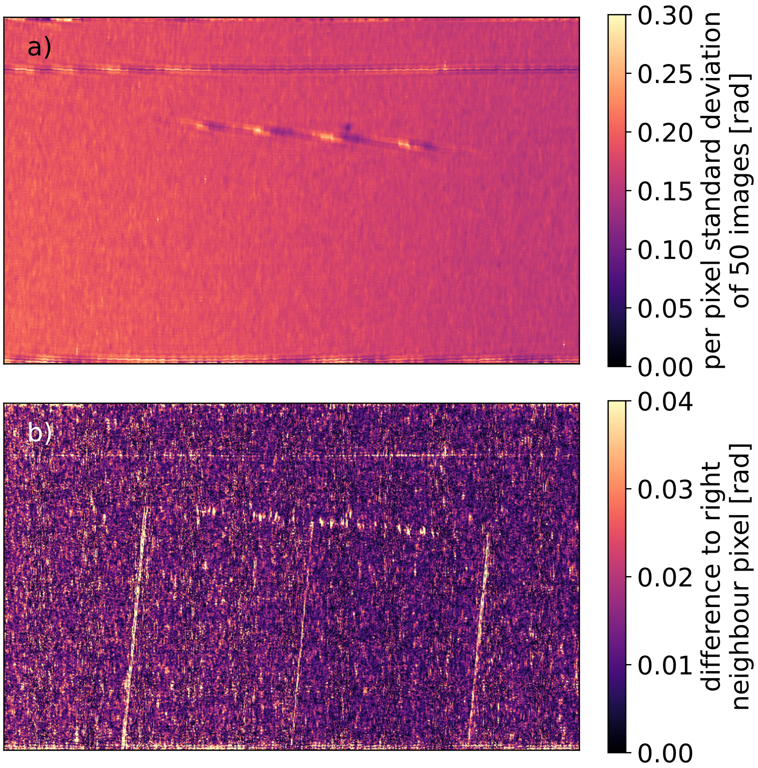

Figure 5.4.: Surface roughness plots for the DPC phantom. Both images contain the same area, it is shown in Figure A.8. A thin line indicates the border of the support plate. Slightly below, shown as a shorter, tilted line is the edge of the third prism. a) shows the standard deviation of DPC values between 50 images, whereas b) shows the difference between two neighbouring pixels after the 50 images are averaged.

two horizontal lines in the upper third of the image. These lines are the upper edges of the prism and an artefact from a grating defect. Next, all the DPC images are averaged, and the differences between two horizontally neighbouring pixels are evaluated. This is the direction in which the setup is sensitive to phase shifts due to the orientation of the grating bars. Figure 5.4 b) shows the difference between two neighbouring pixels. The image contains the same two horizontal lines seen in the standard deviation between the fifty DPC images. Additionally, the other edges of the prism and the peak ridge are visible, since they are the locations where the differential phase changes the most in horizontal direction. The areas containing the angled surfaces and the support plate contain differences in DPC an order of magnitude smaller than standard deviation between images shown in Figure 5.4 a). Hence, the random fluctuations within a pixel are larger than the systematic difference between two pixels caused by surface roughness. The manufacturing precision is therefore sufficient to use the phantom for the intended purpose, except for the first and second prism which are damaged and can not be used.

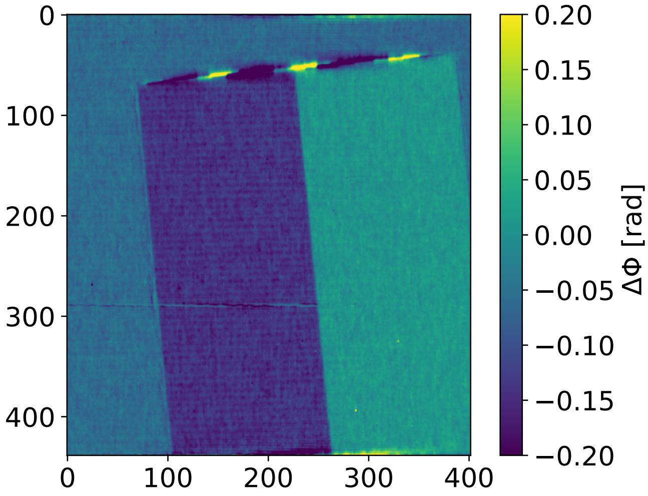

Figure 5.5.: DPC image of the third DPC phantom prism. The structure covering most of the image is the prism. It is surrounded by the supporting plate. The two inclined surfaces of the prism show different differential phase values than the supporting plate. The area of the phantom covered in this image is shown in Figure A.8.

5.3. Data acquisition and processing

The third prism of the DPC resolution phantom is used for measurements, since the strongest DPC signal among the intact prisms can be expected from it. The prism is imaged using the liquid metal jet X-ray tube with the Dalsa Shad-o-box and the Photonic Science CMOS detector. The acceleration voltage is set to 30 kV, the output power to 20 W and the focal spot size to 20 µm in all measurements.

After the images are taken, the DPC images are retrieved in a ROI around the prism. A sample image can be seen in Figure 5.5. It shows a portion of the prism in the centre. The two inclined surfaces on both sides of the ridge produce different phase signals, as is expected from the design. The prism is surrounded by the support plate with uniform phase shifts close to zero.

The slanted-edge method is then applied to the area in the image, where the prism is located. The inclined surface with negative DPC values is used in place of the area with little to no transmission in the standard slanted-edge analysis. The ROI for the determination of the MTF is limited to areas that contain only the prism. Since the support plate has different differential phase signals than the prism, including it in the analysis causes problem at multiple steps during the data processing.

Noise levels are generally high within the images, this is partly due to the interferometer absorbing significant parts of the X-ray radiation before it even reaches the detector. Hence, the ROIs are chosen to include as many rows as possible, increasing the number of pixel values per bin in the binning step of the slanted-edge method.

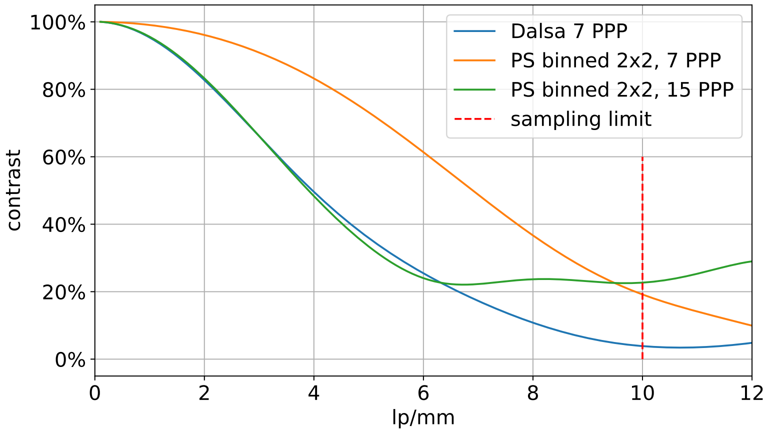

Figure 5.6.: MTF curves measured with different detectors and Moiré patterns. The $MTFs$ plotted with blue and green are measured using the Dalsa Shad-o-Box and the Photonic Science CMOS respectively, but with the same Moiré pattern. The last MTF is acquired using the Photonic Science detector with a Moiré pattern with 7 pixels per period. The increase of contrast in the MTF of the 15 PPP Photonic Science CMOS binned curve for spatial frequencies larger than 6 lp/mm is caused by noise. DPC images from acquired with the Photonic Science CMOS are binned 2 by 2 prior to calculating the MTF.

5.4. Moiré pattern and spatial resolution

The first measurement is performed using the Dalsa Shad-o-Box. The DPC phantom is placed in a distance of 42 ± 1 cm from the source. The interferometer, consisting of the 8078 $G1$ and 1626 $G2$, follows with a distance of 30 ± 1cm. The distance from source to detector is 110 ± 2cm. The interferometer is tuned to a Moiré pattern with a period of 7 pixels, the standard pixels per period (PPP) [Sch20]. The same setup is used to take images with the Photonic Science camera. Since the pixel size for this detector is about half of the Shad-o-Box, the PPP increases to 15, as the interferometer is not altered. Object and reference images are taken before the interferometer is tuned back to 7 PPP by tilting $G2$. Images are also taken with this Moiré pattern.

The resulting $MTFs$ are shown in Figure 5.6. Three curves are plotted, showing the contrast of the ridge for the three different measurements. The noise level of the Photonic Science CMOS measurements is initially too high to perform the slanted-edge analysis, so the DPC images for this detector are binned 2 by 2 prior to the MTF calculation. This decreases the spatial resolution of the images, nonetheless, Figure 5.6 shows interesting results. The measurements taken with the same Moiré pattern, meaning 7 PPP with the Shad-o-Box and 15 PPP with the Photonic Science, have an MTF that is effectively indistinguishable up to about 6 lp/mm. Afterwards, the Photonic science MTF increases once again. The increase is probably a result from noise, since structures like this stem from signal swings in the ESF, as can be seen in Figure 5.3. The Photonic Science measurements using the 7 PPP pattern on the other hand, shows a significantly better

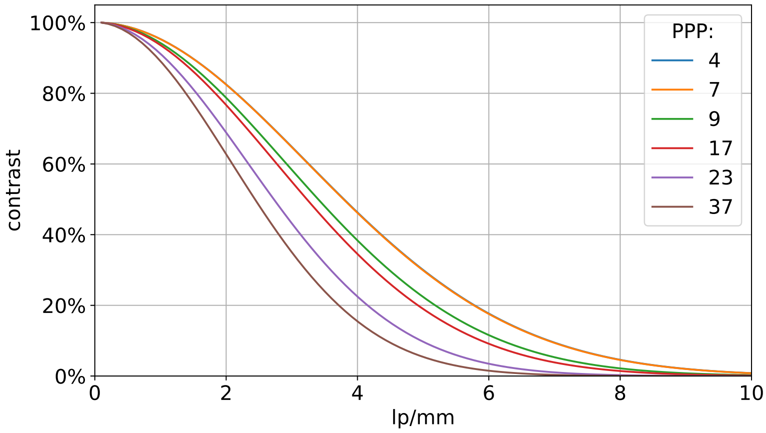

Figure 5.7.: Multiple $MTFs$ measured with the Dalsa Shad-o-Box detector at the ridge of the DPC phantom. Each MTF is measured with a different Moiré pattern period. The 4 PPP MTF is completely covered by the 7 PPP MTF.

contrast over the spatial frequency range, until noise effects in the Photonic Science CMOS curve measured with 15 PPP set in.

The Photonic Science CMOS shows better spatial resolution, even when binned 2 by 2, over a large part of the spatial frequency range (see Figure A.7). This would indicate that for the conditions in the measurements the sharpness of the ridge in the DPC image does not change with increasing detector resolution, but with a decrease in Moiré pattern period. To better test the second aspect, another measurement using only the Dalsa Shad-o-Box is conducted. This time, the third prism is imaged using the same setup as before, but varying the period of the Moiré pattern between each image acquisition. By changing the angle of $G2$, the period of the Moiré pattern is varied between 4 and 37 pixels.

$MTFs$ resulting from this measurement series are shown in Figure 5.7. While the two curves measured for 4 and 7 PPP are practically identical, all higher $MTFs$ measured with higher PPP show reduced sharpness in the edge for increasing Moiré pattern period. The higher the PPP, the faster the decrease in sharpness with increasing lp/mm. These results corroborate the connection between Moiré pattern and spatial resolution in the DPC image.

Two factors probably contribute to the decrease in resolution with increasing Moiré period. First, the DPC information is encoded in small shifts of intensity within the Moiré pattern. The larger the scale of the pattern is, the larger is the area from which a single pixel is influenced. Subsequently, the retrieval process also has to consider the larger area smearing neighbouring pixels. Additionally, the separation of the Fourier peaks is accomplished by applying cuts to the Fourier images. The larger the period of the Moiré pattern, the lower its frequency, moving the first order peak closer to the zeroth order peak. In order to distinguish both, the cuts have to be more strict, removing more of the higher spatial frequency information, thereby worsening spatial resolution.

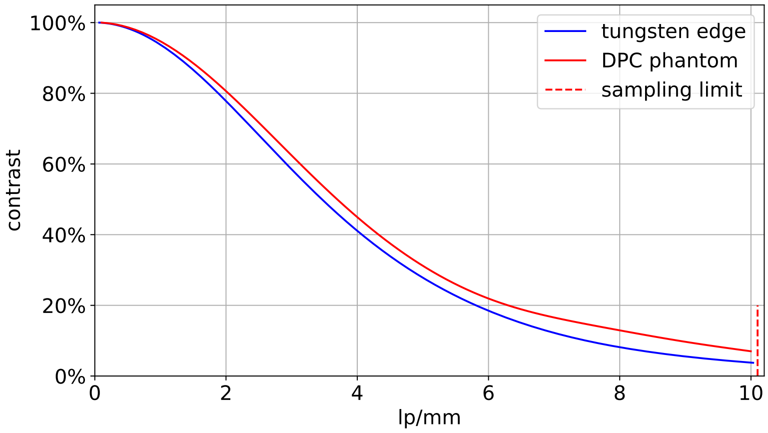

Figure 5.8.: $MTFs$ of the Dalsa Shad-o-Box detector (blue) and the DPC image of the prism (red). The detector MTF is measured with the edge directly in front of the detector, whereas the DPC phantom is placed in distance of $68 \pm 1\,\mathrm{cm}$ from the detector.

In terms of spatial resolution, the Moiré pattern with 7 PPP is optimal for the Dalsa Shad-o-Box. While decreasing the period does not improve the spatial resolution further, increasing the period worsens it significantly. The Shad-o-Box is an indirect detection detectors, where the spatial resolution is determined by the scintillator (see section 4.3) and not the pixel size. In setups using direct detection detectors, the resolution is typically better, even for same pixel sizes. The optimal PPP could be lower in these cases. Similarly, if a detector with wider signal spread is used, the PPP might need to be increased. Additional tests with suitable detectors are required to verify prediction.

5.5. Comparison to raw detector performance and outlook

In subsection 4.3.1 the raw detector resolution of the Dalsa Shad-o-Box was determined using the transmission image of the tungsten edge. These results are now compared with the spatial resolution as measured with the DPC phantom and the same detector. Both $MTFs$ are plotted in Figure 5.8 to allow for an easier comparison.

The MTF measured with the phantom at 7 PP in the DPC image shows consistently higher contrast values for most of the spatial frequency range. Since the DPC target was placed closer to the X-ray tube, smearing from the spot and its movement should decrease the measured contrast. The tungsten edge is placed directly in front of the detector, where the best possible MTF is expected. The MTF measured in the DPC with the phantom being consistently better hence indicates that the spatial resolution within a DPC image is better than in a standard attenuation image.

One possible explanation is the fact, that sources of a phase shift within the DPC image are not resolved directly. Instead, only the shift in the Moiré pattern needs to be resolved. If this shift has a larger spatial extent than the source, the retrieval process is able to retrieve sources that are too small for conventional attenuation imaging with the same detector.

More experiments beyond the scope of this thesis can be performed with the phantom. Using the tungsten edge and attenuation imaging in combination with the interferometer can provide information about the influence of the gratings. Phase stepping, the other grating-based X-ray phase-contrast imaging method mentioned in subsection 2.4.3 uses a similar setup without relying on the Moiré pattern. Instead, the analysis is performed in each Individual pixel. A comparison with phase stepping could therefore provide insights into the influence of the Moiré pattern. Combining the spatial resolution information from the phantom with the visibility of the setup could help in identifying the best Moiré pattern period in more aspects than just spatial resolution. The DPC phantom can therefore be used to gain additional insights into the process of Moiré imaging.

6. Conclusion and outlook

Multiple measurements aimed at improving the quality of images obtained with grating-based X-ray phase-contrast imaging were presented in this thesis.

Angular X-ray transmission (AXT) measurements were implemented following [Gus+19] and [Sch+16]. The method was shown to identify small grating defects as well as large scale deviations in grating parameters like duty cycle, absorber inclination and absorber height. A novel projective correction was developed to compensate for projection errors resulting from the rotation of the grating in front of the detector and thereby increase the sharpness of the obtained parameter maps.

Results of the AXT measurements were then analysed by examining an example measurement with the 1626 grating. Grating defects, cracks within the wafer and deviations in duty cycle were visible within the different parameter maps. These defects and deviations decrease image quality, making knowledge about their locations valuable.

However, a grating support structure caused the analysis to fail in regard to the determination of local absorber height in a large area. A two-dimensional AXT measurement was proposed to properly take into account the two-dimensional nature of the gratings and to overcome this problem.

In an effort to find a detector with the best performance for the backlighter experiment at PHELIX, methods for the characterisation of noise and resolution performance were introduced. The noise characteristics of detectors were compared using series of flat- and dark frames. For resolution characterisation, the slanted-edge method was presented. Compared to the previously used imaging plates, potential for improvement was found with the Photonic Science CMOS camera, especially regarding noise characteristics. The Andor CCD proved to be unsuitable due to its low quantum efficiency at 12 keV, the design energy of the PHELIX imaging setup.

Three other detectors that are meant exclusively for use at our laboratory were examined using the same methods. Of the two flat panel detectors, the Dalsa Shad-o-Box was shown to be superior in terms of spatial resolution compared to the Dalsa Xineos and similar in terms of noise characteristics. Standing out from the two flat panel detectors, the Rigaku X-sight micron LC camera showed impressive spatial resolution with the capability of directly resolving grating structures the size of about 6 µm. Hence, the Rigaku camera can be used to obtain grating parameters inaccessible with AXT measurements. The data presented for these detectors is useful in choosing the best suited detector depending on experimental requirements.

The slanted-edge method used for spatial resolution characterisation was additionally extended to investigate the resolution of DPC images. A dedicated phantom was designed to produce a signal within the differential phase image that is similar to the signal of the tungsten edge in the attenuation image. The influence of the Moiré pattern and the

image modality retrieval on the resulting spatial resolution in the DPC was examined using this phantom.
In this way, a decrease in sharpness of the prism ridge for increasing Moiré pattern period was found. No difference in ridge sharpness was found when the same Moiré pattern, but different detectors were used. This indicates, that the limiting factor of spatial resolution in DPC images is the Moiré pattern and not the detector resolution. Such information is crucial when designing setups where a specific spatial resolution needs to be reached.

The methods introduced in this thesis therefore allow for an in-depth preparation of our imaging setup, further increasing the chance for success during the next beamtimes, and paving the way towards establishing grating-based X-ray phase-contrast imaging as diagnostic tool for high energy density experiments.

Bibliography

[Ant+17] Luca Antonelli et al. 'Laser-driven shock waves studied by x-ray radiography'. In: *Physical Review E* 95 (June 2017). DOI: `10.1103/PhysRevE.95.063205`.

[Col+98] G. W. Collins et al. 'Measurements of the Equation of State of Deuterium at the Fluid Insulator-Metal Transition'. In: *Science* 281.5380 (1998), pp. 1178–1181. DOI: `10.1126/science.281.5380.1178`. eprint: `https://www.science.org/doi/pdf/10.1126/science.281.5380.1178`. URL: `https://www.science.org/doi/abs/10.1126/science.281.5380.1178`.

[Ben+96] Alessandra Benuzzi et al. 'Indirect and direct laser driven shock waves and applications to copper equation of state measurements in the 10–40 Mbar pressure range'. In: *Phys. Rev. E* 54 (2 Aug. 1996), pp. 2162–2165. DOI: `10.1103/PhysRevE.54.2162`. URL: `https://link.aps.org/doi/10.1103/PhysRevE.54.2162`.

[Göt22] Stefan Götte. *PHELIX laser facility.* 7th Apr. 2022. URL: `https://www.gsi.de/en/work/research/appamml/plasma_physicsphelix/phelix`.

[Aks19] Bernhard Akstaller. 'Phase-Contrast Imaging in the Optical Wavelength Regime'. MA thesis. Friedrich-Alexander-Universität Erlangen-Nürnberg, 28th Feb. 2019.

[Bar+19] F. Barbato et al. 'Quantitative phase contrast imaging of a shock-wave with a laser-plasma based X-ray source'. In: *Scientific Reports* 9.1 (Dec. 2019). DOI: `10.1038/s41598-019-55074-1`.

[Dem18] Wolfgang Demtröder. *Experimentalphysik 2.* Springer-Verlag GmbH, 23rd Mar. 2018. ISBN: 3662557894. URL: `https://www.ebook.de/de/product/31029958/wolfgang_demtroeder_experimentalphysik_2.html`.

[POB21] Gavin Poludniowski, Artur Omar and Robert Bujila. 'Technical Note: SpekPy v2.0-a software toolkit for modeling x-ray tube spectra'. In: *Med Phys* (2021). DOI: `10.1002/mp.14945`.

[AB21] Excillum AB. *MetalJet C2.* 25th Nov. 2021. URL: `https://www.excillum.com/our-products/metaljet/metaljet-c2/`.

[ERS02] W T Elam, B Ravel and J Sieber. *A new atomic database for X-ray spectroscopic calculations.* United Kingdom, Feb. 2002. DOI: `10.1016/S0969-806X(01)00227-4`.

[Dem17] Wolfgang Demtröder. *Experimentalphysik 4. Kern-, Teilchen- und Atomphysik.* Springer-Verlag GmbH, 28th Feb. 2017. ISBN: 978-3-662-52883-9. URL: `https://www.ebook.de/de/product/26707431/wolfgang_demtroeder_experimentalphysik_4.html`.

[CAS17] David (University of California, Berkeley) Attwood and Anne Sakdinawat. *X-Rays and Extreme Ultraviolet Radiation.* Cambridge University Press, 16th Feb. 2017. 652 pp. ISBN: 1107062896. URL: `https://www.ebook.de/de/product/26311551/david_university_of_california_berkeley_attwood_anne_sakdinawat_x_rays_and_extreme_ultraviolet_radiation.html`.

[HS96] J.H. Hubbel and S.M Seltzer. *X-Ray Mass Attenuation Coefficients.* Radiation Physics Division, PML, NIST. 1996. URL: `https://physics.nist.gov/PhysRefData/XrayMassCoef/chap2.html` (visited on 10/12/2021).

[Miy+86] Junji Miyahara et al. 'A new type of X-ray area detector utilizing laser stimulated luminescence'. In: *Nuclear Instruments and Methods in Physics Research Section A: Accelerators, Spectrometers, Detectors and Associated Equipment* 246.1 (1986), pp. 572–578. ISSN: 0168-9002. DOI: `https://doi.org/10.1016/0168-9002(86)90156-7`. URL: `https://www.sciencedirect.com/science/article/pii/0168900286901567`.

[Fik+12] G Fiksel et al. 'Note: Spatial resolution of Fuji BAS-TR and BAS-SR imaging plates'. In: *Review of Scientific Instruments* 83.8 (2012), p. 086103.

[Lut+07] Gerhard Lutz et al. *Semiconductor radiation detectors.* Springer, 2007. ISBN: 978-3-540-71678-5.

[BP18] Karl W. Boer and Udo W. Pohl. *Semiconductor physics.* Springer Berlin Heidelberg, 2018.

[GTE02] Sol M. Gruner, Mark W. Tate and Eric F. Eikenberry. 'Charge-coupled device area x-ray detectors'. In: *Review of Scientific Instruments* 73.8 (2002), pp. 2815–2842. DOI: `10.1063/1.1488674`. eprint: `https://doi.org/10.1063/1.1488674`. URL: `https://doi.org/10.1063/1.1488674`.

[GC16] Luiz Carlos Paiva Gouveia and Bhaskar Choubey. 'Advances on CMOS image sensors'. In: *Sensor review* (2016).

[Mag03] Pierre Magnan. 'Detection of visible photons in CCD and CMOS: A comparative view'. In: *Nuclear Instruments and Methods in Physics Research Section A: Accelerators, Spectrometers, Detectors and Associated Equipment* 504.1 (2003). Proceedings of the 3rd International Conference on New Developments in Photodetection, pp. 199–212. ISSN: 0168-9002. DOI: `https://doi.org/10.1016/S0168-9002(03)00792-7`. URL: `https://www.sciencedirect.com/science/article/pii/S0168900203007927`.

[KW16] Hermann Kolanoski and Norbert Wermes. *Teilchendetektoren.* Springer, 2016. ISBN: 978-3-662-45349-0. DOI: `https://doi.org/10.1007/978-3-662-45350-6`.

[Pag06] David Paganin. *Coherent x-ray optics*. Oxford New York: Oxford University Press, 2006. ISBN: 9780198567288.

[Bor99] Max Born. *Principles of optics : electromagnetic theory of propagation, interference and diffraction of light*. Cambridge New York: Cambridge University Press, 1999. ISBN: 0521642221.

[Tal36] H.F. Talbot. 'LXXVI. Facts relating to optical science. No. IV'. In: *The London, Edinburgh, and Dublin Philosophical Magazine and Journal of Science* 9.56 (1836), pp. 401–407. DOI: `10.1080/14786443608649032`. eprint: `https://doi.org/10.1080/14786443608649032`. URL: `https://doi.org/10.1080/14786443608649032`.

[Eng+07] Martin Engelhardt et al. 'High-resolution differential phase contrast imaging using a magnifying projection geometry with a microfocus x-ray source'. In: *Applied Physics Letters* 90.22 (2007), p. 224101. DOI: `10.1063/1.2743928`. eprint: `https://doi.org/10.1063/1.2743928`. URL: `https://doi.org/10.1063/1.2743928`.

[Lud20] Veronika Ludwig. 'Development of image acquisition and alignment methods for X-ray dark-fieldand phase-contrast imaging'. PhD thesis. Friedrich-Alexander-Universität Erlangen-Nürnberg, 10th May 2020.

[Sch16] Max Schuster. 'Design und Charakterisierung eines Talbot-Interferometers mit Mikrofokus-Röntgenröhre'. Masters Thesis. Friedrich-Alexander-Universität Erlangen-Nürnberg, 16th May 2016.

[Sei20] Maria Seifert. 'X-ray phase-contrast and dark-fieldimaging in single-shot and scanningmode'. PhD thesis. Friedrich-Alexander-Universität Erlangen-Nürnberg, 12th Oct. 2020.

[Ami09] Isaac Amidror. *The Theory of the Moiré Phenomenon*. Springer-Verlag GmbH, 15th Mar. 2009. ISBN: 9781848821811.

[TIK82] Mitsuo Takeda, Hideki Ina and Seiji Kobayashi. 'Fourier-transform method of fringe-pattern analysis for computer-based topography and interferometry'. In: *Journal of the Optical Society of America* 72.1 (Jan. 1982), pp. 156–160. DOI: `10.1364/JOSA.72.000156`. URL: `http://www.osapublishing.org/abstract.cfm?URI=josa-72-1-156`.

[Ben+10] E Bennett et al. 'A grating-based single-shot x-ray phase contrast and diffraction method for in vivo imaging'. In: *Medical Physics* 37.11 (2010), pp. 6047–6054. DOI: `10.1118/1.3501311.-DOI10.1118/1.3501311`.

[Bev+12] N Bevins et al. 'Multicontrast x-ray computed tomography imaging using Talbot-Lau interferometry withoutphase stepping'. In: *Medical Physics* 39.1 (2012), pp. 424–428. DOI: `10.1118/1.3672163.-DOI10.1118/1.3672163`.

[Die19] Lisa Dietrich. 'Entwicklung und Charakterisierung von Testobjekten für die Phasenkontraströntgenbildgebung'. Bachelor Thesis. Friedrich- Alexander-Universität Erlangen-Nürnberg, 2nd Aug. 2019.

[Sei+18] Maria Seifert et al. 'Improved Reconstruction Technique for Moiré Imaging Using an X-Ray Phase-Contrast Talbot–Lau Interferometer'. In: *Journal of Imaging* 4.5 (2018), p. 62.

[Hof18] Fabian Hofmann. 'Modeling and Correcting Moiré Artifacts in Grating-Based Phase-Contrast X-Ray Imaging'. Masters Thesis. Friedrich-Alexander-Universität Erlangen-Nürnberg, 1st Aug. 2018.

[Sch20] Stephan Schreiner. 'Design and characterization of a portable Talbot interferometer for imaging high energy density experiments'. MA thesis. Erlangen Centre for Astroparticle Physics Department of Physics Friedrich-Alexander-Universität Erlangen-Nürnberg, 3rd Nov. 2020.

[Gus+19] Nikolai Gustschin et al. 'Quality and parameter control of X-ray absorption gratings by angular X-ray transmission'. In: *Optics express* 27.11 (2019), pp. 15943–15955.

[Sch+16] Markus Schüttler et al. 'Height control for small periodic structures using x-ray radiography'. In: *Measurement Science and Technology* 27.2 (2016), p. 025015.

[Pas] SEM images provided by Pascal Meyer. *(Karlsruhe Institute of Technology, Institute of Microstructure Technology).*

[Ros69] Kurt Rossmann. 'Point Spread-Function, Line Spread-Function, and Modulation Transfer Function'. In: *Radiology* 93.2 (1969). PMID: 5822701, pp. 257–272. DOI: `10.1148/93.2.257`. eprint: `https://doi.org/10.1148/93.2.257`. URL: `https://doi.org/10.1148/93.2.257`.

[RPN91] Stephen E. Reichenbach, Stephen K. Park and Ramkumar Narayanswamy. 'Characterizing digital image acquisition devices'. In: *Optical Engineering* 30.2 (1991), pp. 170–177. DOI: `10.1117/12.55783`. URL: `https://doi.org/10.1117/12.55783`.

[EM04] Magali Estribeau and Pierre Magnan. 'Fast MTF measurement of CMOS imagers using ISO 12333 slanted-edge methodology'. In: 5251 (2004). Ed. by Jean-Pierre Chatard and Peter N. J. Dennis, pp. 243–252. DOI: `10.1117/12.513320`. URL: `https://doi.org/10.1117/12.513320`.

[Sta21] International Organization for Standardization. *ISO 12233:2017 Photography — Electronic still picture imaging — Resolution and spatial frequency responses.* 8th May 2021. URL: `https://www.iso.org/standard/71696.html`.

[Bur00] Peter D. Burns. 'Slanted-Edge MTF for Digital Camera and Scanner Analysis'. In: (2000).

[Har78] Fredric J. Harris. 'On the Use of Windows for Harmonic Analysis with the Discrete Fourier Transform'. In: *Proceedings of the IEEE* 66.1 (Jan. 1978), pp. 51–83. DOI: `10.1109/PROC.1978.10837`.

[FC08] S. N. Friedman and I. A. Cunningham. 'Normalization of the modulation transfer function: The open-field approach'. In: *Medical Physics* 35.10 (2008), pp. 4443–4449. DOI: `https://doi.org/10.1118/1.2977536`. eprint: `https://aapm.onlinelibrary.wiley.com/doi/pdf/10.1118/1.2977536`. URL: `https://aapm.onlinelibrary.wiley.com/doi/abs/10.1118/1.2977536`.

[Sha49] Claude Elwood Shannon. 'Communication in the presence of noise'. In: *Proceedings of the IRE* 37.1 (1949), pp. 10–21.

[Mul21] Alan Mullan. *Calculating the Signal to Noise Ratio of a Camera*. 26th Aug. 2021. URL: `https://andor.oxinst.com/learning/view/article/ccd-signal-to-noise-ratio`.

[Mul+94] James C. Mullikin et al. 'Methods for CCD camera characterization'. In: *Image Acquisition and Scientific Imaging Systems*. Ed. by Helen C. Titus and Amir Waks. Vol. 2173. International Society for Optics and Photonics. SPIE, 1994, pp. 73–84. DOI: `10.1117/12.175165`. URL: `https://doi.org/10.1117/12.175165`.

[Iri+08] Kenji Irie et al. 'A Technique for Evaluation of CCD Video-Camera Noise'. In: *IEEE Transactions on Circuits and Systems for Video Technology* 18.2 (2008), pp. 280–284. DOI: `10.1109/TCSVT.2007.913972`.

[JT 11] J.M Boone J.T. Bushberg. *The Essential Physics of Medical Imaging*. Online access: Ovid Technologies LWW Doody's Core Collection 2019. Wolters Kluwer Health, 2011. ISBN: 9780781780575. URL: `https://books.google.de/books?id=tqM8IG3f8bsC`.

[KW14] Mikhail Konnik and James Welsh. *High-level numerical simulations of noise in CCD and CMOS photosensors: review and tutorial*. 2014. DOI: `10.48550/ARXIV.1412.4031`. URL: `https://arxiv.org/abs/1412.4031`.

[Met20] W. J. Metzger. *Statistical Methods in Data Analysis*. 17th Oct. 2020. URL: `https://www.hef.ru.nl/~wes/stat_course/statist.pdf`.

[Ima20] Teledyne Rad-icon Imaging. *Shad-o-Box HS Product Family Datasheet*. Ed. by Inc. A BU of Teledyne Digital Imaging US. Accessed Oct. 25, 2020. 25th Oct. 2020. URL: `https://www.teledynedalsa.com/en/products/imaging/industrial-x-ray/shad-o-box-hs/`.

[Dal] Teledyne Dalsa. *Xineos-1511 CMOS Flat X-ray Detectors for cost-effective Dental 3D+Panoramic*. URL: `https://www.teledynedalsa.com/en/products/imaging/medical-x-ray-detectors/xineos-large-area/xineos-1511-gige/` (visited on 02/03/2022).

[Cor22] Rigaku Corporation. *XSight Micron LC*. 12th Feb. 2022. URL: `https://www.rigaku.com/de/products/detectors/micron-lc?index=0`.

[Scia] Photonic Science. *X-raysCMOS 4MPDetector*. URL: `https://photonicscience.com/products/x-ray-cameras/x-ray-scmos-4mp-detector/` (visited on 02/03/2022).

[Scib] Photonic Science. *PSViewer Software User guide.*

[Tec] Andor Technology. *iKon-M SO High Energy Imaging Open Front Direct Detection.* URL: `https://andor.oxinst.com/products/high-energy-detection/ikon-m-so` (visited on 02/03/2022).

[Sei+20] M Seifert et al. 'Evaluation of the Weighted Mean X-ray Energy for an Imaging System Via Propagation-Based Phase-Contrast Imaging'. In: *Journal of Imaging* (1st July 2020). DOI: `10.3390/jimaging6070063`.

[Sch22] Bernd Schmitt. *JUNGFRAU: adJUstiNg Gain detector FoR the Aramis User station.* 21st Apr. 2022. URL: `https://www.psi.ch/en/lxn/jungfrau`.

[Red+18] S. Redford et al. 'First full dynamic range calibration of the JUNGFRAU photon detector'. In: *Journal of Instrumentation* 13.01 (Jan. 2018), pp. C01027–C01027. DOI: `10.1088/1748-0221/13/01/c01027`. URL: `https://doi.org/10.1088/1748-0221/13/01/c01027`.

[Jun+14] J H Jungmann-Smith et al. 'JUNGFRAU 0.2: prototype characterization of a gain-switching, high dynamic range imaging system for photon science at SwissFEL and synchrotrons'. In: *Journal of Instrumentation* 9.12 (Dec. 2014), P12013–P12013. DOI: `10.1088/1748-0221/9/12/p12013`. URL: `https://doi.org/10.1088/1748-0221/9/12/p12013`.

A. Appendix

A.1. Grating parameters

name	type	period	duty cycle	structure height	waver material	waver thickness
1626	$G2$	6 µm	0.72	150 µm	graphite	500 µm
8077	$G2$	6 µm	0.72	150 µm	Vespel	500 µm
8078	$G1$	10 µm	$0,5$	25 µm	Polyimide	500 µm

Table A.1.: Grating parameters of the gratings used in this thesis.

A.2. Verification of the slanted-edge method

The slanted-edge method is verified using a line grating target constructed from a thin lead film coated in plastics. It contains thirteen areas with line gratings of different frequencies from 0.005 lp/mm to 10 lp/mm. A transmission image of this target is shown in Figure A.1a, the spatial frequencies of the grating regions increase from the top of the target to the bottom. By calculating the contrast within the grating areas, the MTF is sampled at the corresponding spatial frequencies. The results can then be compared to the slanted-edge results.

The construction of the line grating target causes a problem, that has to be addressed first. At lower photon energies, the plastics absorb significant amounts of radiation, whereas at higher photon energies, not all radiation is absorbed within the lead structures. This means, that the target does not possess an object contrast of one. After the standard gain and offset corrections are applied, additional corrections are required to compensate. First, an area with only lead is taken and its transmission values averaged. This value is then subtracted from the entire image. Second, an area with only plastics is chosen, the relative transmission in this area is calculated, and each pixel is divided by the obtained value. This ensures, that areas with lead have values of zero, whereas areas with plastics have values of one, creating an object contrast close to one.

In the next step, lines through the different grating areas are investigated. One such line is shown in Figure A.1b. As can be seen, at lower pixel indices, where the spatial frequencies are lower, the maxima lie close to one and the minima close to zero. With increasing spatial frequencies, the maxima diminish, while the minima increase, until they are barely distinguishable. This is the decrease in contrast, that is to be determined. For each trace, the different line grating areas are identified and the maximum and minimum values are found. This is done for many lines to reduce the influence of noise.

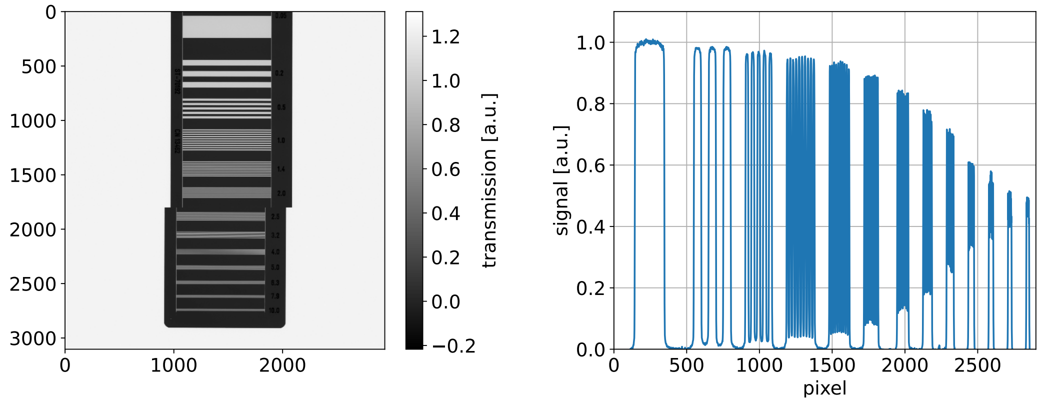

(a) Transmission image of the line resolution target used for spatial resolution characterisation. The image is a composite of two exposures, since the target is too large to fully fit within the FOV.

(b) Individual line taken from the transmission image of the line grating target, with all gain and offset corrections applied. The transmission signal is plotted in arbitrary units over the horizontal pixel index.

Figure A.1.

An averaged maximum I_{max} and minimum I_{min} is calculated in each grating region. From these values the contrast

$$C(f) = \frac{I_{\text{max}}(f) - I_{\text{min}}(f)}{I_{\text{max}}(f) + I_{\text{min}}(f)} \tag{A.1}$$

is calculated. The high number of data points in each grating area can also be used to estimate the uncertainty on these results. By estimating the uncertainty for each maximum and minimum via

$$\Delta I_{\text{max/min}}(f) = \frac{\sigma(I_{\text{max/min}})}{\sqrt{N-1}}, \tag{A.2}$$

where σ is the standard deviation and N the number of maxima or minima, and usage of Gaussian uncertainty propagation, a formula for the uncertainty of the contrast can be obtained:

$$\Delta C(f) = \sqrt{\left(\frac{2I_{\text{max}}(f)}{K}\Delta I_{\text{min}}(f)\right)^2 + \left(\frac{2I_{\text{min}}(f)}{K}\Delta I_{\text{max}}(f)\right)^2} \tag{A.3}$$

$$K = (I_{\text{max}}(f) + I_{\text{min}}(f))^2 \tag{A.4}$$

Both the contrast and the uncertainty for the Dalsa Shad-o-Box over the frequencies are shown in Figure A.2 as data points with error bars. It agrees well with the values obtained with the slanted-edge resolution method, that is also shown in Figure A.2.
An advantage of the line resolution target method is, that it does not require knowledge of the pixel pitch, which is often only known from the manufacturer. The method has

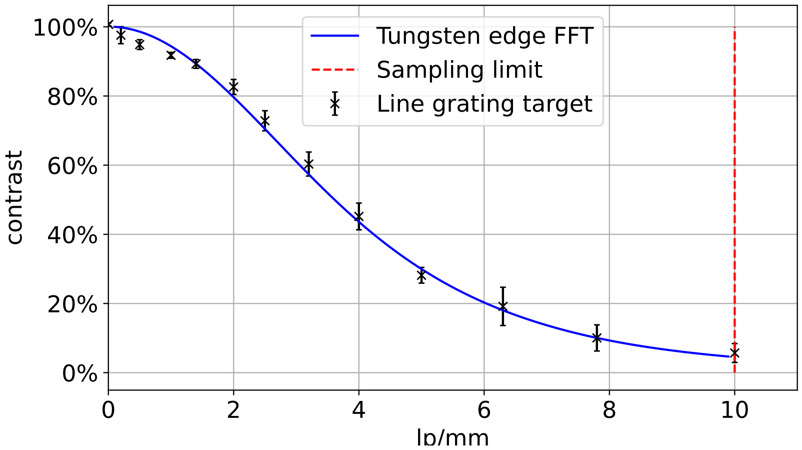

Figure A.2.: Verification of the slanted-edge method. Shown are the MTF (blue) as calculated using the slanted edge method for the Dalsa Shad-o-Box and contrast values obtained with the line grating target (black markers). Also shown is the sampling limit due to the Nyquist-Shannon theorem (red).

a few disadvantages. The target must be aligned well with the pixel edges, otherwise the measured contrast changes. The sampling rate of the MTF depends on the grating targets available, increasing the number of grating targets reduces the speed of the method, as more images need to be taken. Hence, the method is not used for detector characterisation. Instead, only a verification of the slanted-edge method is done.

A.3. 70 kV noise characteristics

In the following plots similar to the flat field noise characteristic plots in chapter 4 are presented. They are taken with the same settings as the corresponding 30 kV plots, except that the acceleration voltage is set to 70 kV.

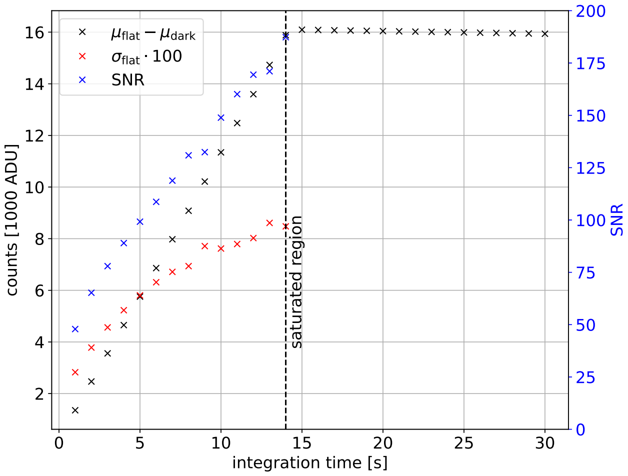

Figure A.3.: Flat frame noise characteristics of the Dalsa Shad-o-Box detector. The plot shows the counts in ADU over the integration time in seconds. Black data points are the mean signal, red data points the noise. The solid black line represents a linear fit. The blue data points use the right y-axis and show the SNR over integration time.

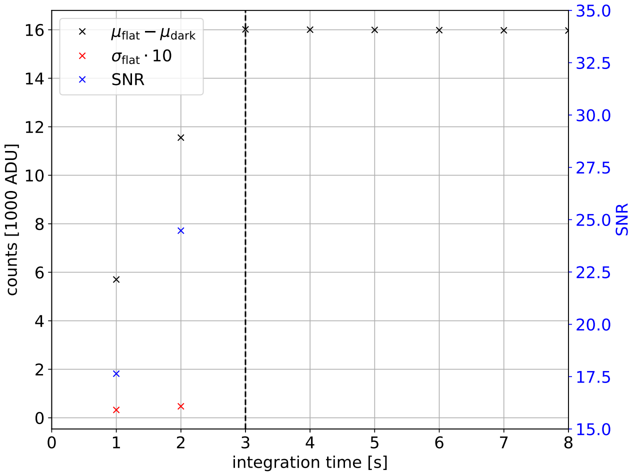

Figure A.4.: Flat frame noise characteristics of the Dalsa Xineos detector. The plot shows the counts in ADU over the integration time in seconds. Black data points are the mean signal, red data points the noise. The solid black line represents a linear fit. The blue data points use the right y-axis and show the SNR over integration time.

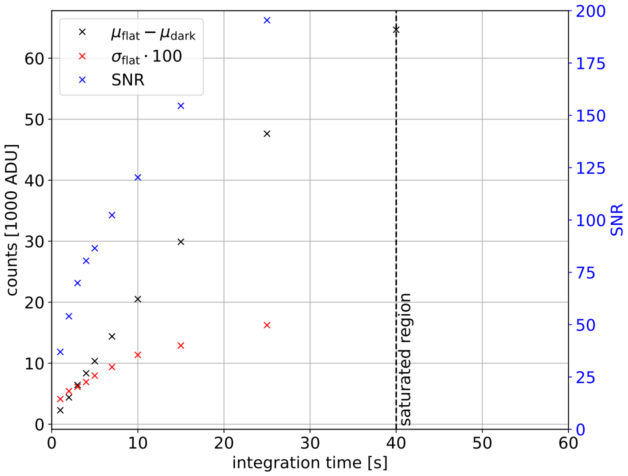

Figure A.5.: Flat frame noise characteristics of the Photonic Science CMOS detector. The plot shows the counts in ADU over the integration time in seconds. Black data points are the mean signal, red data points the noise. The solid black line represents a linear fit. The blue data points use the right y-axis and show the SNR over integration time.

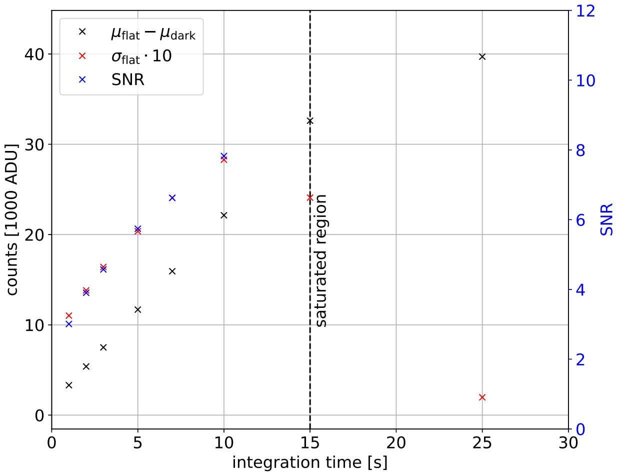

Figure A.6.: Flat frame noise characteristics of the Andor iKon CCD detector. The plot shows the counts in ADU over the integration time in seconds. Black data points are the mean signal, red data points the noise. The solid black line represents a linear fit. The blue data points use the right y-axis and show the SNR over integration time.

A.4. DPC Phantom

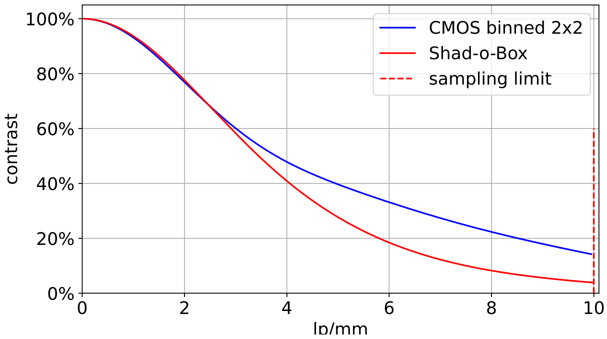

Figure A.7.: Resolution comparison between the Dalsa Shad-o-Box (red) and the Photonic Science CMOS detector (blue). Shown are the *MTFs* of both detectors, encoding the retained resolution over spatial frequency in lp/mm.

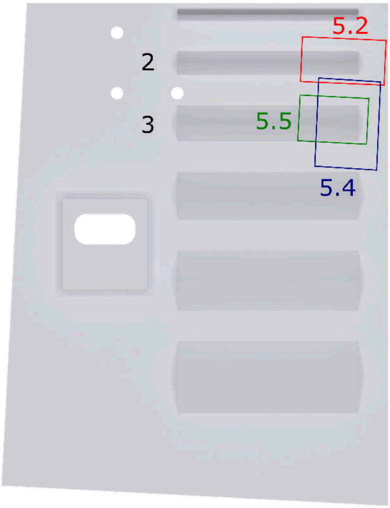

Figure A.8.: ROIs of Figures 5.2 (red), 5.4 (blue) and 5.5 (green) shown in front of the DPC phantom. Figure 5.4 is mirrored.

Acknowledgments

At the end of my thesis, I want to thank all who have helped me in getting here. In no particular order, I thank

- Prof. Dr. Gisela Anton, Prof. Dr. Stefan Funk and PD Dr. Thilo Michel for their supervision.
- Stephan Schreiner and Bernhard Akstaller for introducing me to the topic and their support over the last year.
- The entire PHACT group for their input during meetings and the friendly atmosphere.
- Pascal Meyer, who provided the gratings and help with the AXT measurements.
- Paul Neumayer for providing the Andor CCD and Photonic Science CMOS camera.
- The mechanical workshop for producing the DPC target.
- Stephan Schreiner, Bernhard Akstaller and Dorothea Rauch for proofreading this thesis.
- My family for their unyielding support and encouragement during my five and half years of studies.

Erklärung

Hiermit erkläre ich, die vorliegende Arbeit eigenständig und nur unter Verwendung der angegebenen Hilfsmittel erstellt zu haben. Diese Masterarbeit wurde weder in gleicher noch in ähnlicher Form einer anderen Prüfungsbehörde vorgelegt.

Ort, Datum	Unterschrift